Author/s:
Jung, Young Jun

Title:
Functional organisation of the tammar wallaby visual cortex

Date:
2020

Persistent Link:
https://hdl.handle.net/11343/268025

FUNCTIONAL ORGANISATION OF THE TAMMAR WALLABY VISUAL CORTEX

Young Jun Jung

ORCID id: 0000-0002-3762-0735

Doctor of Philosophy

November 2020

Department of Optometry and Vision Sciences
The University of Melbourne
and
National Vision Research Institute
Australian College of Optometry

Submitted in total fulfilment of the degree of
Doctor of Philosophy

Abstract

How are the complex maps for feature selectivity created in the mammalian visual cortex? In most Eutherian mammals (e.g. cats, ferrets, tree shrews, and primates), orientation selective cells are organised into columns, which are arranged in pinwheel-like patterns across the cortex. However, rodents and rabbits do not have the same cortical structure: although they have robust orientation selectivity (OS) in individual cells, these are randomly distributed across the cortex in salt-and-pepper maps. Many studies have tried to explain how the complex maps for orientation preference (OP) are created in the primary visual cortex (V1). However, it remains unknown why some mammals have random salt-and-pepper OP maps while others have pinwheel OP maps.

In the first chapter, we used intrinsic optical imaging to determine the cortical map structures in the V1 of a marsupial, the tammar wallaby *(Macropus Eugenii)*. Marsupials represent a phylogenetically distinct branch of early mammals and we are the first to examine cortical map structures in a mammal that is not a member of the following mammalian Clades: Glires (e.g. rats, mice, squirrels), Laurasitheria (e.g. cats, ferrets) or Euarchonta (e.g. primates).We found clear orientation columns, arranged in pinwheel-like patterns across the cortex. Based on the finding of pinwheel maps in a marsupial and their similarity to those found in cats and primates, we proposed that the columnar organisation of OPs may be a primitive feature of the mammalian visual cortex and that the species in the Clade Glires (i.e. rodents and rabbits) are the unusual case in terms of mammalian visual brain organisation. We also proposed that the type of cortical map can be predicted by the central-to-peripheral ratio (CP ratio) of retinal ganglion cell (RGC) densities.

Second, we extracellularly recorded and estimated the spatial RFs of neurons from the wallaby V1 and LGN in response to white-Gaussian noise (WGN) using 32-channel array probes. Single units were characterised using the nonlinear input model (NIM). We found that OS in the V1 of marsupial wallabies emerges from less selective LGN cell inputs, similar to cats and primates. Again, rodents and rabbits were found to be the odd ones out, suggesting that they have a unique neural circuitry different to other mammals. The NIM framework provided a far

more comprehensive analysis of RF properties of neurons in the marsupial cortex, with greater variation in RF structures of simple and complex cells than reported based on simplistic F1/F0 analysis.

In the final chapter, we extracted the extracellular spikes of V1 neurons and examined their spatial RFs using the NIM. Consistent with findings from cat V1, we found five distinct classes of extracellular spike waveforms in wallaby V1: regular spiking, fast spiking, triphasic spiking, compound spiking, and positive spiking. The five different spike waveforms were correlated to their spatial RF types and spiking characteristics. We found that negative spiking units showed characteristics typical of cortical cells, and the positive spiking units have similar RF types and spiking characteristics to the thalamic afferents that originate outside the cortex. Moreover, the RF properties of cortical neurons with positive spiking units resembled the wallaby LGN neurons we recorded in the study.

Declaration

I hereby declare that:

- this thesis comprises of my original work towards the degree of Doctor of Philosophy except where indicated in the preface,
- acknowledgement has been made in the text to all other material used,

  and
- this thesis is below the maximum allowable word limit in length, exclusive of tables and bibliographies.

Young Jun Jung

November 2020

Preface

I performed all experimental work from wallaby cortex in Professor Michael Ibbotson's laboratory at the National Vision Research Institute (NVRI). I conducted and was responsible for the collection of optical imaging and electrophysiological data and the analysis of all my data. In detail, the contributions were:

- designing experimental protocols including the stimuli and analysis,
- conducting the experiments including the surgery, in which I was trained during my studies. These experiments were conducted with the assistance of my colleagues at the NVRI as each experiment continued for 72 hours of non-stop recordings,
- analysis of the data featured in this thesis.
- assisting with the care and maintenance of the research animals at the NVRI.

Introductory Chapter has been published.

[Ibbotson, M., & Jung, Y. J. (2020). Origins of Functional Organization in the Visual Cortex. Frontiers in Systems Neuroscience, 14, 10.]

The publications based on the results chapters of this thesis are currently under preparation.

Acknowledgements

Throughout the writing of this dissertation I have received a great deal of support and assistance from many people. First and foremost, I am extremely grateful to my supervisors, Prof. Michael Ibbotson and Dr. Hamish Meffin for their invaluable advice, continuous support, and patience during my PhD study. Their immense knowledge and abundant experience have encouraged me in all the time of my academic research and have allowed me to grow as a young scientist.

I would also like to extend my sincere thanks to Prof. Marilyn Renfree who has kindly provided us with the wallabies to make this project possible. I would also like to thank Dr. Shaun Cloherty and Dr. Sebastien Baquier for their technical support on the experimental side of my research. My gratitude also goes to my PhD advisory committee, Prof. Andrew Anderson and Prof. Andrew Metha for their valuable advice during my committee meetings.

To my fellow colleagues at the NVRI, they have all made my PhD journey enjoyable and less daunting. A special thanks goes to Dr. Ali Almasi, Dr. Shi Hi Sun, and Dr. Molis Yunzab for their continuous assistance and support throughout my journey.

Finally, I would like to show my deepest gratitude to my family for their love, encouragement, moral support, and blessings. I appreciate all of the sacrifices that my parents have made for me. Without their support, I would have not come this far. A special thanks to my wife, Betty who has been through this journey the whole time. Betty was stuck with me 24/7 during the last 6 months of my candidature, as we were both under COVID-19 lockdown. Without her continuous encouragement and incredible editing work, it would have not been possible for me to complete my study.

”And God said, Let the land produce living creatures according to their kind…
And God saw that it was good.”

Genesis

Contents

List of Figures

CHAPTER 1

CHAPTER 2

CHAPTER 3

Chapter 1

Background

An area of great interest in the field of visual neuroscience is how the complex maps of visual information are created in the primary visual cortex (V1). The maps cluster together cells that code specific stimulus attributes, such as location in the visual field (retinotopy), eye of origin, orientation preference, direction preference, spatial frequency and colour (Bonhoeffer & Grinvald, 1991; Horton & Hubel, 1981; Hubel & Wiesel, 1968; LeVay & Gilbert, 1976; Weliky et al., 1996; Hubel & Wiesel, 1969). The organisation of visual cortical maps became a major topic of interest recently when it was discovered that rodents and rabbits do not have the same map structure as cats and monkeys (as reviewed by Ibbotson & Jung, 2020). Given other clear similarities in the organisation of the visual pathways, why is it that maps coding the same sensory information are so radically different? In this chapter, I will begin with a brief description of how the visual world is processed by the mammalian visual system, with a strong emphasis on the primary visual cortex. Then, I will outline the basic anatomical, physiological, and functional features of the mammalian primary visual cortex and review the current literature surrounding the origins of the functional maps.

The experimental animal used in this thesis is the marsupial tammar wallaby *(Macropus eugenii)*. There are a number of reasons why the tammar wallaby was selected for investigation and this will be discussed in the literature review. The descriptions of the neural processing will mainly refer to the wallaby visual system, which will be compared to that of cats and monkeys.

1.1 Early visual processing

Figure 1.1 illustrates the early visual pathway. Light enters the eye and hits the photoreceptors at the outermost part of the retina, which transduce light into electrochemical signals. There are two types of photoreceptors: rods and cones. Rods are highly sensitive to light and are responsible for providing scotopic vision (i.e. vision in dim light). Cones are less sensitive to light and are responsible for delivering photopic vision (i.e. in bright light) and colour vision (Kolb & Famigilietti, 1974; Kolb et al., 1981). Photoreceptors form synapses in the outer plexiform layer with horizontal cells and bipolar cells. Bipolar cells synapse either directly or indirectly via AII amacrine cells to the retinal ganglion cells (RGCs) in the inner plexiform layer. RGCs are the only cells in the retina that can conduct action potentials. The action potential is achieved once the cell membrane reaches a threshold electrical potential. The axons of RGCs converge to form the optic nerve, which transmits visual signals from the retina to the dorsal lateral geniculate nucleus (LGN) in the thalamus.

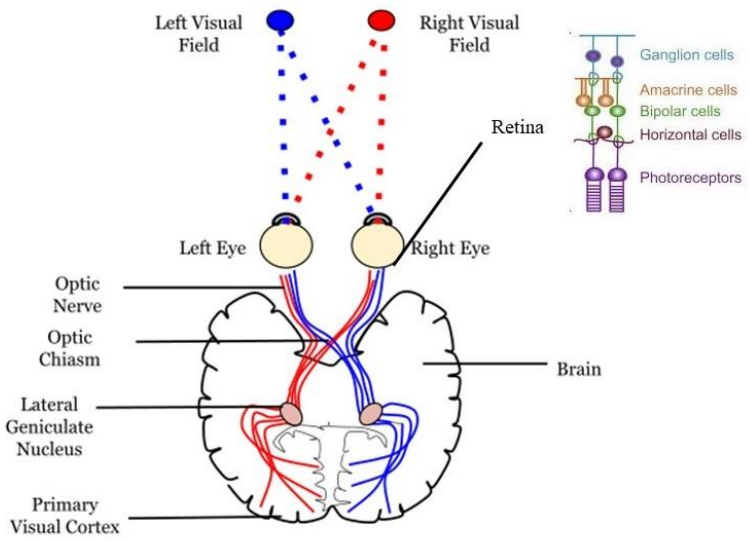

Figure 1.1 The visual pathway from the retina to the primary visual cortex. Light enters the retina and retinal ganglion cells (RGCs) send electrical signals to the lateral geniculate nucleus (LGN), which relays information to the primary visual cortex (V1). Top right inset illustrates visual processing occurring at the retinal level. Source: visual pathway image from open source under Creative Commons license; retinal image from Alonso (2002).

Kuffler (1953) first used the term receptive fields (RFs) to describe a discrete region in visual space where the action of light modulates the rate of cell firing. The spatial RFs of neurons in the retina (RGCs) and LGN are organised into two regions, centre and surround (Figure 1.2) (Hubel & Wiesel, 1962). For an ON-centre cell (left), a light stimulus in the central subregion increases the cell's response, while it inhibits the cell's response in the surround subregion. An OFF-centre cell (right) has the opposite configuration (i.e. excited by dark stimuli in the centre). This specific RF organisation detects local luminance contrast in the visual environment.

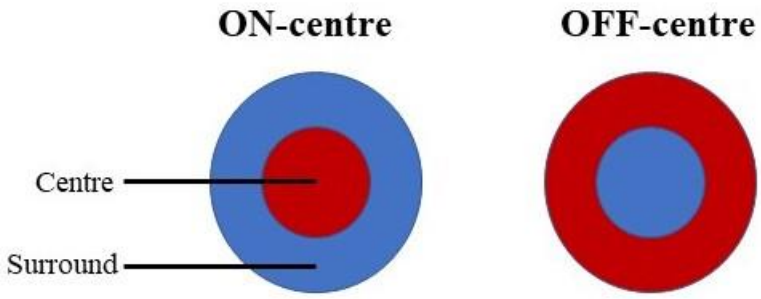

Figure 1.2 The spatial RFs of neurons in the retina (RGCs) and LGN. They have circular antagonistic centre-surround organisation. Left: ON-centre RF. Right: OFF-centre RF.

1.2 Primary visual cortex (V1)

Situated at the posterior pole of the cerebral cortex (occipital lobe), the visual cortex is responsible for processing visual information that is received from the retina via the lateral geniculate nucleus (LGN). The region that receives direct inputs from the LGN neurons is called the primary visual cortex (also known as Area 17 or V1). V1 is also referred to as the striate cortex due to its distinctly laminated appearance in cross sections. In the following, I will discuss the anatomical, physiological, and functional organisation of the primary visual cortex in more detail.

1.2.1 Anatomical organisation of V1

There are six functionally distinct layers in the mammalian primary visual cortex (

Figure **1.3**A; example from wallaby V1). The distinct layers emerge from the presence of myelinated axons and the disposition of different neuronal bodies (Gabbott & Somogyi, 1986). In the primary visual cortex, there are three classes of neurons: two excitatory and one inhibitory. The two excitatory neurons are spiny pyramidal and stellate cells. Both cells have branches of apical dendrites with spines (Peters & Sethares, 1991). Pyramidal cells make up the majority of cortical neurons (80%) and form intrinsic local connections in layers 2/3, as well as long-range connections to different areas (Peters & Sethares, 1991) (Figure 1.3B). The lateral axon projections of pyramidal cells form clusters of connections in a set of patches, which allow integration of visual information from different receptive fields (Hubel & Wiesel, 1974). Spiny stellate cells in layer 4 have spherical dendritic trees that form the major excitatory pathway to pyramidal cells in layers 2/3 (Feldmeyer et al., 1999; 2002).

Inhibitory neurons in the primary visual cortex are called aspiny interneurons. They have a rounder cell body compared to excitatory neurons, with almost no spines on their dendrites (Figure 1.3B). There are three main types of smooth spinous interneurons: basket cells, chandelier cells, and double bouquet cells. Basket cells have a relatively large cell body that projects myelinated axonal

branches across a considerable distance to the pyramidal cell body. Chandelier cells are characterised by their synaptic connections to axon initial segments. Double bouquet cells have axonal collaterals and bitufted dendrites that are tightly intertwined in bundles across layers (Payne & Peters, 2002).

In the wallaby cortex, layer 1 contains cell bodies that are sparsely populated and consists mainly of apical dendrite terminals from cells in the deeper layers. Layer 2 contains cells that are densely packed when compared to those of layer 3. The upper part of layer 3 is more densely packed than the bottom part of the layer (which most likely resembles layer 4b in Brodmann's scheme for primates). Layer 4 is the granular layer, which is populated by densely packed stellate cells and some small pyramidal cells. Layer 5 contains sparsely distributed medium and large pyramidal cells. The large pyramids are present near the top of the layer. The cells are much less densely packed than in layers 4 or 6. Layer 6 is populated with small pyramidal cells that are on the border with the white matter. The cell density in layer 6 becomes sparser closer to the white matter (Vidyasagar et al., 1992).

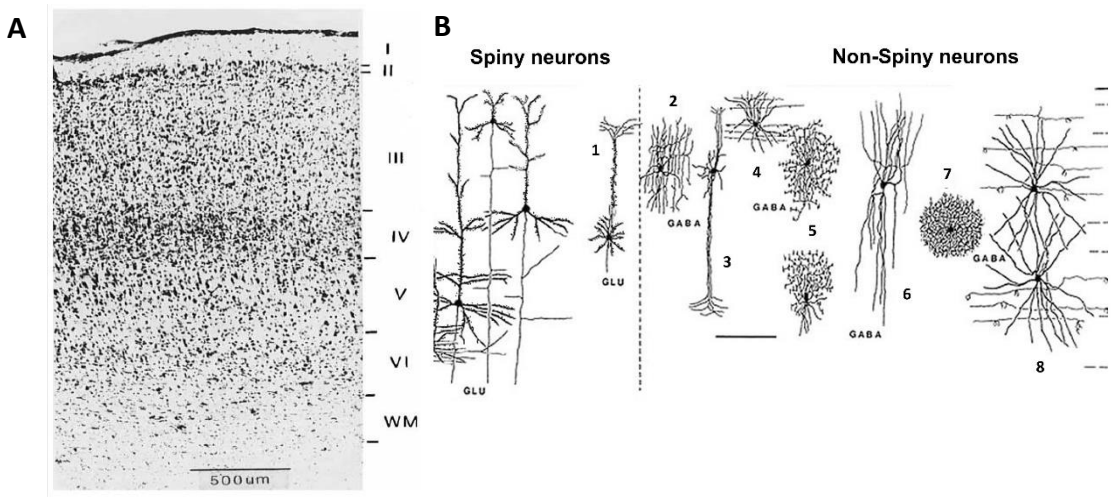

Figure 1.3 Nissl-staining preparation of the wallaby primary visual cortex showing six layers. Scale bar in 500 µm. Source: Vidyasagar et al. (1992). **(B)** Different cell types in the cerebral cortex. Left: 1. spiny neuron with neurotransmitter glutamate. Right: smooth cells with neurotransmitter GABA. 1. Cell with local axons; 2. Double bouquet cell; 3,8. Basket cells; 5. Chandelier cells; 6. Bitufted; 7. Glia cell. Source: Schmolesky (2007).

1.2.2 Physiological organisation of V1

Hubel and Wiesel were the first to discover the functional organisation and basic physiology of neurons in V1 in cat and monkey (cat: Hubel & Wiesel, 1962; monkey: Hubel & Wiesel, 1968). The spatial RFs of cells in V1 were first classified by stimulating neurons with moving bars into two types: simple and complex cells (Hubel & Wiesel, 1962). Simple cells are characterised as having RFs with distinct ON-OFF subregions, which are likely generated from the convergence of inputs from arrays of geniculate RFs (Figure 1.4). The ON-OFF subregions respond to opposite brightness polarities, the ON region to brightness increments and the OFF region to brightness decrements. Later studies have attempted to characterise neuronal RFs using the spike-triggered average (STA) analysis (Ringach et al, 2002; Rust et al., 2004; 2005; Nishimoto et al., 2006). The STA analysis recovers the RF of a neuron using the first-order moment of the spike triggered stimulus ensemble (i.e., the mean stimulus that elicited a spike), which has been effective in uncovering simple cell RFs (Chichilnisky, 2001; Ringach et al., 2002; Paniski, 2003; Schwartz et al., 2006). In general, simple cells have been found to show linear RF properties with position and contrast variance and orientation selectivity.

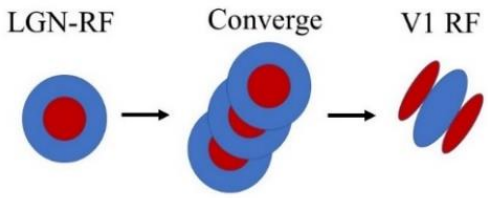

Figure 1.4 The classical hierarchical model of V1 cell receptive fields. The circular centre-surround RFs of several neurons in the LGN can lead to the elongated RFs observed in simple cells of the primary visual cortex.

Complex cells are characterised by the absence of distinct ON and OFF subregions and by their nonlinear summation properties. The convergence of simple cell RFs with similar orientation selectivity lead to the emergence of complex RFs. Figure 1.5 illustrates the convergence of three simple cells with the same orientation selectivity, which lead to the emergence of a complex cell. This RF structural

connectivity makes the complex cells orientation selective, but phase (position) invariant. More recently, spike-triggered covariance (STC) analysis, which computes the second-order moments of the spike-triggered stimulus ensemble, has been used to characterise the nonlinear filters of complex cells (Rust et al., 2005; Touryan et al., 2005; Chen et al., 2007). In contrast to simple cells, additional dimensions in the feature subspace of the complex cells make it difficult to uncover their RFs, as more data is required. Over recent years, parametric models have been used to capture a more physiological representation of the stimulus-response relationship of simple and complex cells. RFs were characterised by fitting the elicited neural data in response to stimuli, which was followed by a nonlinear a probabilistic spiking stage to account of the variability in the neuronal response (Touryan et al., 2005; Park & Pillow, 2011; McFarland et al., 2013; Liu et al., 2016). This analysis technique will be further explained in the Methods section from Chapter 3.

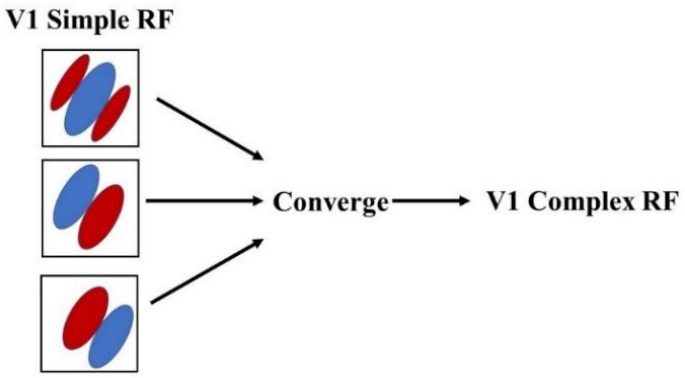

Figure 1.5 Complex RF generated from the convergence of the inputs from simple cells with similar orientation selectivity. The red and blue represent the ON and OFF subregions, respectively. The resultant complex cell has overlapping ON and OFF subregions.

The arrangement of the spatial RFs governs the response properties of cells in V1. For example, orientation selectivity of simple cells is directly influenced by the shape of their elongated ON-OFF subregions, controlled by inputs from LGN cells. Approximately 1.3 million LGN afferents project to V1 cells in macaques and ~ 0.5 million afferents in cat V1 (Mazade & Alonso, 2017). The orientation selectivity of complex cells is thought to be determined by the orientation of the simple cells providing input to the complex cell. For cells with non-oriented circular RFs, the

preferred orientation is evenly spread out from 0 to 180 degrees, whereas cells with clear ON-OFF subregions show clear orientation preferences. These cells respond optimally when a bar of light falls on the ON region and dark bar falls on the OFF region in the preferred orientation (Figure 1.6).

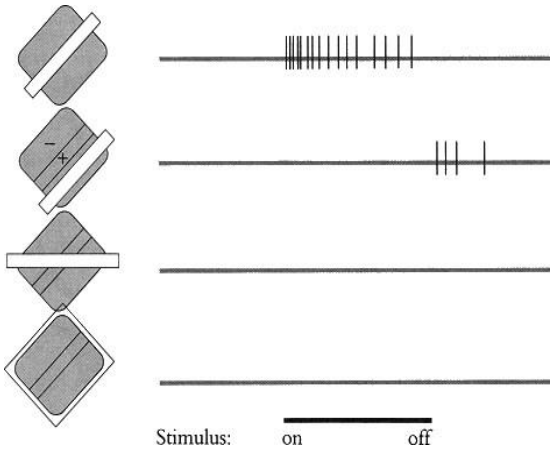

Figure 1.6 Illustration of various stimulus geometries that evoke different responses in cells. The left side shows the various stimulus geometries according to orientation and position. The stimulus line at the bottom represents the light bar being turned on and off. The vertical lines in the first and second recordings represent spikes elicited from the cells. The first recording shows the response to a bar of light with optimum size, position, and orientation. Source: Hubel and Wiesel (1962).

Using single-cell recording techniques, Ibbotson and Mark found that approximately 70% of the cells in the wallaby visual cortex are orientation selective (i.e. exhibit elongated RFs) while the other 30% of the cells are non-oriented (i.e. exhibit circular RFs) (Ibbotson & Mark, 2003). Cats and monkeys also have a high percentage of orientation-selective neurons in their visual cortex (65-70%; cats: Hubel & Wiesel, 1962; Ferster et al., 1996; monkeys: Hubel & Wiesel, 1968; Bullier & Henry, 1980).

1.2.3 Functional organisation of V1

Hubel and Wiesel (1968) first introduced the concept of columnar organisation when they observed clustering of cells with similar response properties across the layers in the monkey primary visual cortex. They found that neurons preferring the same orientation are clustered within an orientation column, and the neurons tuned to a slightly different orientation were clustered in an adjacent column. They also

observed clustering of cells based on inputs from either the left or the right eye. They found that neurons dominated by inputs from the same eye are grouped in an ocular dominance column. The area of the primary visual cortex containing a complete set of orientation columns (i.e. covers 180°) and ocular dominance columns of the left and the right eye is called a "hypercolumn" (Figure 1.7). Aside from columnar organisations, cytochrome-oxidase (CO) staining in primates revealed patchy patterns (blobs) in the supra-granular layers of the primary visual cortex which contained a high concentration of non-oriented, monocular, colour-selective neurons (Livingstone & Hubel, 1984).

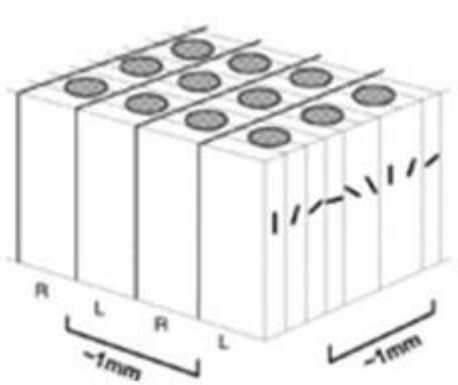

Figure 1.7 Schematic illustration of a hypercolumn, containing a complete set of orientation columns that represent 0–180°, one right and one left ocular dominance column, and several blobs. Source: hypercolumn image from Ts'o et al (2009).

Early studies have used tissue staining with radioactively marked 2-deoxyglucose injected into the blood to visualise the spatial patterns of ocular dominance and orientation columns in the mammalian primary visual cortex (Hubel et al., 1978; Schoppmann & Stryker, 1981; Kossut et al., 1983). Only the cells that are metabolically active absorb the 2-deoxyglucose markers and, in this way, it is possible to determine the spatial patterns of active and inactive cells. Using this technique, Hubel et al. (1978) revealed stripe-like forms of orientation and ocular dominance columns in monkey V1.

Later studies have used sensitive video or charge coupled device (CCD) cameras to image the neural activity of the cortex. In one technique, the changes in

the membrane potentials are imaged using signals from voltage sensitive dyes (Blasdel, 1992; Blasdel & Salama, 1986). In another technique, optical imaging of intrinsic signals reveals the changes in light absorbance and reflection of active areas of the cortical tissue (Grinvald et al., 1986; Bonhoeffer & Grinvald, 1996). During intrinsic optical imaging, areas with high levels of neural activity show less cortical tissue reflectance due to large blood volumes or increased deoxy-haemoglobin concentrations. In this way, it is possible to determine which areas of the cortex are active and which are not. In our study, we used the optical imaging of intrinsic signals to visualise the active areas of the visual cortex. This technique will be further explained in the Methods section of Chapter 2. This method showed that preferred orientation shifts continuously across the cortex, forming a regular two-dimensional orientation map (Bonhoeffer & Grinvald, 1991; Obermayer & Blasdel, 1993). As shown in Figure 1.8, the iso-orientation domains radiate around the 'orientation centre' and produce a pinwheel-like pattern in the map (Bonhoeffer & Grinvald, 1991). Similar to orientation columns, neurons that are tuned to the same direction of motion are clustered into direction columns across the visual cortex. For direction to be mapped with a complete cycle of orientation values (0 to 360°), each orientation needs to be mapped around an orientation pinwheel with two possible directions. As a result, there is a discontinuity in the direction map whenever adjacent cortical regions prefer opposite directions (Figure 1.8C) (Weliky et al., 1996). Moreover, Ohki et al. (2007) imaged the activity of neuronal populations in rat visual cortex at single-cell resolution using two-photon microscopy and found that orientation selective cells are randomly distributed in what is termed salt-and-pepper map. (Figure 1.8D).

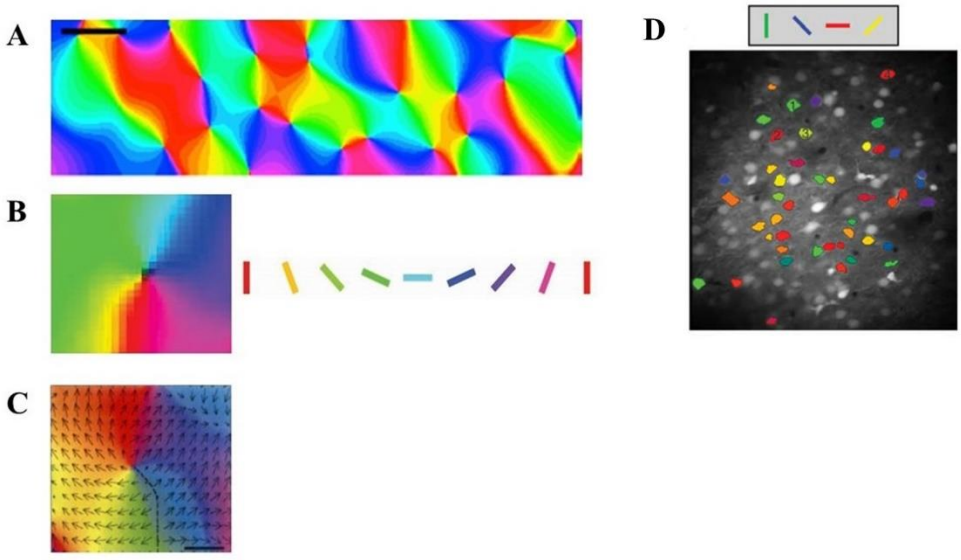

Figure 1.8 Functional maps in the mammalian visual cortex. **(A)** Orientation map of the cat striate cortex. **(B)** A single pinwheel structure zoomed to a square width of 1 mm. **(C)** Direction map around a single pinwheel from the ferret visual cortex. The black arrows show a continuous shift in direction preferences around the pinwheel up to the fracture point (dashed line) where the two cortical regions have opposite direction preferences. Scale bar, 200 µm. **(D)** *In vivo* images of calcium-stained cells in rat visual cortex, colour-coded according to their preferred orientation. Source: orientation map in a cat visual cortex from Cloherty et al. (2016), direction map in a ferret visual cortex from Weliky et al. (1996), orientation map in rat visual cortex with single-cell resolution from Ohki et al. (2005).

1.3 Origins of functional organisation in the Visual cortex

Over the past decades, researchers have obtained an increasingly detailed understanding of the anatomical and functional organisation of the visual cortex. Hubel and Wiesel (1962) first revealed that neurons in the cat primary visual cortex exhibit selectivity for the orientation of a bar or edge stimulus. They also described columnar systems in the visual cortex, where cells preferring the same orientation are clustered in an orientation column and cells dominated by inputs from the same eye are grouped in an ocular dominance column. Later studies using optical imaging techniques have confirmed the concept of functional organisation in the visual cortex (Blasdel & Salama, 1986; Bonhoeffer & Grinvald, 1991; Grinvald et al.,

1991; Obermayer & Blasdel, 1993). The pinwheel-like maps of orientation preferences are seen in most mammalian primary visual cortex (monkeys: Blasdel & Salama, 1986; cats: Bonhoeffer & Grinvald, 1991; ferrets: Chapman et al., 1996; tree shrews: Bosking et al., 1997).

However, more recently, it was found that rodents and rabbits do not have the same cortical structure; despite having robust orientation selectivity in individual cells, orientation-selective cells are randomly distributed across the cortex in what is termed salt-and-pepper OP maps (Ohki et al., 2005; Van Hooser et al., 2005; Bonin et al., 2011; Espinosa & Stryker, 2012; Reid, 2012). Many studies have tried to explain how the complex maps for orientation preference are created in the primary visual cortex (Swindale, 2004; Karim & Kojima, 2010; Paik & Ringach, 2011; Scholl et al., 2013; Vidyasagar & Eysel, 2015; Kremkow et al., 2016). However, it remains unknown why some mammals have random salt-and-pepper OP maps while others have pinwheel OP maps.

Several computational models have made important contributions to our understanding of how the cortical maps are created. Most developmental models of cortical maps suggest fixed intracortical connections with local excitation and long-range inhibition (e.g. Erwin et al., 1995; Miller et al., 1999). These ‘unsupervised’ simulations generate maps that closely reproduce pinwheel OP maps (Olshausen & Field, 1996; Cloherty et al., 2016). It was suggested that the 1–2mm inhibitory connections are responsible for the OP maps (e.g. Shouval et al., 2000). However, the same connections exist in squirrels (Kaas et al., 1989), which do not have pinwheel OP maps. Kaschube et al. (2010) analysed functional OP maps in the ferret, tree shrew, and galago (all with pinwheels) and found a common organizing principle. A symmetry-based class of models predicted all the essential features of the layout of the OP maps if long-range interactions dominate. As rodents and rabbits lack this ordered OP mapping it is possible that their cortices are dominated by local circuit connections, despite having the long-range connections available.

Some models of cortical development have expressly considered the structure of the retinal input. Goodhill and Sejnowski (1997) incorporated retinal

parameters (position and density) into their self-organizing 'feature space' model of cortical development (Goodhill & Sejnowski, 1997; Carreira-Perpinán et al., 2005). Another model suggests that the ON and OFF pathways in the retina both form near-perfect geometrical arrays of cells but that the two arrays are rotated relative to each other (Ringach, 2004; Paik & Ringach, 2011; Kremkow et al., 2016). Paik and Ringach's theory suggests that orientation selectivity is created in a later step in the visual hierarchy through interactions between the ON and OFF arrays (Paik & Ringach, 2011). Due to Moire interference patterns formed when the two arrays are superimposed, different patterns of OS could form in the cortex, which resemble pinwheel maps. If this is true, this model could allow us to determine whether a species has structured pinwheel maps. However, although the model is elegantly built, it is not biologically plausible. Several studies show that the mammalian RGCs (e.g. cats and monkeys) do not have the spatial distributions required to create perfect ON and OFF retinal mosaics, and in turn, for seeding the OP maps of the primary visual cortex (Hore et al., 2012; Schottdorf et al., 2014; Reese & Keeley, 2015). Many computational models for the generation of OP maps have incorporated Hebbian plasticity, intracortical interactions and the properties of growing axons. However, many of these models suggest that the whole story can be explained based on intracortical interactions.

In the following, I summarise the differences in cortical map structures found between mammals and outline many possible factors that may influence the type of OP maps created in the visual cortex (for review, see Ibbotson & Jung, 2020). These include: (1) the degree to which the animal is nocturnal, (2) whether the animal is a predator or a prey, (3) the size of the brain and sophistication of the cortical architecture, (4) the need for binocular vision, (5) genetic factors related to phylogeny, (6) the distribution of RGCs in the retina and the LGN, and (7) the emergence of orientation selectivity in the visual pathway. The following is a brief discussion on the factors (1–4), which are relatively easy to argue against.

(1) Evidence so far has not shown a correlation between the OP map structure and whether an animal is diurnal or nocturnal. Cats and some primates are primarily nocturnal, and they have pinwheel structures, whereas mice are

nocturnal even though they have salt-and-pepper maps. Moreover, squirrels have salt-and-pepper structures despite being diurnal.

(2) It is unlikely that there is a correlation between the OP map structure and whether an animal is a predator or prey. Rodents, a typical prey animal, have salt-and-pepper maps. However, it was found that a carnivorous rodent with predator instincts has a salt-and-pepper structure (Scholl et al., 2013).

(3) The notion that mammals with smaller primary visual cortices, less sophisticated cortices, or poor vision are restricted to having random salt-and-pepper structures can be rejected. A study by Van Hooser et al. (2005) found that squirrels have a highly differentiated cortex and good spatial resolution, but they have salt-and-pepper maps. Moreover, tree shrews (Fitzpatrick, 1996) have a V1 that is smaller than those of rabbits (Hughes, 1971), but they have pinwheel maps, while rabbits have salt-and-pepper maps. More recently, Weigand et al. (2017) proposed that mammals are more likely to organise their brain into columns when they have more cells in V1. It is true that cats and monkeys, which have a pinwheel structure, have clearly larger cortical cell populations (> 30 million cells in V1) than rodents in general (< 3 million cells in V1), which have salt-and-pepper maps. However, the difference in cell population is less marked when comparing the rabbit, which has a clear salt-and-pepper structure and 6 million cells in V1, with the ferret and tree shrews that have 7–8 M cells, despite their pinwheel structure. Hence, it is difficult to say that the “more cells, more complexity” theory explains the different types of OP map structures.

(4) The difference in OP map organisation cannot be linked to the location of the eyes in the head (frontal versus lateral) or the degree of binocular overlap. Figure 1.9 plots the binocular field overlap against the eye divergence for most animals that have had their OP maps measured. At first glance, it looks as though species with frontally positioned eyes and large binocular overlaps (Figure 1.9; blue writing: humans, macaques, squirrel monkeys, owl monkeys, bushbabies, and cat) have pinwheel maps, while

species with laterally positioned eyes with small binocular overlap (Fig. 1.10; red writing: squirrels, rats, mice, rabbits) have salt-and-pepper maps. However, tree shrews and ferrets (green diamonds) contradict this simple theory. Tree shrews and ferrets have quite laterally positioned eyes and small binocular overlaps, and yet they still have pinwheel maps.

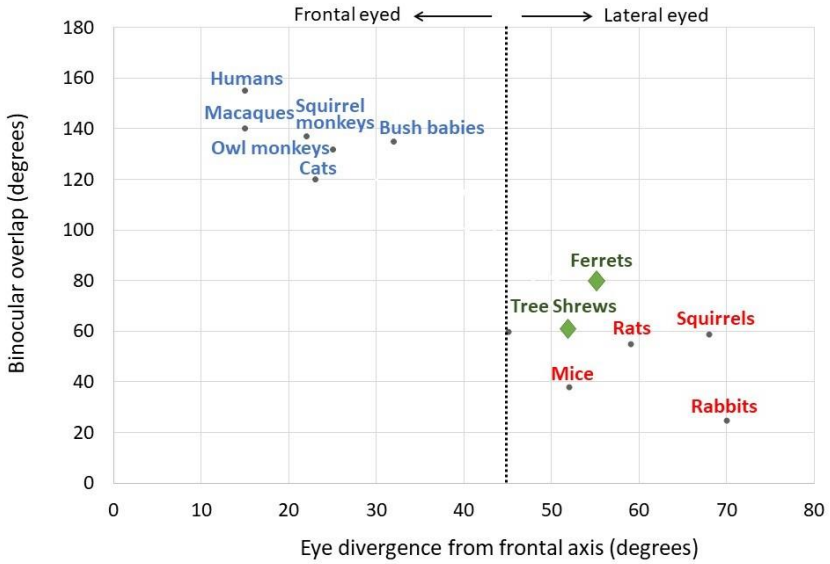

Figure 1.9 Binocular overlap plotted against eye divergence from direct front in mammals. The black vertical line shows an eye divergence of 45°, which divides frontal from lateral eyed animals. Species names in blue have pinwheel maps, while species names in red have salt-and-pepper maps. Ferrets and tree shrews have names and symbols in green: both have pinwheel maps. Source from: Ibbotson and Jung (2020).

1.3.1 Relationship between phylogeny and OP maps

Our understanding of the visual cortex in mammals comes mostly from studies on mice, cats, monkeys, and tree shrews. However, these species cover only a small subset of extant mammals in the phylogenetic tree. A simplified phylogenetic tree (Figure 1.10) (Springer et al., 2003; Luo et al., 2011) for mammals shows a large phylogenetic distance between primates (Clade Euarchonta) and carnivores (Clade Laurasitheria), both of which have pinwheel OP maps. Members of the mammalian order rodents and lagamorphs (Clade Glires), which are phylogenetically far closer to the primates than the carnivores, have salt-and-pepper maps. At present, the only discernable phylogenetic pattern found is that all Glires have a salt-and-pepper map

structure. Given that no other mammal studied so far has this structure, salt-and-pepper maps may be a genetically determined feature of the Glires. However, without adding more species from diverse mammalian orders, this conclusion cannot be verified. In this study, we decided to look into a highly visual Marsupial, the tammar wallaby, which are said to have split away from the Eutherian mammals ~160 million years ago (Samollow, 2008). From a phylogenetic standpoint, even if just one marsupial mammal has a pinwheel OP map, this could suggest that the genetic code for pinwheel maps existed for all mammals from the beginning, but, for some species (e.g. all mammals in the Clade Glires), the code was altered through later evolution to that of a salt-and-pepper map.

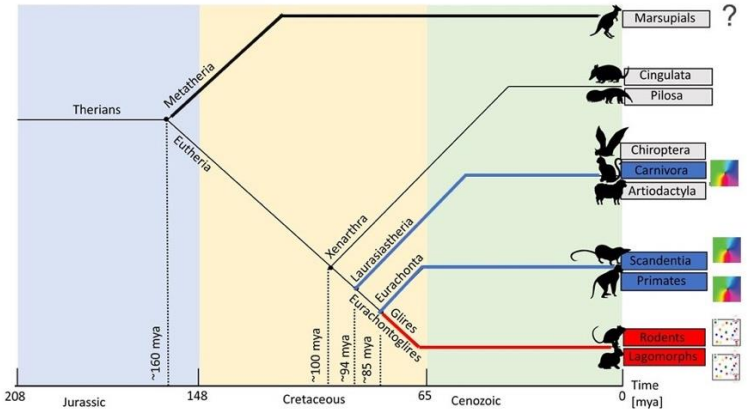

Figure 1.10 A simplified mammalian phylogenetic tree, with most detail on Eutherian mammals. Mammalian order names with blue backgrounds have pinwheels. Order names with backgrounds in red have salt-and-pepper. Order names in grey are those without optical imaging data. MYA, millions of years ago. Source: Ibbotson and Jung (2020).

1.3.2 Relationship between the density of cells in the retina and the thalamus and OP maps

Could the density of cells in the retina (RGCs) and LGN, which provide input to the cortex, affect the type of OP maps created? Mazade and Alonso (2017) proposed that for cells to cluster within different cortical domains, there needs to be sufficient spacing between thalamic axon patches. Consistent with their claim, species with pinwheel maps (e.g. cats, monkeys, and ferrets) have low densities of LGN axons (inputs form a single afferent) in V1, whereas species with salt-and-pepper maps

(i.e. rodents and rabbits) have high LGN densities in V1 (> 2000 axons/mm^2) as shown in Figure 1.11. The density of LGN cells in V1 decreases as V1 receives more inputs from LGN cells. As the number of LGN cells increases, the size of V1 increases in a nonlinear fashion (Stevens, 2001). For example, a human V1 has a surface area of ~2,400 mm^2, and it receives ~3.4 million LGN axons. The LGN-axon density in human V1 is about four times lower than that of the mouse, which distributes ~20,000 axons within ~4mm^2 of the V1 area (Mazade & Alonso, 2017). The spatial distribution of retinal inputs is an important factor determining the number of thalamic afferents to V1.

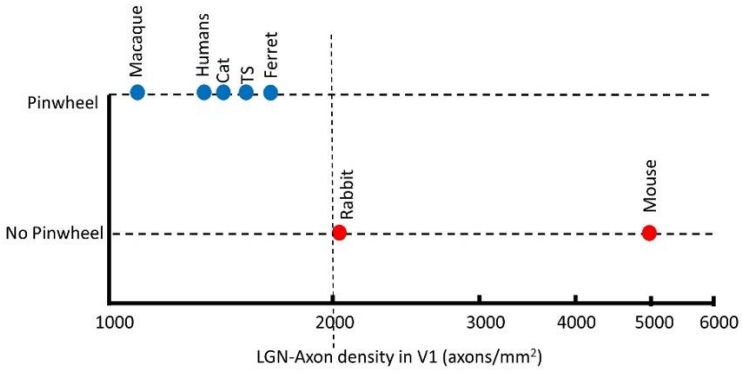

Figure 1.11 The LGN-axon densities in V1. Existence of pinwheels plotted against the LGN-axon density in V1. Red dots, no pinwheels; blue dots, pinwheels. The dotted vertical line shows an estimated and approximate threshold between species with pinwheels and those without. Source: Ibbotson and Jung (2020).

Different mammalian species have unique arrangements of retinal specialisations (areas of higher cell density), which appears to be influenced by ecological and developmental selective pressures in their ecological niches and habitats (Hughes, 1977; Collin, 1999; 2008). For example, the retinal inputs in rabbits are devoted to peripheral vision and offer a panoramic view of the environment, which gives them the best opportunity to look out for predators (Oyster et al., 1981). On the other hand, cats and primates have a strong retinal bias toward central vision to process high acuity vision, which increases the number of thalamic afferents to V1 (Kremkow & Alonso, 2018). For more detail on the different types of retinal designs refer to Ibbotson and Jung's (2020) review paper.

In our review paper (Ibbotson & Jung, 2020), we introduced the concept of the centre-to-periphery ratio (CP ratio), i.e. the ganglion cell density in the centre of the retinal specialisation divided by the peripheral cell density, to describe the spatial organisation of RGCs. Figure 1.12A illustrates the relationship between CP ratios and OP map design. We found that for a species with CP ratios < 4 (e.g. Red: rat, grey squirrel, mouse, and rabbit), the pinwheel map was absent. On the other hand, for species with a CP ratio > 7 (Blue: e.g. cat, sheep, ferret, and primates), the pinwheel map was present. Moreover, for some species with pinwheel maps, there was a strong linear correlation between CP factors and pinwheel density (Figure 1.12. $r^2 = 0.85$). The wallaby has a CP ratio of 20, which indicates that they have a strong centralised retinal input to the cortex. Based on this CP ratio, we propose that wallabies have pinwheel maps, and that the density of the pinwheels will be slightly lower than that of cats.

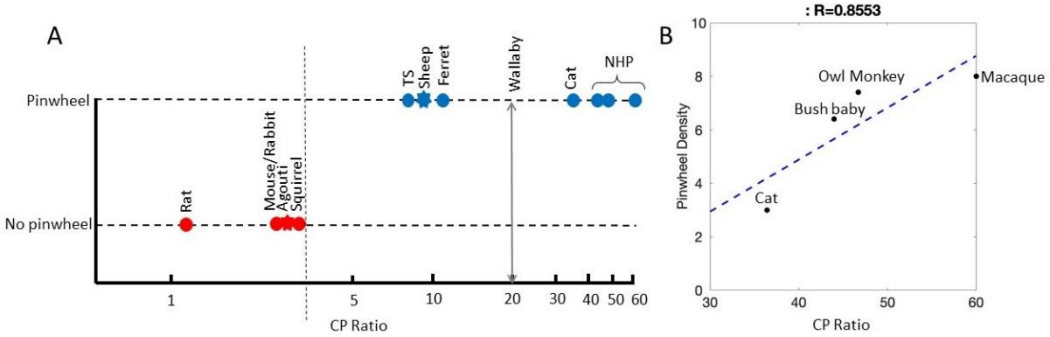

Figure 1.12 Relationship between organisation of RGCs and OP map structure. **(A)** Presence of pinwheels plotted against the CP ratios. Red, no pinwheels; blue, pinwheels. Circles show results from intrinsic optical imaging. Stars show results inferred only from single-cell recording. The dotted vertical arrow shows the possible threshold between species with pinwheels and those without. TS, tree shrew; NHP, non-human primates (including bushbaby, owl monkey, macaque). **(B)** For cat and primates, the pinwheel density (per mm^2) is plotted as a function of CP ratio. The linear regression is shown as a blue dashed ($r^2 = 0.85$). Source: Ibbotson and Jung (2020).

1.3.3 Selectivity in subcortical regions of the visual pathway and OP maps

The visual pathway to the cortex is from RGCs to lateral geniculate nucleus (LGN) to primary visual cortex (V1). It has been revealed that the LGN afferents that form

the input to mouse cortex are already orientation selective (Scholl et al., 2013; Sun et al., 2016). This is in contrast to cat and monkey cortices, where orientation selectivity in LGN neurons is weak or absent and OS is created *de novo* in cortex (Kremkow et al., 2016; Wilson et al., 2016; Lee et al., 2016). However, again the literature has been so focused on rodents, cats, or primates that it is not clear what influence the position at which orientation selectivity emerges in the visual pathway has on the development of cortical OP maps (Vidyasagar & Eysel, 2015). A comparative approach would be constructive in resolving this problem.

Our argument is that the existence of extensive orientation selectivity in LGN may disrupt the development of an ordered pinwheel OP map. It is possible that orientation-selective LGN cells send signals into V1 in a random spatial order, thus imposing a salt-and-pepper arrangement on the cortex. It is noteworthy that in all animals found to have salt-and-pepper OP maps, the diversity of retinal cells is high (e.g. rat: Wong et al., 2012). Conversely, in species with high CP ratios, there is reduced cell diversity in the central retina. (e.g. Dacey & Packer, 2003). In effect, to ensure high spatial resolution, the creation of more sophisticated response characteristics such as orientation selectivity appears to be pushed further up the visual pathway into the cortex. Therefore, we expect that animals with a high CP ratio are more likely to create OS in cortex *de novo* and that this, in turn, leads to more structured OP maps. In wallabies, we do not know where orientation selectivity emerges in the visual pathway. The present study will aim to record from the LGN and determine if OS occurs early on, as in the rodents or later in V1, as in cats and primates.

1.3.4 Why study the Marsupial tammar wallaby?

Mammals evolved from a large group of animals known as Therians. Mammals are defined as having mammary glands, true hair and three middle ear bones (Schiebinger, 1993). The Therians split into many types including Monotremes, Eutherians and Metatherians. The marsupials arose from a group of Metatherians. Marsupials split from Eutherian mammals around 130–180 mya (Dawson, 1983). Marsupials share many common traits with Eutherians but there are some obvious

differences in their tooth structure, reproductive systems and brain anatomy (e.g. Meyer, 1981; Lillegraven et al., 1987; Tyler et al., 1998; Wynne & McLean, 1999; Aboitiz & Montiel, 2003; Weisbecker & Goswami, 2010; Renfree, 2010). Regarding anterior commissure, Marsupials do not have a corpus callosum, which in Eutherians connects the two cortical hemispheres (Aboitiz & Montiel, 2003). However, marsupials, like Eutherians, do have a ventral brain pathway that connects the two cortical hemispheres via a longer route (Heath & Jones, 1971). Apart from this obvious difference in brain structure, other brain features are similar between Marsupials and Eutherians (e.g. Rocha-Miranda et al., 1973; Crewther et al., 1984; Vidyasagar et al., 1992; Rosa et al., 1999; Karlen & Krubitzer, 2007)

Specifically, for this thesis, the tammar wallaby has a primary visual cortex (V1) that has similar connectivity as V1 in well-known Eutherian mammals, such as cats and primates (Vidyasagar et al., 1992).This particular species was selected for a number of reasons, both scientific and practical. First, the tammar wallaby belongs to the largest Australian marsupial Order, the Diprotodontia, which has 137 extant species. The wallabies are small kangaroos and belong to the Suborder Macropodiformes and the Family Macropodidae. The Latin Family name means "large foot", which aptly describes the dominant feature of kangaroos and wallabies, which is that they stand on their large back legs and hop as their main form of fast locomotion. The common understanding of the kangaroo family is that they are ground-dwelling herbivores. There are in fact only four species of ground dwelling kangaroos, while there are thirteen species of tree-kangaroos. The latter are very well adapted to arboreal lives and have visual systems to match; e.g. the retina has an area centralis similar to the cat for high central vision (Hughes, 1977). There are 48 species of wallaby (including those that are extinct). The tammar wallaby belongs to the Genus *Macropus*. Wallabies range from quite large species that resemble small kangaroos through to very small species. Wallabies are generally very agile and are often very good at climbing, e.g. rock wallabies. The tammar wallaby represents a marsupial group that has relatively high spatial resolution vision, with central retinal densities similar to the cat (Wimborne et al., 1999). This offers a good comparison with the cat, which is studied in the same laboratory using the same equipment.

Second, the tammar wallaby has been the subject of numerous research projects over many years for which they are uniquely placed. Such topics include developmental and reproductive system (Shaw et al., 1988; Hinds et al., 1989; Tibben et al., 1991; Renfree et al., 1992; Renfree et al., 1996; Hickford et al., 2009), early neural development (Waite et al., 1994; Gummer & Mark, 1994; McCluskey et al., 2008) and comparative physiology (Meyer, 1981; Hemmi & Mark, 1998; Vidyasagar et al., 1992). The visual cortex of the tammar wallaby has been studied previously, providing an excellent baseline for the present study (Sheng et al., 1990; Vidyasagar et al., 1992; Hemmi & Mark, 1998; Wimborne et al., 1999; Ibbotson & Mark, 2003; Ibbotson et al., 2005). This is a major advantage for this thesis, as much of the preliminary knowledge about the retinotopic structure of wallaby cortex and its basic neuroanatomy and physiology is known (Vidyasagar et al., 1992; Ibbotson & Mark, 2003; Ibbotson et al., 2005).

Third, on a practical level, due to the use of wallabies for a range of projects, a colony is maintained at the University of Melbourne. As a result, the wallaby proved to be readily available for research purposes. Adult tammar wallabies' range in weight from about 3.5–7kg. As such, they are similar in size to domestic cats and, therefore, relatively easy to handle in a laboratory designed to work on cat cortex.

1.4 Importance of study

Understanding how the brain is organised is a primary goal in neuroscience worldwide. The neurons in the brain are intrinsically wired together to construct a functional brain. Although we have some understanding of the connections in the cortex and the functional implications of neuronal organisation, we are still far from understanding how the connections in the brain create a systematic map of features in the visual cortex. Many studies have attempted to provide insight into the origin of the functional architecture of the brain but, as mentioned above, we have a comparative problem in the literature. The present study will assist in filling a critical missing gap in the literature and provide a deeper understanding of the

functional organisation of the visual cortex. It is also the first investigation of maps in any marsupial cortex, with an importance all of its own.

Abbreviation	**Meaning**
RGCs	Retinal Ganglion cells
LGN	Lateral Geniculate Nucleus
V1	Primary visual cortex
RF	Receptive Field
CO	Cytochrome-oxidase
CCD	Charge coupled device
OP	Orientation Preference
OS	Orientation selectivity
MYA	Millions of years ago
CP	Centre-to-periphery
TS	Tree shrew
NHP	Non-human primates

Chapter 2

2.1 Introduction

The ability to detect the orientation of edges (orientation selectivity: OS) is a prominent feature of neurons in the mammalian primary visual cortex, but the spatial organisation of these neurons varies across species. In cats, ferrets, tree shrews and primates, orientation-selective neurons are organised into structured orientation columns, which are vertical arrays of neurons with the same orientation preference (Hubel et al., 1977; Blasdel & Salama, 1986; Bonhoeffer & Grinvald, 1991; Bartfeld & Grinvald, 1992; Obermayer & Blasdel, 1993; Hübener et al., 1997; Nauhaus et al., 2012). These columns are organised into two-dimensional orientation maps in which the different orientations are arranged radially around singular, pinwheel centres. However, rodents and lagomorphs (e.g. rabbits), despite having robust orientation selectivity in individual neurons, do not have orientation columns, but instead the neurons are randomly distributed throughout the cortex. This random organisation is referred to as a salt-and-pepper arrangement (rodents and rabbits: Van Hooser et al., 2005; Ohki et al., 2005; Bonin et al., 2011; Reid, 2012; Espinosa & Stryker, 2012).

The origins of the functional architecture of primary visual cortex remains a widely discussed topic in the field of visual neuroscience (Vidyasagar & Eysel, 2015; Kremkow et al., 2016; Jang et al., 2020; Ibbotson & Jung, 2020). We do not yet know why some mammals have structured pinwheel maps while others have salt-and-pepper maps. In chapter 1, I looked at several factors that may influence V1 structure, which included the phylogeny, the thalamocortical networks and, the topography of the retina. In this chapter, I aim to examine whether the development of OP maps is influenced by (1) a genetic factor related to phylogeny and (2) the topography of the retina by studying the arrangement of orientation selective cells in the primary visual cortex of a highly visual marsupial, the tammar wallaby (*Macropus Eugenii*). The marsupials (Metatherians) represent a phylogenetically distinct branch of mammals for which the orientation map structure is not known.

In this chapter, we use intrinsic optical imaging and multi-channel electrophysiological recording techniques to generate orientation preference maps (OP), direction preference maps (DP) and ocular dominance maps (OD) for the first time in a mammal that is not a member of the following mammalian Clades: Glires (e.g. rats, mice, squirrels), Laurasitheria (e.g. cats, ferrets) or Euarchonta (e.g. primates).

2.2 Methods

2.2.1 Experimental procedure

In vivo procedures

Recordings were made from six male adult tammar wallabies (12-24 months), each weighting between 3.9–5.7kg. The experiments were conducted using the facilities at the National Vision Research Institute (NVRI) and in accordance with the National Health and Medical Research Council's *Australian Code of Practice for the Care and Use of Animals for Scientific Purposes*. All experimental procedures were approved by the Animal Care Ethics Committee at the University of Melbourne (Approval ID: 1714178.1).

In each experiment, the animal was given lincomycin (10 mg/kg) and spectinomycin (20mg/ kg) intramuscularly, and paraffin oil (10ml) orally to reduce intestinal bloating during prolonged anesthesia. Ketamine (10mg/kg), medetomidine (0.015mg/kg), and methadone (0.4mg/kg) were administered intramuscularly for deep anaesthesia (absence of withdrawal and palpebral reflexes). During surgery, the animal was given phytomenadione (10mg/kg) and tranexamic acid (100mg/kg) intramuscularly to counter any bleeding. The animal was maintained on anaesthesia throughout the surgery with gaseous isofluorane (1–2% during surgery) and during the recording period with halothane (0.5% during recordings) with a 2:1 mix of O_2 and N_2O. We maintained the animal's body temperature at around 37ºC by a feedback-controlled heating blanket, and the CO_2 level was maintained between 3.0% and 5.0% with a mechanical ventilator. The stroke volume was set between 32-35ml and stroke rate was set between 30-32

breaths per minute. The head of the animal was stabilised with a stereotaxic frame and custom-made ear bars.

Using published stereotaxic coordinates and anatomical markers for area 17 (V1) (Vidyasagar et al., 1992; Ibbotson & Mark, 2003), we exposed small craniotomy windows (7 mm x 7 mm) in the left hemisphere of V1. The craniotomy window expanded 13–20 mm posterior to bregma and 3–10mm lateral from the midline. To expose more of the central visual field, in some experiments, we adjusted the craniotomy window to expand 9–16mm posterior to bregma and 7–14 mm lateral from the midline. The topographical mapping of wallaby V1 constructed in Vidyasagar et al.'s (1992) study was used as a reference point.

We performed a durotomy to expose the cortex and a stainless-steel chamber was affixed to the skull with dental cement. We applied 4% agarose in saline on the surface of the cortex to maintain the level of moisture. Neuromuscular blockade was initiated and maintained with vecuronium bromide (0.05mg/kg for induction and 0.1 mg/kg/h in 1ml of Hartmann's solution containing 5% glucose for constant intravenous infusion) to eliminate eye movements. For fluid replacement during the experiment, the animal received intravenous infusion containing Hartmann's solution (50% by volume) and 0.9% NaCl solution (50% by volume) at a rate of 2.5 ml/kg/h. Daily intramuscular injections of atropine (0.2 mg/kg), dexamethasone phosphate (1.5 mg/kg) and Clavulox (0.05 mL/kg) were given to the animal to reduce salivation, prevent cerebral oedema and control infection, respectively. The animal received atrophine sulphate eye drops (1%) daily to maintain pupil dilations and prevent retraction of the nictitating membranes. Zero-power gaseous permeable contact lenses were used to protect the corneas. The refractive errors were measured using retinoscopy and corrected with spherical lenses placed in front of the eyes to have the stimulus focused on the retina. After the conclusion of the experiment, we euthanised the animal with an intravenous injection of an overdose of barbiturate (sodium pentobarbital; 150 mg/kg).

Visual stimuli

Visual stimuli were generated with a ViSaGe visual stimulus generator (Cambridge Research Systems, Cambridge, UK) and displayed on a calibrated, gamma-corrected LCD monitor (ASUS VG248QE, 1920x1080 pixels, refresh rate 60Hz, 1ms response time) at a viewing distance of 30cm. The stimulus screen was presented in two positions, one frontally to stimulate the central visual field and the other laterally (45° from the frontal position) to stimulate the peripheral visual field. Visual stimuli involved luminance-defined oriented square-wave gratings (0.15 cycles/°) with a rectangular aperture (60° diameter) set to high contrast (Michelson contrast 100%). They drifted (temporal frequency 2Hz) in one of 16 directions equally spaced between 0° and 360° (0° was a horizontal grating moving upwards). Each stimulus direction was presented randomly across 30 trials, together with a blank condition (no gratings).

Optical imaging setup and data acquisition

The cranial chamber was filled with silicone oil and sealed with a glass coverslip to reduce the hydrostatic pressure on the surface of the cortex and to stabilise the cortex. We imaged the exposed area using a high sensitivity charge-coupled device (CCD) camera (Teledyne DALSA, Waterloo, ON Canada), which was fitted with a tandem macroscope consisting of two Nikkor 50mm f/1.2 lenses (Ratzlaff & Grinvald, 1991). The configuration of the camera was set to bin sensor pixels 2x2, resulting in an image resolution of 512 x 512 pixels (1 px = 24 µm square). For imaging, the focal plane of the camera was positioned 800–1000µm below the surface vasculature with a micromanipulator.

A custom-built LED light source (Agilent Technologies; HSMQ-C150) was used during imaging to epi-illuminate the exposed cortex from above with green light (540 nm). Conventionally, previous studies have used red light (wavelength > 600 nm) for intrinsic signal imaging, but as suggested in an earlier report (Cloherty et al., 2016), we decided to use green light (540 nm) to obtain a stronger signal-to-noise ratio. The component of the intrinsic signal that we could detect using green light was the localised blood flow in the stimulated regions of the cortex. Areas with large blood volumes or high deoxy-haemoglobin concentration as a consequence of increased levels of neural activity would show less cortical tissue

reflectance, and the resulting image would appear darker (Sirotin & Das, 2009; Sirotin et al., 2009). The green light revealed blood vessel artefacts on some occasions, which were overcome by applying more sophisticated analysis techniques than what some studies have used before. The analysis is further discussed in the Map generation section.

We imaged the cortical responses during the presentation of visual stimuli (as described above). Images were acquired continuously at a rate of 5 Hz for 10 seconds for each stimulus condition. The image acquisition started 2 seconds before the stimulus onset. The stimulus onset was synchronised to the phase of the respirator (i.e. stimulus turned on at maximum inspiration). The duration for each stimulus condition was 5 seconds. There was a recovery period of 3 seconds after each stimulus presentation, which displayed an isoluminant grey screen, with luminance equal to the mean luminance of the gratings.

2.2.2 Analysis of intrinsic optical imaging data

Map generation

MATLAB was used to process and analyse all optical imaging data. The raw images were spatially cropped to a region of interest. Regions with very low signal and minor artefacts (i.e. air bubbles, coverslip scratches, dura folds) were excluded. The images acquired before stimulus onset (i.e. reference images) were summed and subtracted from all subsequent images to remove any of the stimulus-independent patterns across images. This method is known as the first-frame analysis (Blasdel, 1992; Bonhoeffer & Grinvald, 1996). Trials from opposite directions of stimulus presentation were summed to obtain 8 orientation conditions and trials from 16 directions of stimulus presentation were used to obtain 16 direction conditions. For each stimulus condition, we averaged the pixels recorded from all trials. Overall, 50 imaging frames were collected for each of 8 orientation conditions (0°, 22.5°, …, 157.5°) or 16 direction conditions (0°, 22.5°, …, 337.5°). To remove baseline activity and any uneven illumination, the averaged images were subtracted by the image of the uniformly activated cortex called the “cocktail blank”. The cocktail blank was obtained by summing the responses from all stimulus conditions as described by Bonhoeffer and Grinvald (1996).

Each of the imaging frames were high-pass Gaussian filtered (σ = 20 pixels = 480μm) to remove the large-scale changes in illumination across the images. Figure 2.1 illustrates the effect of the high-pass filtering on OP maps. As we increase the size of the high-pass filtering patches, we introduce larger spatial scales in the maps and, as a result, the maps are blurred. The spatial scales that are larger than 500μm are commonly filtered out to be able to visualise orientation columns (Kaschube et al., 2003; Wang et al., 2015; Cloherty et al., 2016; Mohan et al., 2019). In Figure 2.1, the histograms below each map show the distribution of the orientations corresponding to maps produced with filters of different sizes. The distribution of the orientations changes subtly for maps produced using a sigma of 100–500μm, but the distribution changes more drastically as larger spatial scales are introduced. The signal strength after applying various filter sizes to the raw image was plotted, as shown in Figure 2.2. Following the filtering process, the magnitude of the signals that are left reduced greatly with filters of lower spatial scale. After considering the spatial scale requirement for orientation columns and the strength of optical imaging signals following the filtering process, we decided to use a sigma of 480μm, as described by Cloherty et al. (2016). The images were then low-pass Gaussian filtered (σ = 2 pixels = 48 μm) to fulfil the requirement of the extended spatial decorrelation (ESD) method, which assumes the sources to be smoothed. The signs of the reflectance values were reversed because a decrease in reflectance meant there was an increase in neural activity.

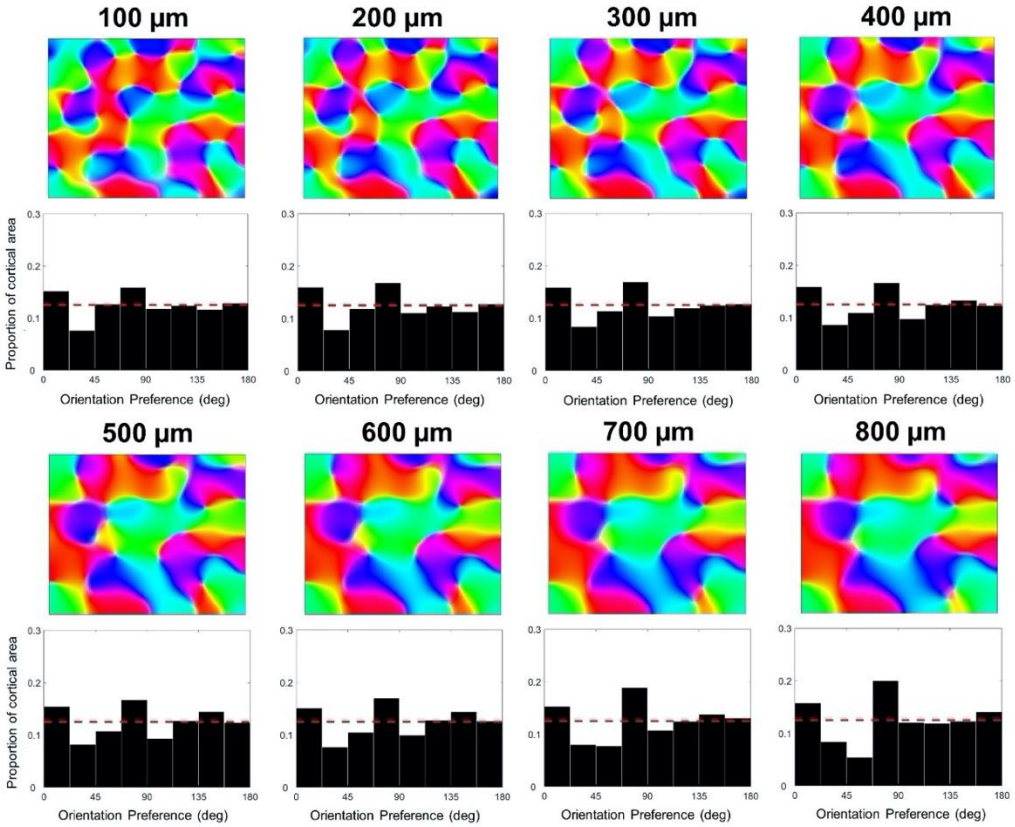

Figure 2.1 Effect of filter size on OP maps. Filters of different sizes (100µm to 800µm) were applied to the OI signal to examine the effect of high-pass filtering on OP maps. The angle (0-180°) is colour-coded on the OP maps. The sigma of the kernel applied to remove signals of a larger spatial scale is shown above each map. The image statistics change as the size of the high-pass filters increase. The OP maps are spatially blurred as we introduce a larger spatial scale. Below each map, a corresponding histogram shows the distribution of OPs across the region of interest. The red dashed line plots 1/8 frequency for equal proportions. As larger spatial scales are introduced, the distribution of the orientations become more biased towards 0° and 90°.

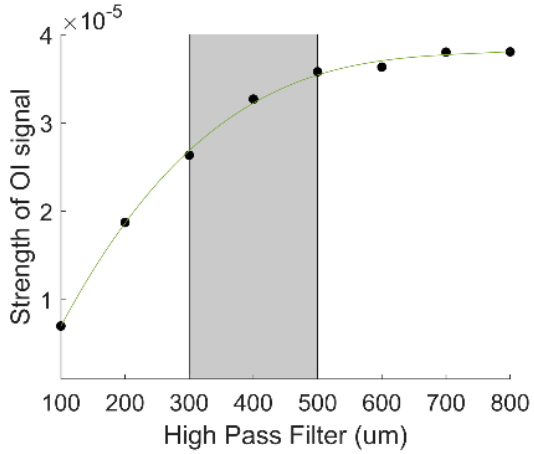

Figure 2.2 The magnitude of the OI signals following the filtering process with various filter sizes (100µm to 800µm). The grey shaded area denotes the commonly used high

pass Gaussian filters for visualisation of orientation columns.

Extended Spatial Decorrelation (ESD)

The ESD method described by Schießl et al. (2000) was employed to generate the feature maps. In principle, the ESD method relies on the second-order statistics of the data to convert individual imaging frames into separable components from different sources and ultimately separate stimulus-specific intrinsic signals from biological noise and artefacts (Schießl et al., 2000), a process known a blind source separation. Assuming that each source components is spatio-temporally separable, the changes in reflectance patterns can be written as:

$$S_j(r,t) = a_j(t)s_j(r), \qquad j = 1,\dots,N, \tag{2.1}$$

where $s_j(r)$ is the spatial pattern of the source, s_j, which is constant at all times for each frame, j and $a_j(t)$ represents the amplitude of the source, s_j. The overall optical imaging data set can be described as:

$$x_m(r) = \sum_{j=1}^{N} a_{mj}s_j(r) + n_m(r) \tag{2.2}$$

where a_{mj} is the amplitude in the m^{th} imaging frame, which gives rise to the time-course of the source (s_j), and $n_m(r)$ is the sensor noise produced during data collection (i.e. photon shot noise and camera readout noise). If the coefficients a_{mj} are combined in the form of a mixing matrix (A = $[a_{mj}]$), the statistical data model can be described as:

$$\boldsymbol{x}(r) = \mathbf{A}\boldsymbol{s}(r) + \boldsymbol{n}(r) \tag{2.3}$$

where $\boldsymbol{x}(r)$ is the pixel time series, which represents a single data point in the mixture space, $s(r)$ is the spatial component of the sources in the source vector, $s_1(r), \dots, s_N(r)$, and $n(r)$is the sensor noise.

The aim of the ESD method is to find the demixing matrix W, which can effectively reconstruct the sources from their noisy mixtures, $\hat{s}(r) = \mathrm{W}\boldsymbol{x}(r)$, from a statistical independence criterion on the original sources. This assumption is that

the sources are temporally and spatially uncorrelated with each other. The cross-correlation function used to decorrelate the two source patterns $s_l(r)$ and $s_m(r)$ can be written as:

$$C_s^{lm}(\Delta r) = \frac{1}{Q}\sum_r s_l(r)s_m(r+\Delta r) \tag{2.4}$$

where the shift Δr is often called the lag of the correlation function and each lag Δr delivers one value $C_s^{lm}(\Delta r)$and as the number of overlapping pixels between s_l and $s_m$decreases with the size of Δr we normalise with the value Q, that is the number of pixels the two sources still have in common.

As a first step in ESD, different sources s_l and s_m are decorrelated in time from each other using the zero-shift correlation matrix of $\boldsymbol{C}_s\ (0)$.

$$\boldsymbol{y}(r) = \boldsymbol{\Lambda}_0^{-1/2}\,\boldsymbol{V}_0^T\,\boldsymbol{x}(r), \tag{2.5}$$

where $\boldsymbol{y}(r)$ is the decorrelated signal, $\boldsymbol{\Lambda}_0$ is a diagonal matrix with the eigenvalue of $\boldsymbol{C}_s\ (0)$ along the diagonal and $\boldsymbol{V}_0^T$ is the matrix of corresponding eigenvectors arranged in rows. This transforms the sources to have identity covariance. Second, the sources s_l are decorrelated in space by using shifted versions of s_m, i.e. $C_s^{lm}(\Delta r)$ vanished for all Δr. A shift of Δr = (5,5) pixels was used to perform the single shift ESD. This decorrelation matrix, U, is the solution of the eigenvalue equation:

$$(\boldsymbol{C}_s\ (\Delta r) + \boldsymbol{C}_s\ (-\Delta r))\boldsymbol{U} = \boldsymbol{\Lambda}_{\Delta r}\,\boldsymbol{U} \tag{2.6}$$

The overall demixing matrix, W was obtained by multiplying the decorrelation derived from the zero-shift correlation matrix, $C_s^{ml}(0)$ and the second decorrelation matrix derived from $C_s^{lm}(\Delta r)$.

$$\boldsymbol{s}(r) = \boldsymbol{U^{-1}}\boldsymbol{\Lambda}_0^{-1/2}\,\boldsymbol{V}_0^T\,\boldsymbol{x}(r), \tag{2.7}$$

The demixing matrix, W was then applied to the noisy mixture to generate 50 decorrelated signal components. The time course of the coefficients (i.e. which is the inverse of the demixing matrix) derived from each source was plotted to

determine which of the sources corresponded to stimulus presentation (Figure 2.3A). In most cases, the correct source was obvious, as the time series resembled the typical signal from the intrinsic optical imaging response (i.e. a rise at the time of stimulus onset and maximal at the stimulus off-set). Figure 2.3B illustrates the five decorrelated sources corresponding to plots in Figure 2.3A. It is clear from the dark patches present in the first source that it is the correct one corresponding to the stimulus-specific intrinsic signal and the rest of the sources are most likely due to biological noise or blood vessel artefacts. Each frame of the correct source was multiplied by its corresponding coefficient as an estimate of the response signal in the data, and the map for each stimulus condition was created by averaging the final 5 stimulus frames (i.e. frames with the highest signal). We removed any remaining high-frequency noise caused by the remaining blood vessel artefacts by applying low pass Gaussian filters (σ = 5 pixels= 120μm) onto the map.

Figure 2.3C shows examples of two OP maps generated: the one on the right derived from the ESD method and the one on the left derived from a more conventional approach, i.e. based on the calculation of differential image, where orthogonal stimuli are subtracted from each other (introduced by Blasdel, 1992). The spatial patterns of the map derived from the ESD method is not greatly different from the map using the conventional method. So, while ESD employs a more sophisticated analysis technique to separate stimulus-specific intrinsic signals from the biological noise and artefacts, the method does not produce maps that are considerably different to conventional methods for analysis of optical images.

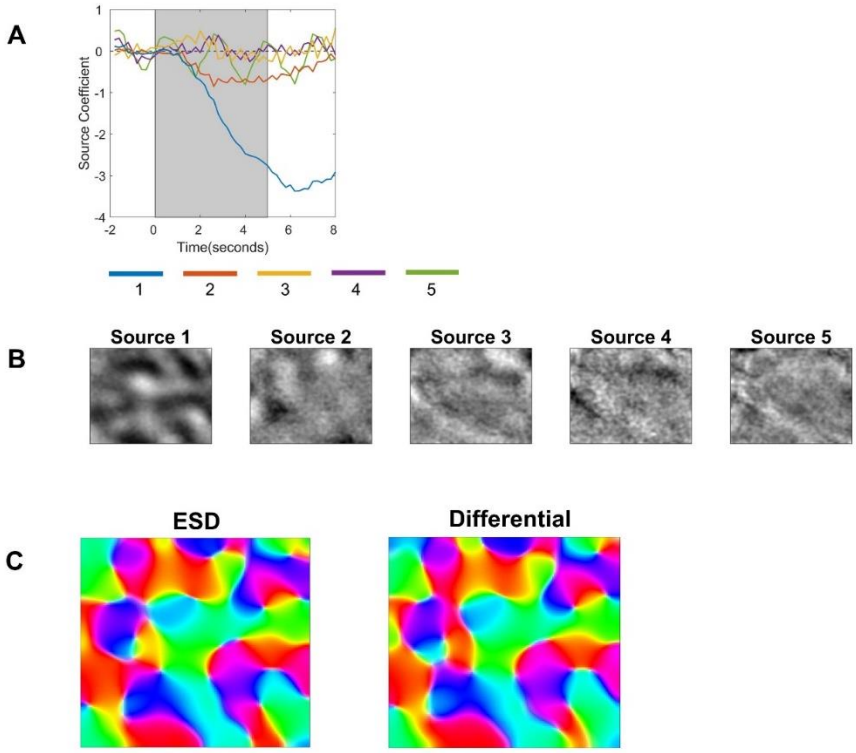

Figure 2.3 ESD separates mapping signal from green light imaging. **(A)** Time course of the separated components (sources 1–5). The grey shaded region shows the stimulus period (5 seconds). It is clear that source 1 is the mapping signal as the time course represents the change in absorption during the presentation of visual stimuli. **(B)** The corresponding reconstructed sources. **(C)** OP maps generated from the ESD and the conventional approach, i.e. differential imaging where orthogonal stimuli are subtracted from each other. While ESD removes any biological noise and artefacts from the map, the spatial patterns of the two maps derived using two different techniques can be similar.

Orientation Preference map

To visualise the organisation of orientation preferences across the visual cortex, the monocular OP maps were generated by vectorially summing the supplied single condition maps (Blasdel, 1992). The two vector components of the OP map were obtained by summing the responses to 8 stimulus conditions for each pixel. Let $R_{\theta,R}$ be the sum of responses to orientation θ produced by the right eye, and likewise for the left eye:

$$\text{real(OP)} = \sum_{\theta} \left(R_{\theta,R}\right) \cos(2\theta) \tag{2.8}$$

$$\text{imag(OP)} = \sum_{\theta} \left(R_{\theta,R}\right) \sin(2\theta)$$

where θ values in the sum were 0°, 22.5°, …, 157.5°. For each pixel, the angle of

the resulting complex number was converted back to orientation between 0 and 180 degrees by dividing by 2, and colour-coded.

Direction Preference map

The layout of direction preferences across the cortex was determined by vectorially summing the single condition maps obtained from 16 directions. The two vector components of the DP map were obtained by summing the responses to 16 stimulus conditions for each pixel. Let $R_{\theta,R}$ be the sum of responses to direction θ produced by the right eye, and likewise for the left eye:

$$\begin{aligned} \text{real(DP)} &= \sum\nolimits_{\theta} \left(R_{\theta,R}\right) \cos(\theta) \\ \text{imag(DP)} &= \sum\nolimits_{\theta} \left(R_{\theta,R}\right) \sin(\theta) \end{aligned} \tag{2.9}$$

where θ values in the sum were 0°, 22.5°, …, 337.5°. For 2x2 pixels, the angle of the resulting vector was indicated by the direction of arrows.

Ocular Dominance map

The OD map was obtained by summing the responses to orientation θ produced by the right eye and subtracting the sum of responses to orientation θ produced by the left eye.

$$OD = \sum\nolimits_{\theta} R_{\theta,R} - \sum\nolimits_{\theta} R_{\theta,L} \tag{2.10}$$

where θ values in the sum were 0°, 22.5°, …, 157.5°.

Analysis of Orientation Preference maps

For all the OP maps obtained, each pixel was binned according to its preferred orientation into 22.5° wide orientation preference bins positioned on 11°, 33.75°, ..., 168.75°. These orientation bins were set to produce a histogram, which illustrates the proportion of cortical area representing different orientations.

The sizes of iso-orientation domains were measured from the single condition maps obtained, in which dark areas represent regions that were strongly active to one particular orientation. Each image was thresholded to include only the active domains that have the top 25% darkest pixels, as previously described by Xu et al. (2004). The Image Processing Toolkit (in Matlab) was used to draw contours

around selected domains and to measure the domain sizes.

Pinwheel locations were determined using the method previously described by Carreira-Perpinan et al. (2005). For each pixel, the winding number was calculated by summing the increments of orientation angle in [(−π/2), (π/2)] along a closed path of radius 1 pixel and dividing it by 2 π. The winding number is 0 for non-pinwheel points and +1/2 or -1/2 for pinwheel points that have orientation angles increasing around the pinwheel in a clockwise or anticlockwise direction, respectively. The exact location of a pinwheel was determined by clustering pixels with nonzero winding numbers and computing their centres of mass. The pinwheel density was determined by counting the number of pinwheel centres in the region of interest and dividing the total count by the area (mm^2) as described previously by Bonhoeffer and Grinvald (1996).

Analysis of Ocular Dominance maps

An ocular dominance index (ODI) was calculated for each responsive pixel as follows:

$$ODI = \frac{\left|R_{R+R_L}\right|}{R_R + R_L} \tag{2.11}$$

where R_R and R_L represents the sum of responses to orientations θ presented monocularly to the right and left eye, respectively. The median of the ODI scores across all responsive pixels was determined. ODI ranges between -1 and 1, where negative values represent ipsilateral dominance and positive values represent contralateral bias.

2.3 Results

We used optical imaging of intrinsic signals to examine feature maps in V1 of six anaesthetised adult tammar wallabies. As tammar wallabies have a wide visual field and the optical axes of its eyes are diverged by 45°, the stimulus screen (60° wide and 15° elevated) was presented in two positions, one frontally to stimulate the central visual field and the other laterally (45° from the frontal position) to stimulate the far periphery of the visual field. We presented grating stimuli to each eye separately to visualise various feature maps. OP maps, DP maps and OD maps were obtained for the first time in the tammar wallaby visual cortex. Below, we look at each feature map in more detail.

2.3.1 Orientation Preference maps in the central visual field

We obtained OP maps in the central visual representation of V1 from two wallabies. Figure 2.4A shows examples of single condition maps we obtained from one of the imaged cortices. The dark patches represent regions in the cortex that were activated by the corresponding stimulus condition. The greyscale bar on the side represents the response magnitude in fractions. The iso-orientation domains preferring oblique orientations (i.e. 45° and 135°) appear round or irregular in shape, with an average diameter of 0.52 ± 0.12mm (mean ± SD measured from two wallabies). In contrast, the iso-orientation domains preferring cardinal orientations (i.e. 0° and 90°) appear as elongated patches, with an average width of 0.53 ± 0.13mm and length of 0.8 ± 0.16 mm (mean ± SD measured from two wallabies).

To examine the organisation of orientation columns, the eight single condition maps (for the same case shown in Figure 2.4A) were vectorially summed as described in the Methods. Figure 2.4C shows the OP map computed with each pixel colour-coded according to the orientation that elicited the maximum response for one wallaby. The colour scheme is displayed on the side of each OP map. Patches with different orientation preferences are organised radially around orientation centres, but the pinwheel-like patterns of orientation columns are not uniform across the cortex, in contrast to the lattice-like organisation observed in

cats and primates (Blasdel & Salama, 1986; Bonhoeffer & Grinvald, 1991; Obermayer & Blasdel, 1993; Hübener et al., 1997). The iso-orientation domains preferring cardinal angles (i.e. cyan and red) are over-represented in the cortex. For example, in Figure 2.4C, a large portion in the centre region of the OP map is occupied by iso-orientation domains preferring horizontal orientations (cyan and green). Similarly, a large portion in the left region of the OP map is occupied by iso-orientation domains preferring vertical orientations (red and orange). Figure 2.4D shows a histogram of the proportion of cortical areas devoted to different orientations in the OP map shown in Figure 2.4C. Each pixel was binned according to its preferred orientation into eight bins of size 22.5°. The red dashed line represents a uniform distribution of orientations. 59% of cortical space represented cardinal angles (i.e. orientations between 157.5°–22.5° and 67.5°–112.5°) and 41% represented oblique angles (i.e. orientations between 22.5°–67.5° and 112.5°–145°). Hence, the percentage of cortical area activated by cardinal angles was greater than that for oblique angles.

To further analyse the layout of the iso-orientation domains, we determined the spatial density of the pinwheel centres. The pinwheel locations were determined as described in the Methods. Figure 2.4E shows the contours of all the iso-orientation domains in Figure 2.4C, and the locations of pinwheel centres are marked as black dots. The pinwheels occurred at a density of 1.63 pinwheels/mm^2. Zooming into a region of approximately 1 x 1 mm^2, containing a full set of orientation preferences, we can clearly see the smooth transition of orientation columns around a singularity. However, note that the size of pinwheels varies widely across the cortex (from 0.7mm–1.2mm in diameter). This is because the pinwheel-like patterns of orientation columns are not uniform across the cortex.

When we carried out the same experiment on another wallaby, we again observed iso-orientation domains arranged radially around pinwheel centres, as shown in Figure 2.5B. Moreover, the over-representation of cardinal orientations in the cortical area was more prominent in the second animal compared to the first animal (Figure 2.5C). The percentage of cortical space devoted to cardinal angles was 70%, and 30% for oblique angles. Figure 2.5D shows the pinwheel locations marked as black dots from this case. The pinwheel density was measured to be 1.46

pinwheels/mm^2. Overall, the analysis of two OP maps measured from the central visual representation of V1 revealed an average pinwheel density (n = 2) of 1.60 ± 0.12 pinwheels/mm^2 (mean ± SD).

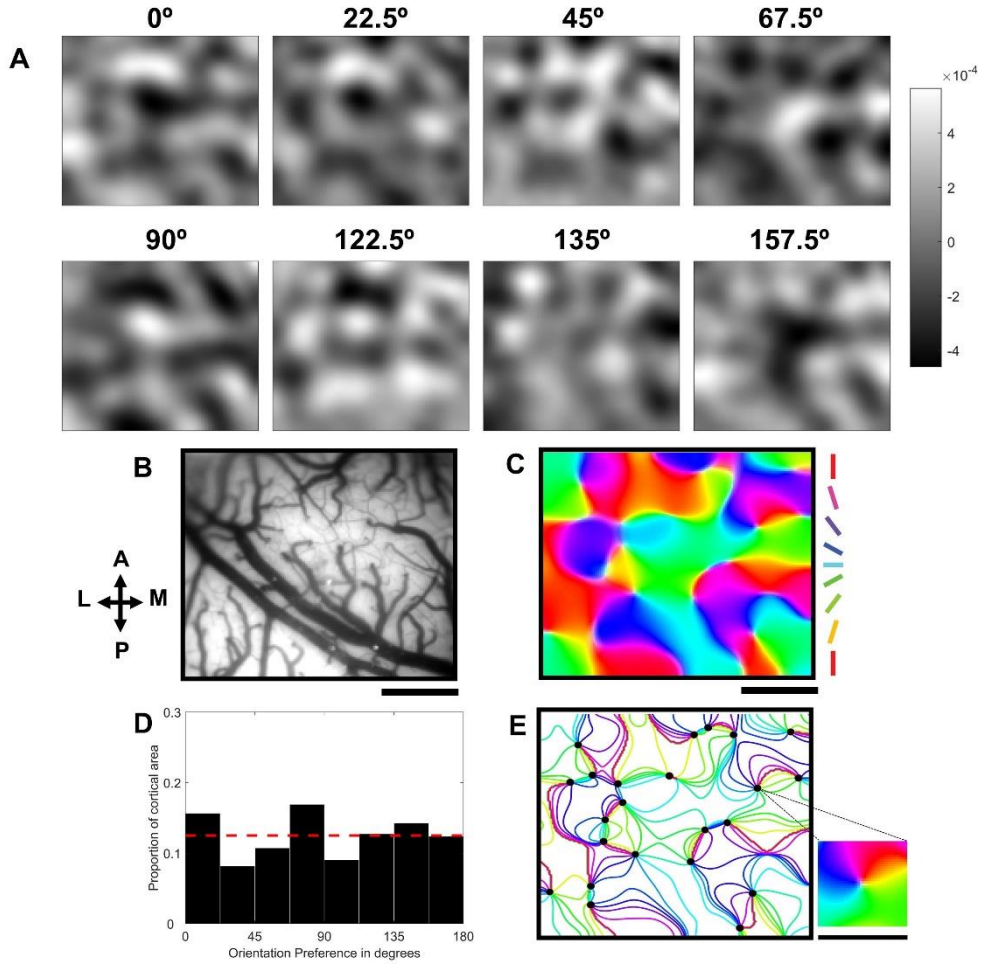

Figure 2.4 OP map obtained in the central visual field of wallaby V1 (animal W1). **(A)** Eight single condition maps in response to moving gratings. The greyscale represents the response magnitude (dark areas represent high activity). **(B)** The image of the cortical surface illuminated with green light. A, Anterior; P, posterior; M, medial; L, lateral. **(C)** OP map showing the preferred orientation for every region of interest. The angle is colour-coded according to the scheme in the legend. **(D)** Proportion of cortical area representing different orientations from right eye stimulation. The red dashed line at a frequency of 1/8 represents uniform distribution. **(E)** OP contours showing the organisation of all the orientation columns and black dots representing pinwheels. 23 pinwheel centers located within 14.1mm^2 cortical area. Pinwheel density = 1.63 pinwheels/mm^2. The inset shows a zoom-in onto a single pinwheel. Square width = 1mm. Scale bar =1mm.

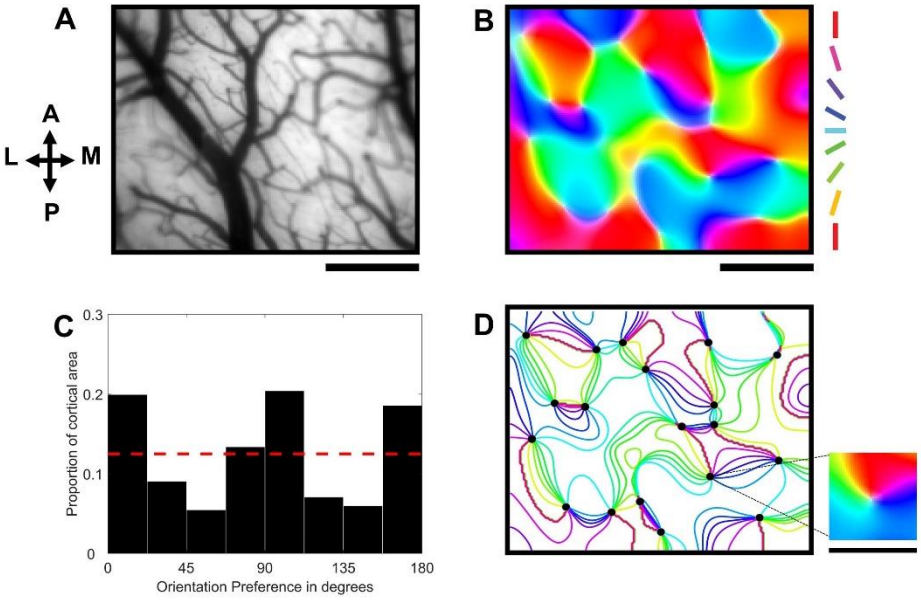

Figure 2.5 OP map obtained in the central visual field of another wallaby (animal W2) V1. **(A)** The image of the cortical surface illuminated with green light. A, Anterior; P, posterior; M, medial; L, lateral. **(C)** OP map showing the preferred orientation for every region of interest. The angle is colour-coded according to the scheme in the legend. **(D)** Proportion of cortical area representing different orientations from right eye stimulation. The red dashed line at a frequency of 1/8 represents uniform distribution. **(E)** OP contours showing the organisation of all the orientation columns and black dots representing pinwheels. 18 pinwheel centers located within 12.29 mm^2 cortical area. Pinwheel density = 1.46 pinwheels/mm^2. The inset shows a zoom-in onto a single pinwheel. Square width = 1 mm. Scale bar = 1 mm.

2.3.2 Orientation Preference maps in the peripheral visual field

We obtained OP maps in the peripheral visual field representation of V1 from four wallabies. For this experiment, the craniotomy window and visual stimulus position were adjusted on the basis of a well-established visuotopic mapping of wallaby V1 (Vidyasagar et al., 1992), as described in the Methods. Figure 2.6A shows an example of the single condition maps we obtained in one of the imaged cortices, representing peripheral vision. The activated regions run medio-lateral along the cortical surface in beaded bands. The dark patches of strong activation are connected by lighter regions of weaker activation. These beaded domains within bands appear at approximately equal intervals and have an average width of 0.51 ± 0.14mm and length of 0.73 ± 0.15mm (mean ± SD measured from four wallabies). Figure 2.6C shows the colour-coded OP map obtained from vectorially summing the eight single condition maps shown in Figure 2.6A. The iso-orientation domains

in bands are organised linearly parallel to the medial-lateral axis of the cortical surface. Pinwheel centres can be found at the edges of these linear bands, but they are not present uniformly across the cortex. Figure 2.6E shows that pinwheel centres are sparsely located across the cortex, and as a result, the pinwheels occurred at a low density of 0.75 pinwheels/mm^2. Figure 2.6D shows the proportion of cortical area representing different orientations, with 72% of the cortical space devoted to cardinal angles and 28% representing oblique angles.

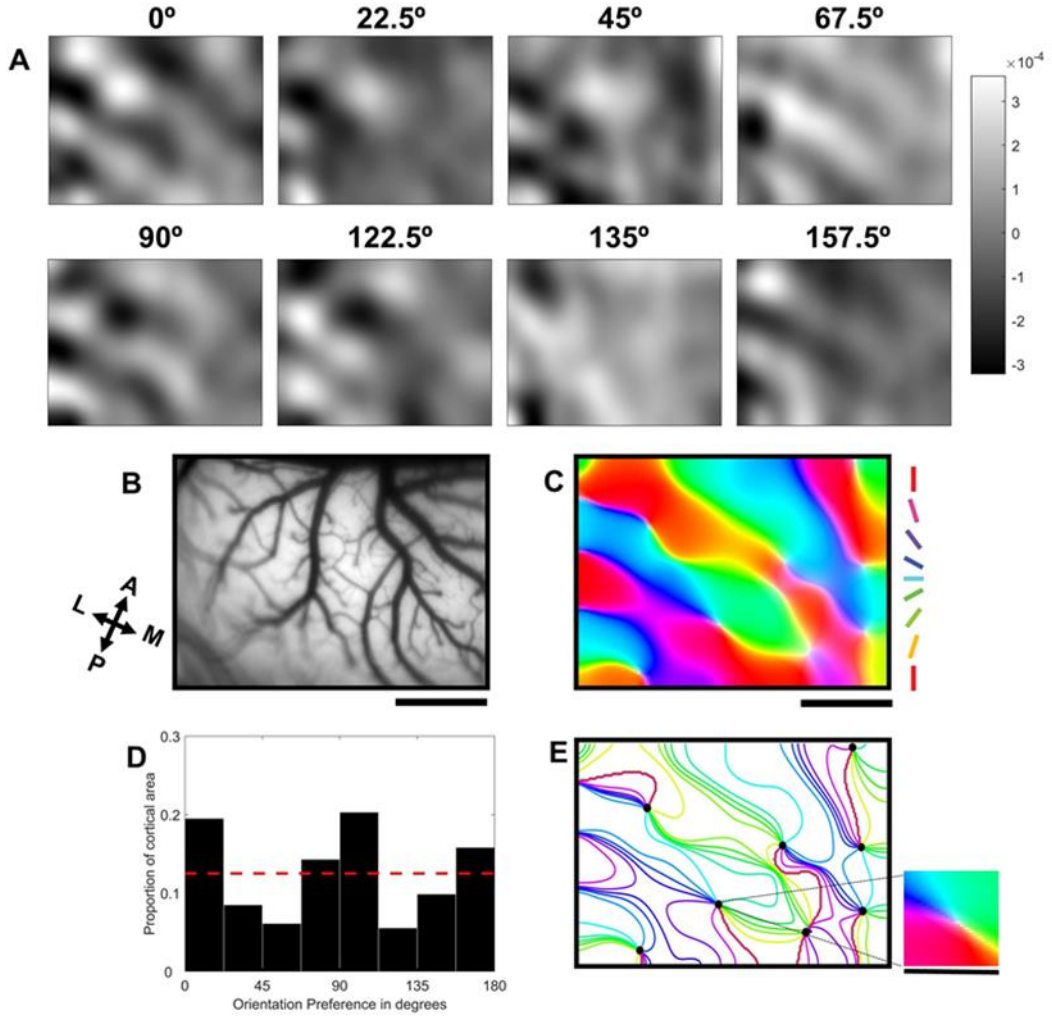

Figure 2.6 OP map obtained from the peripheral visual field in V1 of wallaby number W3. **(A)** Eight single condition maps in response to moving gratings. The grey colour bar represents the response magnitude (dark areas represent high activity). **(B)** The image of the cortical surface illuminated with green light. A, Anterior; P, posterior; M, medial; L, lateral. **(C)** OP map showing the preferred orientation for every region of interest. The angle is colour-coded according to the scheme in the legend. **(D)** Proportion of cortical area representing different orientations from right eye stimulation. The red dashed line at a frequency of 1/8 represents uniform distribution. **(E)** OP contours showing the organisation of all the orientation preference domains and black dots representing pinwheels. 8 pinwheel centers located within 10.6 mm^2 cortical area. Pinwheel density = 0.75 pinwheels/mm^2. The inset shows a zoom-in onto a single pinwheel. Square width = 1mm. Scale bar = 1 mm.

When we imaged from the same area and stimulated the peripheral visual field with three other wallabies, we again found the coexistence of radial and linear organisation of iso-orientation domains. Figure 2.7–Figure **2.9** present OP maps from three other animals where we measured the peripheral visual field representation. Like the OP map presented in Figure 2.6, each map is dominated by vertical and horizontal preferences that run in beaded patterns across the medial-lateral axis of the cortical surface (Figure 2.7–Figure **2.9**B). The over-representation of cardinal orientations can also be seen in Figure 2.7–Figure **2.9**C. The average percentage of cortical space representing cardinal angles measured in four cases for peripheral vision was 75.5 ± 2.6% (mean ± SD measured from four wallabies). In the OP maps shown in Figure 2.7–Figure **2.9**D, we can also observe pinwheels at the edges of the bands. Overall, the analysis of four OP maps measured for peripheral vision revealed an average pinwheel density (n = 4) of 1.06 ± 0.21/mm^2 (mean ± SD).

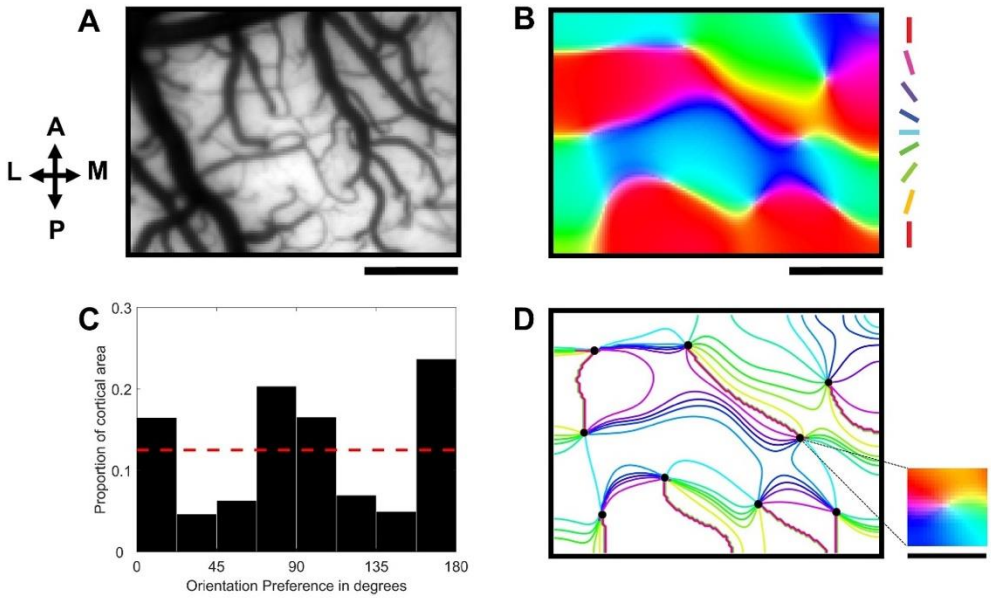

Figure 2.7 OP map obtained from Wallaby W4. **(**See the collective legend for 2.7 to 2.9 below for more detail).

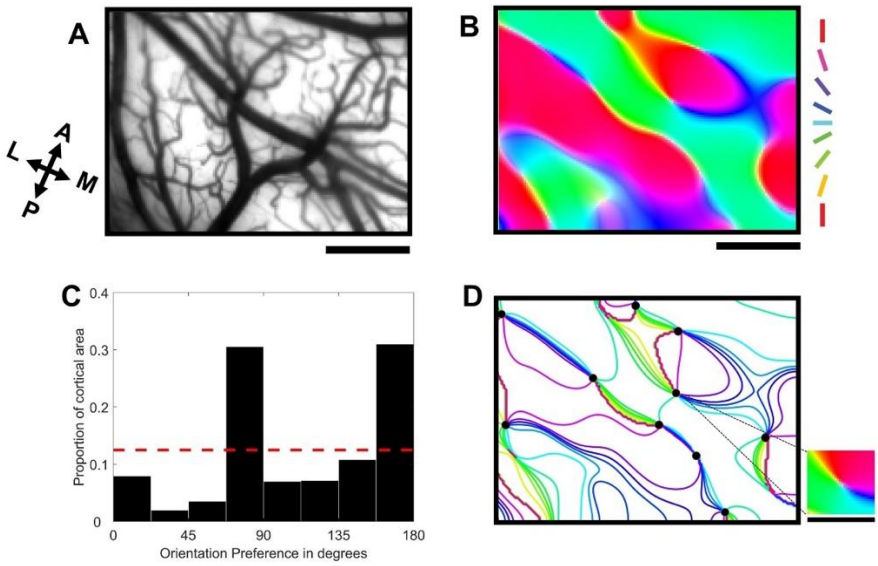

Figure 2.8 OP map obtained from Wallaby W5**. (**See the collective legend for 2.7 to 2.9 below for more detail).

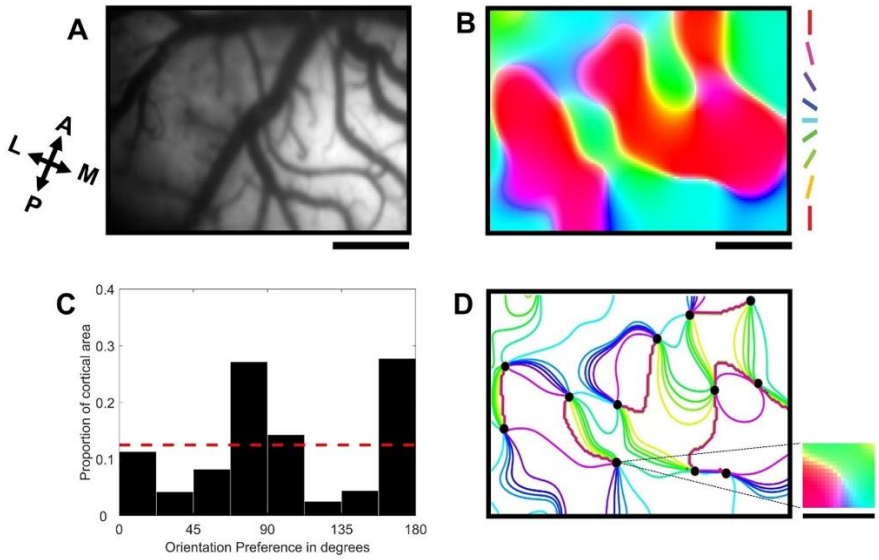

Figure 2.9 OP map obtained from Wallaby W6. **(**See the collective legend for 2.7 to 2.9 below for more detail).

Figure 2.7–2.9 OP maps obtained in the peripheral visual field of three wallabies. **(A)** The image of the cortical surface illuminated with green light. A: Anterior; P: posterior; M: medial; L: lateral. **(B)** OP map showing the preferred orientation for every region of interest. The angle is colour-coded according to the scheme in the legend. **(C)** Proportion of cortical area representing different orientations from right eye stimulation. The red dashed line at a frequency of 1/8 represents uniform distribution. **(D)** OP contours showing the organisation of all the orientation columns and black dots representing pinwheels. W4: 9 pinwheel centers located within 7.5 mm^2 cortical area. Pinwheel density = 1.20 pinwheels/mm^2. W5: 10 pinwheel centers located within 9.37 mm^2 cortical area. Pinwheel density = 1.07. W6: 12 pinwheel centers located within 9.79 mm^2 cortical area. Pinwheel density = 1.12 pinwheels/mm^2. The inset shows a zoom-in onto a single pinwheel. Square width = 1 mm. Scale bar = 1 mm.

2.3.3 Ipsilateral and contralateral eyes

We also recorded cortical responses by stimulating the frontal field of the ipsilateral eye. There was only one experiment in which we were able to record optical imaging signals that were strong enough to construct an OP map via ipsilateral stimulation. Figure 2.10A–H illustrates a comparison between single condition maps obtained from contralateral and ipsilateral eye stimulation. The red arrows on the single condition maps from the contralateral eye indicate areas with high activity. When the same arrows are superimposed onto the corresponding ipsilateral maps, we can see that the dark patches are present in approximately the same areas. Moreover, the OP maps (Figure 2.10I & J) produced from monocular stimulations of right and left eye also look similar. The correlation coefficient between the two OP maps was calculated to be $r^2 = 0.31$ ($p = 0.001$). The similarity between the maps of ipsilateral and contralateral eyes is consistent with previous physiological findings that suggest an overlap in the visual cortex of the inputs from the contralateral and ipsilateral eyes, without segregating into OD columns (Vidyasagar et al., 1992).

Figure 2.10K shows the OD map calculated by summing all eight iso-orientation maps obtained from the contralateral eye and subtracting the result by the sum of the eight single condition maps obtained from the ipsilateral eye. The black represents contralateral eye preference, and white represents the ipsilateral eye preference in the OD map. The greyscale bar represents the magnitude of the responses. Although some black and white patches are present on the map, there are more grey areas stimulated by both contra- and ipsilateral eyes. An ocular dominance index (ODI) was calculated as described in the Methods. ODI ranges between -1 and 1, with negative and positive values representing ipsilateral and contralateral dominance, respectively. The median of the OD scores across all responsive pixels was 0.478, which indicated a strong bias towards contralateral eye inputs.

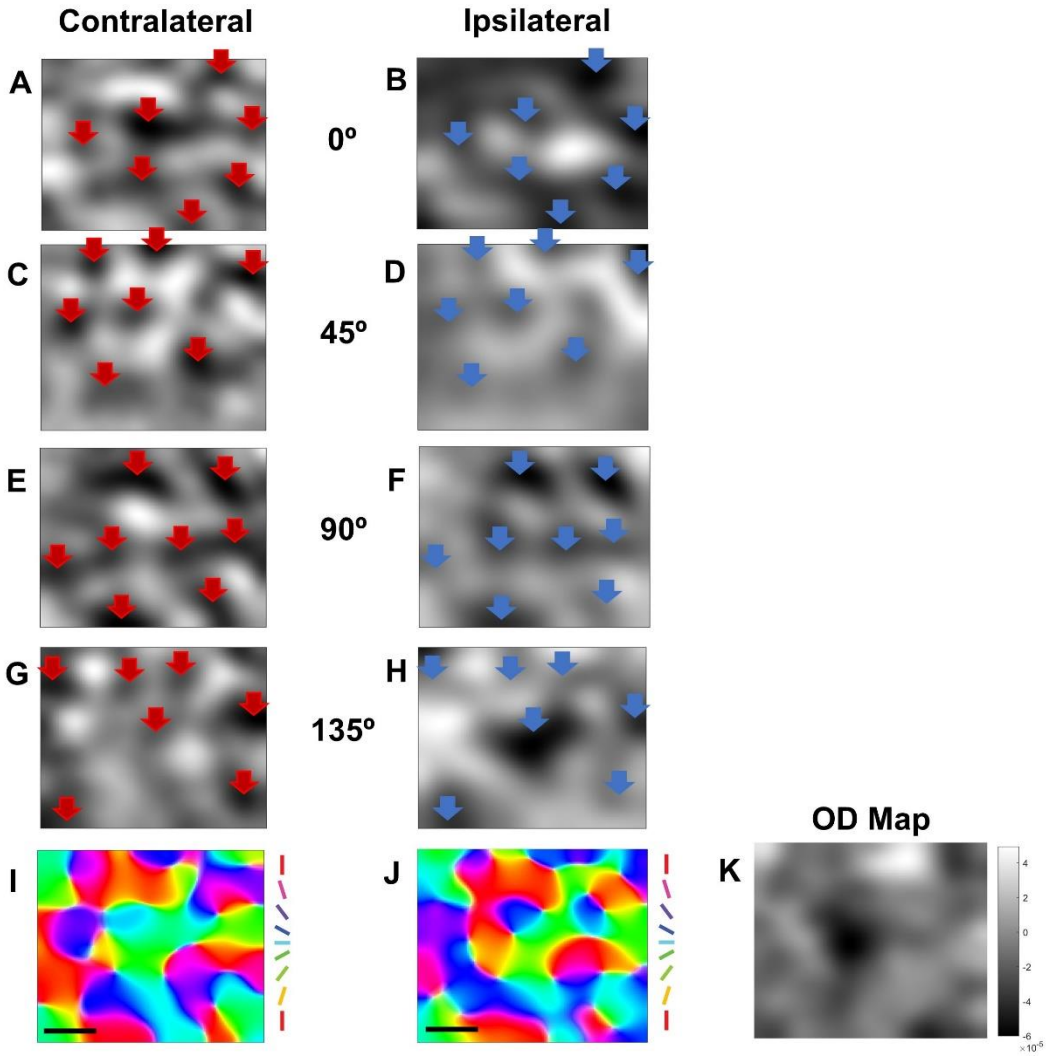

Figure 2.10 Monocular stimulation of the contralateral and ipsilateral eye produces similar activity patterns in wallaby V1. **(A–H)** Single condition maps obtained after monocular stimulation with gratings of four different orientations (dark areas represent high activity). The red arrows indicate dark patches with high intensity, and for comparison, the same arrows are overlaid on the ipsilateral single condition maps (blue arrows). **(I–J)** OP maps obtained from summing cortical responses from eight different orientations. The angle is colour-coded according to the scheme in the legend. For tammar wallabies, the contralateral and ipsilateral inputs overlap in the visual cortex without segregating into columns. Hence the OP maps from the two different inputs look similar. The correlation coefficient between contralateral and ipsilateral OP maps is r^2 = 0.31. Scale Bar = 1 mm. **(K)** OD map obtained by subtracting the sum of all the cortical responses of 8 orientations from contralateral stimulation with the sum of cortical responses from ipsilateral stimulation. Black represents the contralateral eye and white represents the ipsilateral eye. The greyscale bar represents the response magnitude.

2.3.4 Direction Preference maps

DP maps were constructed by vectorially summing the cortical images acquired from gratings moving in 16 directions. Figure 2.11A shows the DP map (in arrows) superimposed on a colour-coded OP map. The DP map appears to have numerous regions within which DP shifts slowly and continuously, similar to how orientation columns are organised around pinwheels. However, these regions are separated by fractures across in which DP changes abruptly by 180°.

Figure 2.11B shows the organisation of DP around an orientation pinwheel. DP shifts continuously with orientation around a pinwheel, except at the fracture (indicated by the white dashed line), where contiguous cortical regions show opposite DPs. The single orientation columns are subdivided into numerous patches preferring opposite DP. Moreover, these directions are orthogonal to the corresponding orientation preference, which is consistent with the previous finding in cat primary visual cortex (Weliky et al., 1996). Figure 2.11C & D show regions preferring vertical gratings, which are subdivided into two patches with opposite directions of motion (left/right). Figure 2.11E shows a region preferring gratings oriented at 157.5°, which is subdivided into two patches preferring diagonally opposite directions of motion.

Similarly, the DP map obtained from the peripheral visual field of V1 (Figure 2.12) shows a subdivision of direction patches in numerous orientation domains. Figure 2.12A shows DP shifting continuously with orientation around a pinwheel and meeting at the fracture where opposite directions stimulate adjoining cortical regions. Figure 2.12B shows a region stimulated by vertical gratings (red) subdivided into two directions of motion (left and right). Figure 2.12C shows a region preferring horizontal gratings (green/cyan), subdivided into patches preferring two directions of motion (up and down).

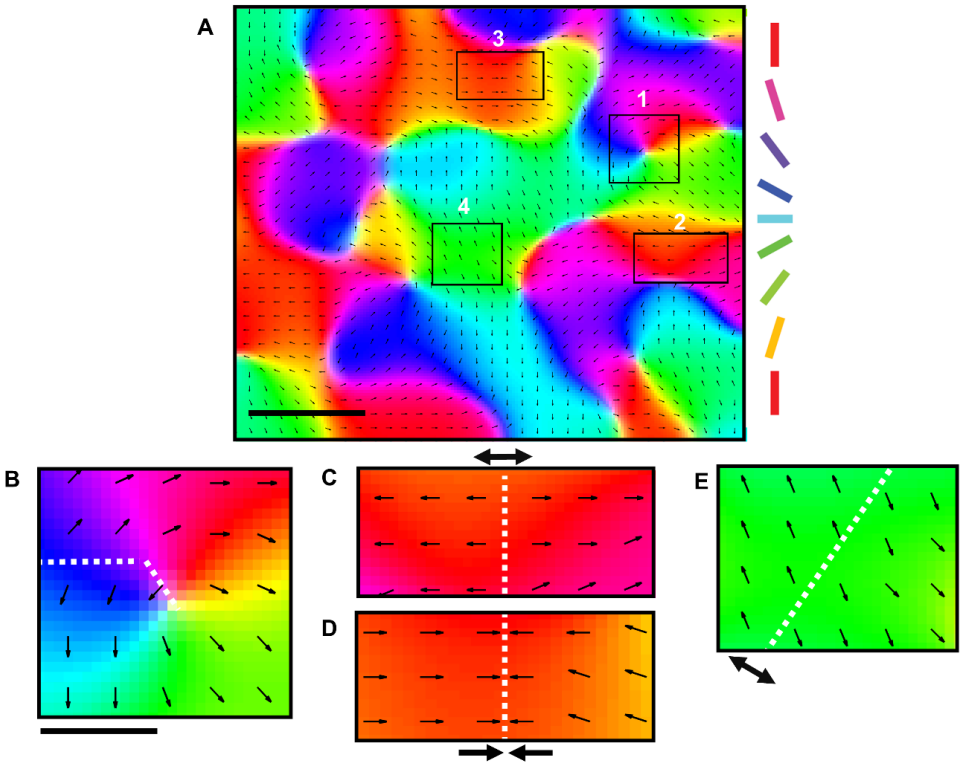

Figure 2.11 Relationship between DP map and OP map obtained from the central visual field representation of wallaby V1. **(A)** DP map represented as arrows are superimposed on an OP map. The angle is colour-coded according to the scheme in the legend. Scale bar =1mm. **(B)** Area 1 shows the organisation of DP around an orientation pinwheel. DP shifts smoothly with orientation except at the fracture (white dashed line) where contiguous cortical regions have opposite DPs. Scale bar = 500 µm. **(C, D)** Areas 2,3 are stimulated by vertical gratings (red) and subdivided into two DP (left and right). **(E)** Area 4 prefers an orientation of 157.5° (green) and is subdivided into patches preferring diagonally opposite DP.

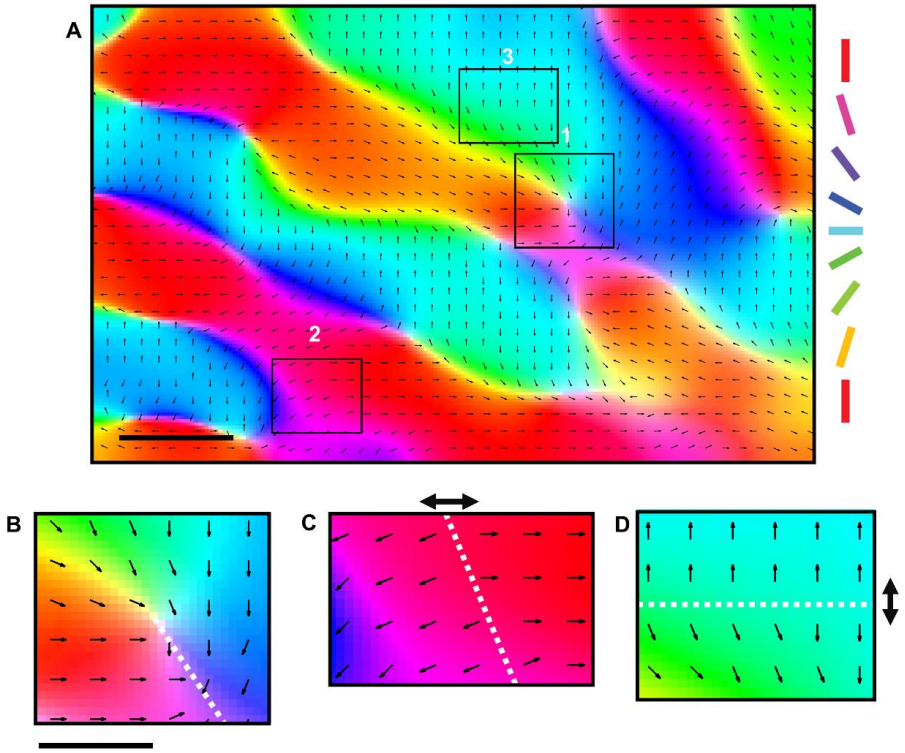

Figure 2.12 Relationship between DP map and OP map obtained from the peripheral visual field representation of wallaby V1. **(A)** The DP map represented as arrows are superimposed on an OP map. The angle is colour-coded according to the scheme in the legend. **(B)** Area 1 shows the organisation of DP around an orientation pinwheel. DP shifts smoothly with orientation around the pinwheel and meets at the fracture (white dashed line) where contiguous cortical regions have opposite DPs. Scale bar = 500 µm. **(C)** Area 2 is stimulated by horizontal gratings (red) and subdivided into two patches preferring opposite DP (left and right). **(D)** Area 3 prefers vertical gratings (green/cyan) and is subdivided into two patches preferring opposite DP (up and down).

2.3.5 A comparison between optical imaging and extracellular spiking

We compared measures of orientation preferences from single-unit recordings with the corresponding measures from the OP maps. Note, only the single-unit recordings from the superficial layers of the cortex were used in the analysis (i.e. channels expanding from the surface to 1mm deep) (see section 3.2.1 for more details on electrophysiology experiments). Figure 2.13A shows the surface of the cortex imaged from one of the brains. The symbols represent where the electrodes were placed to record the spikes. For each of the electrode tracks, 10x10 pixel ROIs were placed around the centre, and the average preferred angle of every pixel within the ROIs was calculated. The mean orientation preference calculated from ROI 1 =

104°, ROI 2 = 80°, ROI 3 = 22°. The orientation preference of each single unit was quantified by measuring its responses to sine wave gratings drifting in each of 16 directions (0°–360°). Responses to opposite directions were summed and the orientation with maximal response was determined. Figure 2.13B shows the orientation preference measured from the single-unit recordings plotted against the orientation preference measured from the OP maps. The plot includes single-unit recordings in the superficial layers from all six wallaby experiments (n = 52). We can see a strong correlation between the two methods (r^2 = 0.771, p = 0.001) with a median absolute difference of 16.94°. The high degree of correlation between the two measures gives us confidence in the quality of the data and the reproducibility of OP maps obtained from optical imaging data.

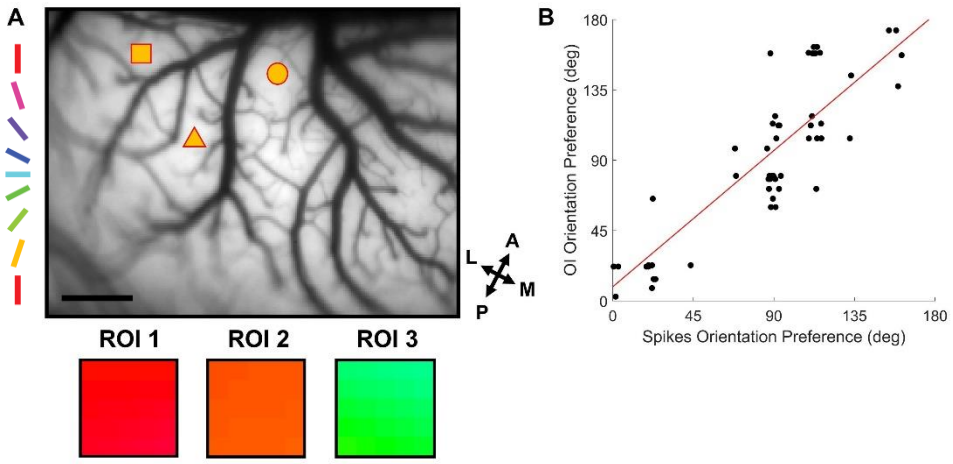

Figure 2.13 Comparing measures of orientation preferences between optical and single-unit recordings. **(A)** Cortical surface imaged under green light for one of the imaged cortices. The symbols indicate the locations of electrode penetrations. 10 x 10 pixel ROIs were placed around each of the electrode tracks. The three coloured boxes represent the average vector of the pixels within the ROIs. ROI 1 = 104°, ROI 2 = 80°, ROI 3 = 22°. **(B)** Plot of preferred orientation measured from the single-unit recordings and the corresponding ROI in the OP maps. The red line represents a strong linear correlation between the two methods (r^2 = 0.771, p = 0.001) with a median absolute difference of 16.94°.

2.4 Discussion

2.4.1 Optical imaging of wallaby visual cortex

We used intrinsic optical imaging methods to obtain orientation preference maps (OP), direction preference maps (DP) and ocular dominance maps (OD) for the first time in a marsupial visual cortex. Previous studies have mainly used red light (> 600 nm) to image from the cortex, but in this study, we used green light (520 nm), as it has a more robust signal-to-noise ratio (Sirotin & Das, 2009; Sirotin et al., 2009; Cloherty et al., 2016). In some of our wallaby experiments, where there were notably strong brain pulsations, the conventional methods for map generation left strong blood vessel artefacts in the maps derived from green light data. This was most likely because changes in cortical reflectance of green light indicate changes in blood volumes (Sirotin & Das, 2009; Sirotin et al., 2009). This problem was resolved by using the extended spatial decorrelation (ESD) method, as described in the Methods. This technique allowed for robust separation of the stimulus-specific intrinsic signals from the biological noise and artefacts in the green light data (Figure 2.3). We found that the measures of orientation preference from single unit recordings corresponded strongly with the OP maps (Figure 2.13, $r^2 = 0.771$, $p = 0.001$), which provides a high level of confidence in the quality of the data and the reproducibility of OP maps obtained from optical imaging data.

2.4.2 Orientation Preference maps in wallaby visual cortex

In this study, we wanted to know whether the development of OP maps is influenced by (1) phylogeny and (2) the topography of the retina. From a phylogenetic standpoint, we proposed that if marsupial mammals have a pinwheel OP map, it is most likely that OP maps existed from the beginning for all mammals, but, for some species, it has been altered through convergent evolution. So far, most mammalian groups have been shown to have pinwheel structures, while the Clade Glires (rodents and rabbits) are the only species studied that have displayed salt-and-pepper maps. In our experiment, we found strong evidence of OP maps (Figure 2.4–Figure **2.8**) in the highly visual marsupial, the tammar wallaby, which suggests

that the species in the Clade Glires are the unusual case in the mammalian visual cortex organisation. Convergent evolution may also explain the formation of pinwheel structures in marsupials and other Eutherian species. When looking at marsupials and other Eutherian species, we see that they have similar body forms, which might reflect similar ecological niches. For example, the tammar wallaby comes from the same highly developed phylogenetic grouping as the tree-kangaroos and cuscuses (Order, Diprotodontia). The latter have body structures and tree climbing behaviours not unlike prosimian primates (e.g. lemurs). Given the extensive evidence for convergent evolution of body forms, the capacity for convergent evolution of brain structure, perhaps driven by retinal organisation (e.g. CP ratios), is possible.

That being said, it is to be noted that there are variations in OP maps across species. Unlike the lattice-like organisation observed in cats and primates (Bonhoeffer & Grinvald, 1991; Obermayer & Blasdel, 1993; Hübener et al., 1997), the pinwheels were sparsely organised in the wallaby V1. Figure 2.1.4 shows the distribution of pinwheel points for central and peripheral OP maps. The median distance to the nearest-neihbouring pinwheel points for central OP maps (median ±std: 526.36±171.05 μm) is significantly lower (t-test: $p < 0.01$) than in the peripheral OP maps (median ±std: 677.55±177.05 μm). It is possible that the reduced number of retino-cortical connections in the periphery decrease the likelihood of orientation-selective cells clustering. We also found the size of orientation domains to be larger than that of cats and primates, and that the pinwheel density was also lower. This will be discussed in the second hypothesis.

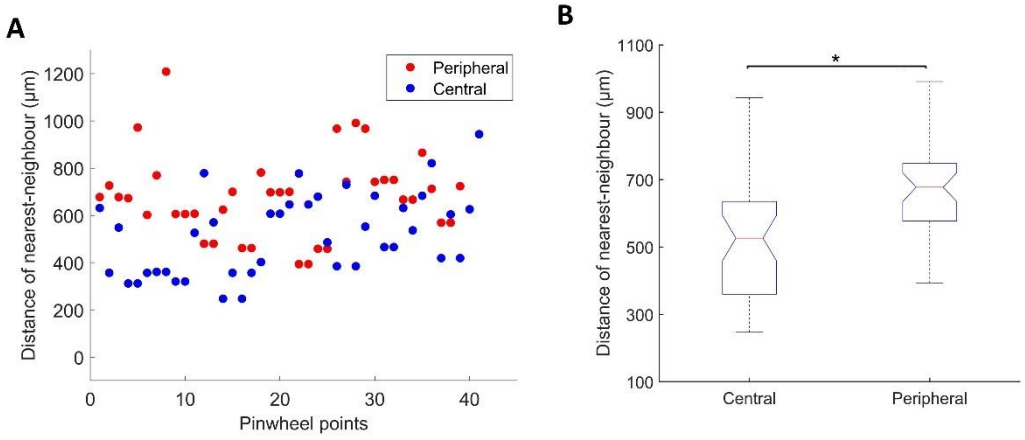

Figure 2.14 Comparison of the distribution of pinwheel points between central and peripheral orientation preference (OP) maps. **(A)** Plot showing the distance to the

nearest-neighbouring (um) pinwheel points for central OP map (in red) and peripheral OP map (in blue). **(B)** Boxplots comparing the median distance to the nearest-neighbouring pinwheel points for central (median ±std: 526.36±171.05 μm) and peripheral (median ±std: 677.55±177.05 μm) OP maps, with outliers removed for the plot. * represent p <0.001 (t-test).

The second hypothesis we proposed, based on the observations discussed in the literature review, was that the existence of pinwheel maps versus salt-and-pepper maps might be determined by the density of cells providing input to the cortex. It is believed that cortical development is driven by the Hebbian principle, "what fires together, wires together" (Goodhill, 2007; Hebb, 1949). Within this framework, cells with the same orientation tuning are more likely to cluster with local excitation and long-range inhibition within intracortical connections (Erwin et al., 1995; Olshausen & Field, 1996; Miller et al., 1999; Ferster & Miller, 2000). As discussed in the literature review for cells to cluster within different cortical domains, there needs to be sufficient spacing between thalamic axon patches (Mazade & Alonso, 2017). Species with pinwheel maps (e.g. cats, monkeys, and ferrets) have low densities of LGN axons in V1 (Ibbotson & Jung, 2020). In contrast, species with salt-and-pepper maps (i.e. rodents and rabbits) have high LGN densities in V1. Interestingly, species with low LGN-axon densities in V1 tend to have more inputs from LGN cells than species with high LGN-axon densities. This is because, as the number of LGN cell inputs increases, V1 overexpands in a non-linear manner (Stevens, 2001).

In cats and monkeys, the high number of LGN cell inputs is related to greater devotion of RGCs to central inputs (Kremkow & Alonso, 2018). We used the centre-to-periphery ratio (CP ratio) described in the literature review (Chapter 1) to predict whether or not a species has pinwheel maps. As seen in Figure 2.14A, we found that for a species with CP ratio < 4 (e.g. rat, grey squirrel, mouse, and rabbit), the pinwheel map was absent. On the other hand, for species with a CP ratio > 7 (e.g. cat, sheep, ferret and primates), the pinwheel map was present. Moreover, we proposed that the CP ratio may be used to predict the density of pinwheels (per mm^2) for a species with a pinwheel map. The wallaby was found to have a CP ratio of 20, which indicates that they have a strong centralised retinal input to the cortex. The fact that wallabies have pinwheel maps suggests that there is a consistent correlation between the CP ratio and the existence of pinwheel maps. In this study,

we have also demonstrated the apparent positive linear correlation between CP ratios and pinwheel density, now also including data from tammar wallabies (Figure 2.14B).

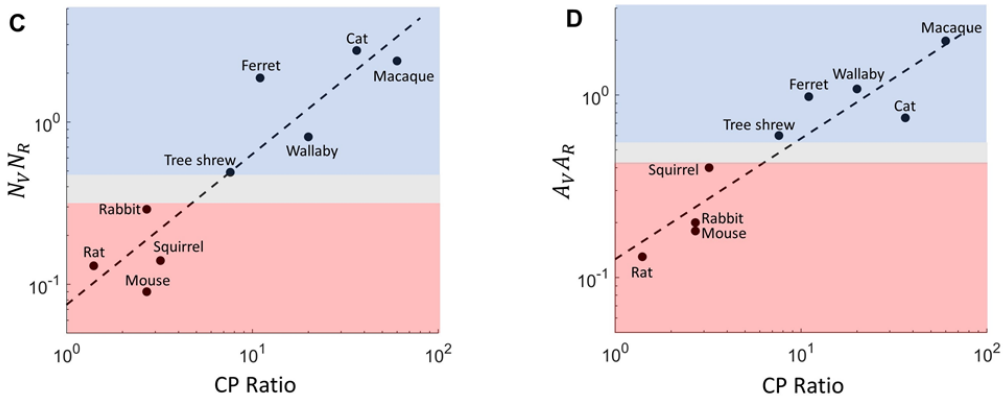

Figure 2.14 Relationship between organisation of RGCs and OP map structure. **(A)** Presence of pinwheels plotted against the CP ratios. Red, no pinwheels; blue, pinwheels. Circles show results from intrinsic optical imaging. Stars show results inferred only from single-cell recording. The dotted vertical arrow shows the possible threshold between species with pinwheels and those without. TS, tree shrew; NHP, non-human primates (including bushbaby, owl monkey, macaque). **(B)** For cat, primates, and wallaby (wallaby-c: central visual field; wallaby-p: peripheral visual field) the pinwheel density (per mm^2) is plotted as a function of CP ratio. The linear regression is shown as a blue dashed line ($r^2 = 0.841$). Source: Ibbotson and Jung (2020). **(C)** For each species, CP ratios are plotted against the ratios between the number of V1 neurons and RGCs ($N_{V/}N_R$) to predict V1 organisation. The dotted line represents a strong correlation between the two variables ($r^2 = 0.71$, $p = 0.001$) **(D)** CP ratios are plotted against the ratios between the size of V1s and of retinas ($A_{V/}A_R$) to predict V1 organisation. The dotted line represents a strong correlation between the two variables ($r^2 = 0.79$, $p = 0.001$).

As mentioned above, when RGCs are sampled by a large number of V1 neurons, the neighboring V1 neurons are likely to have highly overlapping receptive fields as a result of high sampling density from the retina to V1, which is correlated with clustering of neurons with similar orientation tuning. To make this assessment, Jang et al (2020) calculated the ratios of the number (N) of V1 neurons to RGCs (N_V/N_R) and of the areas (A) of V1 to retina (A_V/A_R). We found a strong linear correlation between CP ratios and $N_{V/}N_R$ (Fig.2.14C, $r^2 = 0.71$, $p = 0.001$) and CP ratios and $A_{V/}A_R$ (Fig.2.15D, $r^2 = 0.79$, $p = 0.001$). Species with high CP ratios (including Tammars) have high retino-cortical mapping ratios and pinwheel maps. In contrast, species with salt-and-pepper maps have low CP ratios and low retino-cortical mapping ratios. Our data support the theory that retinal density gradients are an

important driving force behind cortical feature map formation in cortex. By studying a very distantly related marsupial mammal, we have also further isolated the species in the Clade Glires as the odd ones out in terms of their cortical design.

Overrepresentation of cardinal vs oblique angles

On average, 25–30% more of the cortical area responded preferentially to cardinal (i.e. horizontal and vertical) than to oblique angles. Our findings are consistent with previous studies that have reported more neurons preferring cardinal angles in the primary visual cortex of cats, ferrets, monkeys (cat: Pettigrew et al., 1968; Payne & Berman, 1983; Vidyasagar et al., 1992; ferret: Coppola & White, 2004; Chapman & Bonhoeffer, 1998; Grabska-Barwińska et al., 2009; monkeys: De Valois et al., 1982; Smith et al., 1990). This is largely consistent with the classical oblique effect in humans, where we see greater behavioural sensitivity to gratings with horizontal or vertical orientations than to other, oblique orientations (Rovamo et al., 1982). In cats and primates, a bias towards horizontal and vertical orientations is also evident in the distribution of RGCs and their primary dendrites, which are more densely packed along the horizontal and vertical meridians (Hughes, 1977). Coppola and White (2004) believe that the overrepresentation of cardinal angles in the visual cortex may be the consequence of a greater devotion of the visual system's circuitry to the processing of contour information in the cardinal angles.

It is possible that a strong bias towards horizontal and vertical angles in wallabies is a consequence of their biological systems evolving in an environment with dominant horizontal (e.g. horizon) and vertical (e.g. tree trunks) features. Experimental studies have previously reported that rearing animals with visual input biased towards vertical and horizontal orientations altered the OP map (Sengpiel et al., 1999; Tanaka et al., 2006; Giacomantonio et al., 2010; Cloherty et al., 2016). The columns representing the exposed orientation in the environment become enlarged, while columns representing other orientations reduce in size. These rearing experiments show that the genetic code allows environment-driven flexibility in cortical design.

Central vs peripheral representation

In this study, we found differences in the organisation of orientation preferences in the central and peripheral visual representations of wallaby visual cortex. As mentioned above, we observed iso-orientation domains arranged radially around pinwheels in the orientation maps obtained from the central visual field (Figure 2.4Figure **2.5**). In contrast, in the peripheral representation of V1, we found the coexistence of radial and linear organisation of iso-orientation domains (Figure 2.6Figure **2.8**). Here, the preferred orientation was organised linearly, parallel to the medial-lateral axis of the cortical surface, measuring 0.7–1mm in length. Further, pinwheel centres were found at the edges of these linear bands. In the cat area 17/18 border, the long linear sequences of orientation domains also coexist with the radial organisation of orientation (Shmuel & Grinvald, 2000). However, they have suggested that the differences between radial and linear arrangements may not have a functional significance during the processing of visual information. It is possible that the visual inputs to the periphery for lateral eyed animals (e.g. wallabies and rabbits) rush past quickly in front-to-back motion that only the stimuli that are aligned with the rectus muscles running horizontally and vertically are processed. To maintain reflexive optokinetic nystagmus (OKN), there may be a strong drive from vertical and horizontal motion detectors (Wallman & Velez, 1985).

2.4.3 Direction Preference maps in wallaby visual cortex

We also demonstrated for the first-time that neurons cluster according to the direction of motion in wallaby V1 (Figure 2.11Figure **2.12**). Our findings reveal that DP shifts continuously with orientation across the map, except at the fracture point where the opposite DPs divide into different regions. Similar to DP maps in the primary visual cortex of cats and ferrets (Weliky et al., 1996; Shmuel & Grinvald, 2000; Ohki et al., 2005), the preferred directions were orthogonal to the preferred orientations. Orientation patches are divided into areas preferring opposite directions because neurons are tuned to both the orientation and the direction orthogonal to the orientation. The similarity in the types of organisation observed in different species implies that there may be underlying universal principles for the existence of OP and DP maps.

It is also interesting to relate our findings to the organisation of orientation and direction in a different visual brain area, in this case also from a different species. In macaque area MT, the neurons also cluster according to their direction of motion (Maunsell & van Essen, 1983; Albright, 1984). Area MT is sometimes called Area V5, donating that it is higher in the visual hierarchy than V1 (Dubner & Zeki, 1971; Zeki et al., 1991). Area MT is specialised for detecting image motion (Zeki, 1974). The functional organisation of direction-selective neurons in tammar wallaby agree remarkably with those of macaque area MT in that the direction preference changed smoothly across the map, except at the fracture. Moreover, the relationship between the mapping for the orientation domain and the direction domain is also similar in that orientation patches are divided into areas preferring opposite directions.

2.4.4 Ocular Dominance maps in wallaby visual cortex

The OD maps have been examined for the first time in a tammar wallaby visual cortex using intrinsic optical imaging (Figure 2.10). We found that monocular stimulation of contralateral and ipsilateral eyes produced similar activity patterns in the wallaby visual cortex. Our result is consistent with a physiological study by Vidyasager et al. (1992), which suggested that contralateral and ipsilateral inputs do not segregate into different columns in the wallaby visual cortex.

The absence of OD columns in the wallaby cortex is similar to that of rodents (grey squirrels: Van Hooser & Nelson, 2006; mice: Frenkel & Bear, 2004) and new world monkeys (capuchin monkeys: Hess & Edwards, 1987; owl monkeys: Rowe et al., 1978; squirrel monkeys: Adams & Horton, 2003). On the other hand, Eutherian mammals such as old-world monkeys (Florence & Kaas, 1992) and cats (LeVay & Gilbert, 1976) are known to have clear segregations of geniculocortical inputs into OD columns. Since a marsupial, i.e. the tammar wallaby, and a large number of Eutherian mammals do not have OD columns, it may be possible that the lack of columnar segregation is a primitive mammalian pattern and, for some species, OD columns may have developed as a result of convergent evolution. However, the fact that there is not even consistency within primates suggests that ODCs have very complex origins.

2.5 Conclusion

The conclusion is that the OP and DP mapping observed in the primary visual cortex (V1) of marsupial wallabies is similar to that found in the V1s of most mammals, and even in other visual brain areas in other mammals. Species in the Clade Glires (i.e. rodents and rabbits) do not have this structure, suggesting that they are the unusual case in mammalian visual brain organisation. As discussed above, the differences in the density of cells providing input to the cortex in the Clade Glires and other mammals may explain the existence of salt-and-pepper maps versus pinwheel maps. It would be interesting to study orientation map structures in rodent-like marsupials. Do they have salt-and-pepper maps? In contrast, it is harder to draw the same conclusion regarding convergent evolution for OD columns given the high level of variance across different species.

Abbreviation	**Meaning**
DP	Direction Preference
OD	Ocular Dominance
NVRI	National Vision Research Institute
O_2	Oxygen
N_2O	Nitrous oxide
CO_2	Carbon Dioxide
LCD	Liquid-crystal display
ESD	Extended spatial decorrelation
ROI	Region of Interest
MT	Medial temporal

Chapter 3

3.1 Introduction

The visual pathway to the cortex involves light passing through the retinal ganglion cells (RGCs), to the lateral geniculate nucleus (LGN), and to the primary visual cortex (V1). The shape of the cortical RF is determined by inputs from a bundle of thalamic afferents. Past studies have revealed that orientation selectivity (OS) and the clustering of cells in cortical domains are seeded by ON and OFF thalamic afferents (Soodak et al., 1987; Goodhill & Löwel, 1995; Ringach, 2004; Paik & Ringach, 2011; Kremkow et al., 2016). The classical hierarchical model suggests that spatially offset LGN cells with circular symmetric RFs converge onto a single V1 neuron to generate elongated RFs (Hubel & Wiesel, 1962). Cats and monkeys have low or absent OS in the LGN. Consistent with the hierarchical theory, in these species, OS appears as an emergent property in V1 (Hubel & Wiesel, 1968; Ts'o et al., 1990; Bosking et al., 1997). In contrast, rabbits and rodents have been found to have OS emerging early in the visual pathway, in the RGCs, or in LGN (Stewart et al., 1971; Murphy & Berman, 1979; Ohki et al., 2005). It has been revealed that in species where OS emerges in higher areas of the visual system, they exhibit clear OP maps in V1 (i.e. cats and monkeys), whereas species in which OS emerges earlier reveal no such organisation in V1 (i.e. rabbits and rodents). It is possible that the formation of OP maps relates directly to the existence of subcortical OS. In the case of the tammar wallaby, we know that strong OS is present in V1 (Ibbotson & Mark, 2003), but it is yet unknown if OS emerges in the LGN.

Classically, spots or bars of light were used to characterise V1 spatial RFs (Hubel & Wiesel, 1962). These studies revealed clear ON and OFF subregions of simple cell RFs, and the locations and overall sizes of complex RFs. Using Fourier

analysis of responses to moving gratings to calculate modulation indices, Ibbotson et al. (2005) distinguished simple and complex cells in wallaby visual cortex, similar to those found in the rat, cat, and monkey. However, it was not possible to characterise the spatial structures of ON and OFF regions of complex cells because of their nonlinear spatial summation mechanisms. Previous work on the wallaby V1 was based on findings in responses to drifting gratings and no studies have directly measured the spatial structures of the RFs in V1 or LGN cells. Later studies have used reverse correlation techniques to characterise neuronal RFs in V1 (e.g. Simoncelli & Llampaninski, 2004; Touryan et al., 2005; Nishimoto et al., 2006; Liu et al., 2016) When a neuron is presented with a set of arbitrary and prolonged stimuli (i.e. white-Gaussian noise or natural images), reverse correlation determines all the features of the stimulus that the neuron responds to or becomes inhibited by, which is used to estimate the spatial structure of the neuron's RF.

Recent characterisation techniques have employed parametric models to obtain a more physiological representation of the stimulus response relationship of simple and complex cells. The nonlinear input model (NIM) is one of the most robust techniques that employs a biologically plausible model for characterising RFs in cortical cells. For more detail on the NIM refer to the following papers: (McFarland et al., 2013; Almasi et al., 2020).

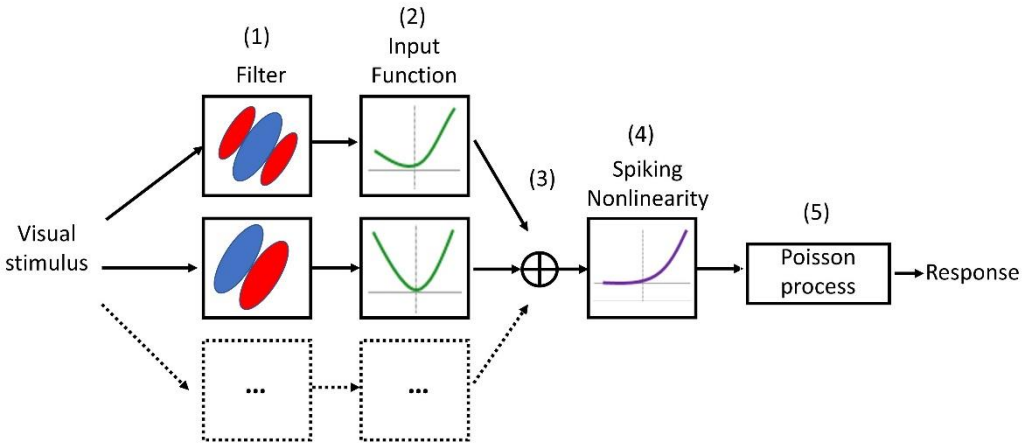

Figure **3.1** illustrates a schematic diagram of the NIM. In the first step of the NIM framework, the visual stimulus is processed in parallel streams by several spatial filters. The output is the feature contrast, which represents the similarity

between the visual stimulus and the spatial filters. The signals are then passed through separate input functions. In the case of NIM, input functions are completely general, rather than fixed. For example, they can be either linear or nonlinear. The signal is then fed through a spiking function. The purpose of the spiking function is to include the nonlinear spiking characteristics of the cell, i.e. spike threshold, spontaneous activity, and response saturation. This spiking function turns the signal into a firing rate. Finally, the spikes are generated randomly by a Poisson process that produces the neuronal response. This NIM method will be explained in detail in the Methods.

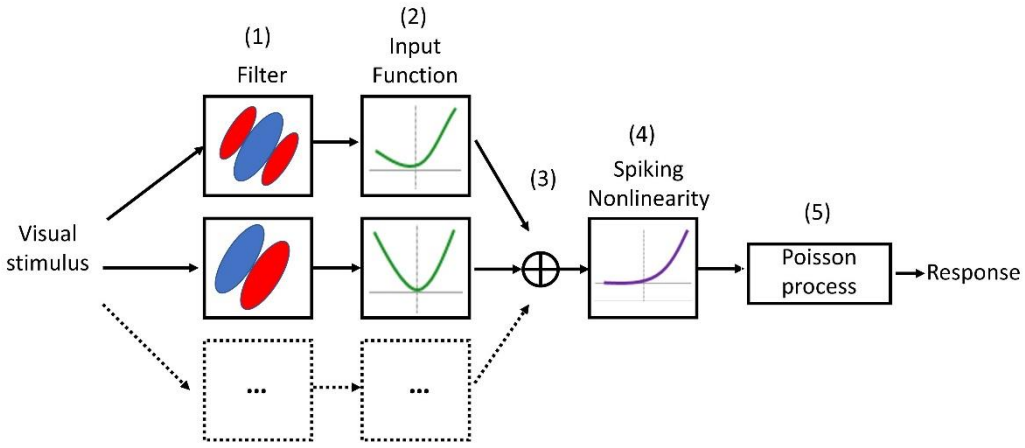

Figure 3.1 Schematic diagram of the NIM. In parallel streams: (1) visual stimulus is processed by several spatial filters, (2) the signal is then fed into the input nonlinearity, (3) the parallel streams combine together to produce a generator signal, (4) the generator signal is processed by the spiking nonlinearity, and (5) randomised by a Poisson process to produce a response for the neuron.

In this chapter, we attempt to characterise the spatial RFs of the cells in V1 and LGN of anaesthetised wallabies using the non-parametric NIM method for the first time. Using recordings from a population of V1 cells and LGN cells in response to WGN, we will examine the diverse range of image features that the neuron responds to through their RF filters and quantitatively measure the orientation selectivities of the cells in V1 and LGN of the wallabies. In this chapter, I aim to determine if OS occurs early on in wallabies, as in the rodents or later in V1, as in cats and primates.

I will also relate the findings to our theory on how the existence of subcortical OS may affect the type of OP map created.

3.2 Methods

3.2.1 Experimental Procedures

All surgical procedures were the same as those described in the previous chapter. We recorded from cells in the primary visual cortex of six anesthetised wallabies and cells in the lateral geniculate nucleus (LGN) of one anesthetised wallaby. For LGN recordings, the electrode was vertically inserted to a depth of 11–13 mm in the area that expanded 8–10mm posterior to bregma and 7–11 mm lateral from the midline, using the stereotaxic coordinates described by Wye-Dvorak et al. (1987).

Visual stimuli

As described in the previous chapter, visual stimuli were presented with a ViSaGe visual stimulus generator on a gamma corrected LED monitor at a viewing distance of 57 cm. WGN stimuli were used to estimate the spatial RFs of cortical cells. WGN images comprised of 90 x 90 pixels over 30° of the visual field, with its mean pixel value matched to the mean luminance of the display monitor. If the spatial RF size was small, the size of WGN images was adjusted to 60 x 60 pixels. Each noise block comprised of 12,000 WGN images, which were each presented for 1/30 second. It was followed by a blank screen of the mean luminance, displayed for the same duration of 1/30 sec. The blank screen was used to increase the overall response of the cell to the stimuli as it would minimise any temporal correlation in the responses. The standard deviation of each noise block was determined, to obtain 90% of individual pixels with non-saturated values between 0 and 1, while the remaining pixels were clipped to produce 10% saturation rate of the generated noise block.

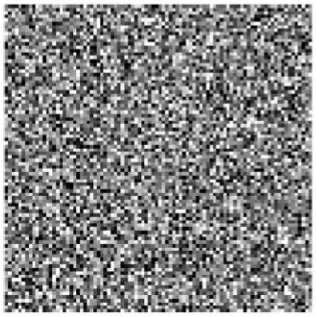

Figure 3.2. Image of 90 x 90 White Gaussian noise

In addition to the WGN stimuli, we used drifting sinusoidal gratings with a circular aperture (30° diameter) set to high contrast (Michelson contrast 100%) on a grey background at the mean luminance. We presented various combinations of spatial and temporal frequencies to determine a cell's preferred direction (i.e. 16 directions equally spaced between 0° and 360°). Each stimulus direction was presented randomly for at least 5 trials.

Data recording

Extracellular recordings were conducted using NeuroNexus 32 channel multi-electrode arrays (MEAs). We used two types of MEAs: a single shank probe (6mm length for cortical recoding/15mm length for LGN recording; 1 x 32 sites spaced at 100 µm intervals) or a four-shank probe (6 mm length; 4 x 8 sites spaced at 100 µm intervals). For each recording session, only one type of MEA was used. The arrays were vertically inserted into the cortex using a piezoelectric drive (Burleigh inchworm and 6000 controller, Burleigh instruments, Rochester, NY). Extracellular signals from 32 channels were simultaneously acquired using a CerePlex acquisition system and Central software (Blackrock Microsystems, Salt Lake City, Utah) sampled at 30 kHz.

Spike-sorting

Extracellular recordings from MEAs can have neighbouring neurons whose spikes are picked up by the same electrode site, and in other cases, the spikes from some neurons may appear on multiple electrode sites. To separate spikes from different neurons, we used an automatic spike-sorting program called KiloSort (Pachitariu et al., 2016), which is commonly used for sorting recordings from dense arrays.

First, the raw data was high-pass filtered at 300 Hz to remove low-frequency fluctuations such as the local field potential. Then, the median signal from all recording sites was subtracted at each time point to reduce the effect of artifacts found across all channels. This process is described by Ludwig et al. (2009) as common average referencing. Second, the filtered data was whitened across channels to remove spatially correlated noise, which arises from neurons located far from the probe. The whitening decorrelates the signals from each other by

having each of the signals' variance equal to 1 (i.e. identity matrix). Whitening was performed by estimating the whitened matrix with the data that had any of the putative spikes above a threshold criterion removed. The whitened matrix was then multiplied to the data matrix containing all channels. Using a three-dimensional singular value decomposition (SVD) of the spike's spatiotemporal waveform, each spike in the filtered signal was assigned a private principal component. This decomposition method denoised the waveforms and removed any irrelevant channels. Spikes were detected using a threshold criterion (6 standard deviations) to initialise the templates, and the running average waveform derived from SVD was used to obtain the predefined templates. In an iterative process, the algorithm was used to find spike times from the raw data that were similar to the predefined template waveform (template matching). After subtracting the matched spikes, we repeatedly performed template matching to find spatiotemporally overlapping spikes.

We used the geometry of the recording probe to create an adjacency map, which allowed us to detect neighbouring sites. We were then able to cluster the spikes, which appeared simultaneously across multiple neighbouring sites as one unit. The spike clusters were manually sorted for further verification using the graphical user interface *phy* (Rossant et al., 2016). Single units (SU) were identified from the presence of well-separated clusters in their feature space and from the profound refractory period in their inter-spike interval histograms, which confirms that spikes are non-overlapping.

3.2.2 Model estimation

We employed the NIM described by Almasi et al. (2020) to estimate the spatial RFs. This framework is a greatly enhanced adaptation of the original model introduced by McFarland et al. (2013) to estimate all model parameters simultaneously. The

(3.1)

model diagram in

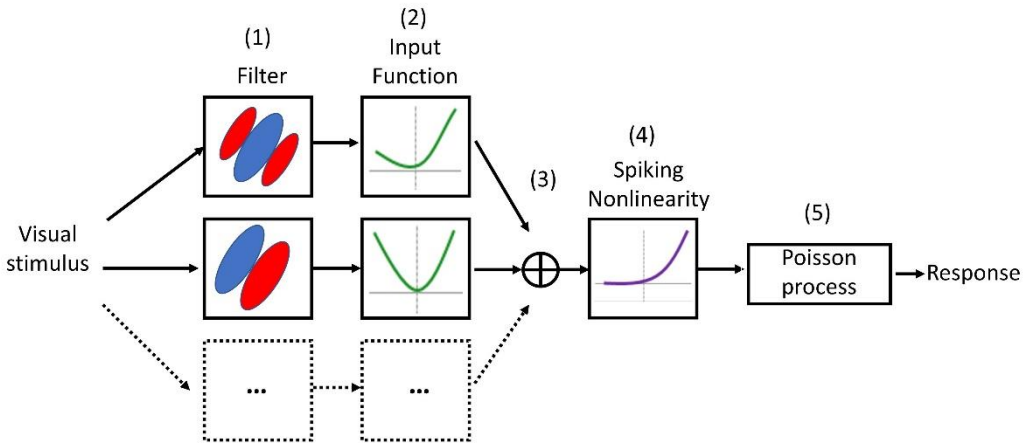

Figure **3.1** and the equation below describes the firing rate (***r***) of the cell as a function of the input visual stimulus (***s***):

$$r = F\left(\sum_{i=1}^{m} f_i\left(\langle \mathrm{k_i}, s\rangle\right)\right)$$

where $\mathrm{k_i}$ represents the parallel streams of spatial filters used to process the stimulus (***s***) and the feature contrast is defined as their inner product $c_i = \langle \mathrm{k_i}, \mathrm{s}\rangle$. The inputs from a number of parallel synaptic input streams (*m)* are summed to produce a generator signal $G = \sum_{i=1}^{m} f_i(\langle \mathrm{k_i}, \mathrm{s}\rangle)$. Each input is measured by an arbitrary input function $f_\mathrm{i}\,(\cdot)$ of the feature-contrast (c_i). The function $F(\cdot)$ is the spiking nonlinearity that converts the generator signal *G* into firing rates (*r*). The parameters in the NIM (i.e. filters $\mathrm{k_i}$, input nonlinearity f_i, and spiking nonlinearity $F(\cdot)$) were estimated using the maximum log-likelihood method. The equation below describes the log-likelihood *(LL)* of the NIM model parameters in response to a visual stimulus:

$$LL\left(\mathrm{k}_i, f_i, F \middle| \mathrm{R_{obs}}, \mathrm{s}\right) = \sum_{t=1}^{N}\left[\mathrm{R_{obs}}^{(t)} \log(r) - r\right] \qquad (3.2)$$

where N represents mutually independent stimuli with responses $\mathrm{R_{obs}} = \{r^{(1)}, \ldots, r^{(N)}\}$, i.e. spike counts. The model assumes that the responses $\mathrm{R_{obs}} = \{r^{(1)}, \ldots, r^{(N)}\}$ (integer spike counts) that are mutually independent instances of the stimuli $S = \{s, \ldots, s^{(N)}\}$ adhere to a homogenous Poisson distribution function:

$$p(\mathrm{R_{obs}}|\mathrm{S}) = \frac{r^{\mathrm{R_{obs}}} \exp(-r)}{\mathrm{R_{obs}}!} \tag{3.3}$$

where r denotes the firing rate described in equation 3.2. The spike counts for each WGN stimulus were determined by pooling all the spikes observed after the stimulus presentation within a 1/30 second window shifted by the optimum latency. For each cell, the latency was manually optimised to maximise the mean response to WGN by finding the time when neurons start to spike after a stimulus presentation. In most cases, 30–40 msec was found to be the optimum latency.

Model representation:

The spatial RF filters were represented as a 2D Fourier basis:

$$\mathrm{k}_i(x, y) = \sum_{nm=1}^{A} \xi_{iaq} B_{aq}(x, y), \tag{3.4}$$

$$B_{nm}(x, y) = z \sin(2\pi \psi_0(nx + my) + \varphi_{nm})$$

where *(x,y)* represents the horizontal and vertical pixel locations, a and q denotes integers from the set $\{-A, -A+1, \ldots, A-1, A\}$, ξ_{iaq} denotes the filter coefficients, and B_{aq} denotes a two-dimensional Fourier basis, which involves the base spatial frequency (ψ_0), a normalisation factor (z), and a phase (φ_{aq}) that is chosen to be either sine phase (φ_{aq} = 0 for $q > 0$, or $q = 0$ & $a > 0$) or cosine phase ($\varphi_{aq} = \pi/2$ for $q < 0$, or $q = 0$ & $a \leq 0$).

We chose $A = 5$ to give total basis functions of 11 x 11 = 121. The arbitrary spatial filters were represented with spatial frequencies of up to $A\psi_0$, calibrated to match the upper cut-off spatial frequency of the cell, and they covered 2.3 octaves to the lowest sampled spatial frequency. A square spatial region of interest was chosen to include each cell's RF filters comprising of a single cycle of the lowest

sampled frequency. The optimum base spatial frequency (ψ_0) was proportional to the size of each cell's RFs. We manually assigned a square spatial region of interest from the spatial RFs of the spike-triggered averaging. For consistency across different cells, we ensured that the RFs were centred in the ROI and that the spatial RF covered approximately a quarter of the ROI's area.

Input nonlinearity function $\boldsymbol{f_i}$ representation:

The input function for each filter was estimated using piecewise linear functions of the feature-contrast with a set of tent basis functions, as shown in the equations below:

$$f_i(c_i) = \sum_{l=0}^{L} \gamma_{il} \Lambda_l(c_i)$$

$$\Lambda(c) = \begin{cases} \dfrac{c - \bar{c}_{l-1}}{\bar{c}_l - \bar{c}_{l-1}} & \text{if } c \in [\bar{c}_{l-1}, \bar{c}_l] \\ \dfrac{\bar{c}_{l-1} - c}{\bar{c}_{l+1} - \bar{c}_l} & \text{if } c \in [\bar{c}_l, \bar{c}_{l+1}] \\ 0 & \text{otherwise} \end{cases} \tag{3.5}$$

where c_i represents the feature contrast and γ_{il} represents the coefficients. L = 7 equally spaced intervals $[\bar{c}_l, \bar{c}_{l+1}]$ were chosen to provide the 2.5%–95.5% interval in the distribution of feature contrast (c_i). Then, the input functions with L = 25 were determined by correcting all other model parameters for a smoother version.

Spiking nonlinearity function $\boldsymbol{F}(\cdot)$ representation

The spiking function that determines the output of the generator signal (G) to the mean firing rate (r) was represented as a log-exponential function:

$$F(G) = \alpha \log\left[1 + \exp\left(\frac{G - \theta}{\alpha}\right)\right] + d \tag{3.6}$$

where scale and shape are represented by α, threshold is represented by θ, and spontaneous spike rate is represented by *d.* The function is at a constant spontaneous spike rate (*d)* when the generator signal (G) is significantly below the threshold θ ($\frac{G-\theta}{\alpha} \ll 0$). Then the function transits to a linearly increasing function when the

generator signal (G) is significantly above the threshold ($\frac{G-\theta}{\alpha} \gg 0$). This transition appears over a wide range of spike rates estimated by $\alpha > 0$, for which the function is represented in a convex shape.

Estimating the optimal set of parameters

The optimum set of NIM parameters was determined by maximising the log-likelihood of the model shown in equation 3.2. The parameters subject to optimisation included filters (k_i), the input nonlinearities (f_i) and spiking function ($F(\cdot)$). Previous studies have used a sequential procedure to optimise these parameters, typically in the order of filters, input functions, spiking functions, while holding the other parameters fixed at each stage (McFarland et al., 2013). However, studies have found that sequential optimisation tends to preserve the type of input functions chosen to initialise the model and did not always reflect the optimum for all parameters (Fitzgerald et al., 2011; Almasi et al., 2020).

A high proportion of cells had multiple local optima, but all the cells were located in the same low-dimensional subspace of RF filters (1–5 dimensional). We performed a systematic brute force search over the low dimensional subspace to find the global optimum. This optimisation method was performed simultaneously across the set of all parameters in two steps. First, we performed a sequential optimisation using the following sequence: filters, input functions, spiking nonlinearity and back to filters, while holding other parameters fixed at each step. Second, the filter subspace identified in stage 1 was used to identify the parameters of the filters (ξ_{inm}), input functions (γ_{il}), and spiking function (α, θ, d) with the highest log-likelihood. For cells with multiple filters, the filters were initialised as different linear combinations of the basis filters:

$$U_j^0 = \sum_{i=1}^{K} O_{ij} U_i^b \tag{3.7}$$

where U_j^0 represents the initialised filter, and U_i^b represents the normalised filters obtained from sequential optimisation. The O_{ik} are the parameters we sampled from the upper hyper-sphere to maintain the unit norm of the initialised filters (U_j^0), provided the normalised basis filters U_i^b. By sampling only from the upper

hypersphere, we were able to avoid any repeats or degeneracy from the initialisations that are just opposite in sign. For example, models with two filters (*K = 2*) were sampled by polar coordinates: $O_{i1} = \cos\theta_i$, $O_{i2} = \sin\theta_i$ with $\theta_i \epsilon \frac{m\pi}{M} | m = 0, \ldots, M - 1$ where M represents an arbitrary number and $\theta_2 > \theta_1$ is set to avoid degeneracy. We chose $M = 5$ for our optimisation.

For higher dimensions, we used $O_{i1} = 1$ and $O_{ij} \epsilon \{-1, +1\}$ to sample in the upper hyper-sphere in the K-dimensional feature space. For models with three filters (K = 3), we used 16 different combinations of filter directions. For models with more than three filters (K > 3), the number of all initial filter sets was too large, which made these models computationally infeasible to probe. Hence, we decided to randomly choose 30 initial filter sets for models with four filters, and 40 initial filter sets for models with five filters. All initial filters were normalised, and the model parameters were fit simultaneously, once the filters were restricted to the feature subspace to avoid producing the same original input nonlinearity. Models with only one spatial filter have the input function and the spike function composed together in the one-dimension and they can be described with one function. To avoid any degeneracy for models with one spatial filter, the spike function parameters were held fixed $[(\alpha, \theta, d) = (1,0,0)]$ when optimisation was performed.

Avoiding model degeneracy

We have implemented two conditions in the code to avoid model degeneracy. First, all filters were normalised $\|k_i\| = 1$, as changes in the filters' norms could be also accounted for by the changes in the scale of the input functions. Second, the input functions were driven through the origin $f_i(0) = 0$ to avoid the degeneracy caused by shifts from the outputs of input functions that created an additive shift parameter θ of the spiking function.

Determining the number of filters and avoiding overfitting

The number of spatial filters of each unit was systematically varied, and we evaluated the statistical significance of each filter using bootstrapping, which is a method commonly used in RF model evaluation (Rust et al., 2005; Touryan et al., 2005; Almasi et al., 2020). Four-fifths of the data was used to estimate the filters and the remaining one-fifth of the data was used as a test set. The performance of the models with different numbers of filters was evaluated by calculating the model log-likelihood derived from the resampling of the test set. This bootstrapping evaluation was repeated 500 times, and we calculated the distribution for the log-likelihood of each model with different numbers of filters. The optimal combination of filters was determined by first starting with the simplest combination of filters (one filter) and adding a new filter each time it significantly improved the log-likelihood of the model (i.e. Z-score > 2). Filters were added until there was no significant improvement in the log-likelihood.

To prevent the input functions from overfitting to the data, we used a similar cross-validation process as that described above. We applied regularisation on the input functions by penalising their second order derivatives to get smooth functions. The penalisation factor was determined using a cross-validation process as has been described above. Four-fifths of the data were used to fit input functions using a combination of smoothing values and one-fifth of the data was used to assess the performance of the model by calculating the log-likelihood of the fitted models with different smoothing values. The procedure was repeated 500 times. The smoothing factor with the highest mean log-likelihood was determined for each cell.

Input nonlinearity characterisation

We characterised the input function based on symmetry around the origin in feature-contrast. The symmetry index (SI) for each curve was calculated as:

$$SI[g] = \frac{\|g_e\|^2 - \|g_o\|^2}{\|g_e\|^2 + \|g_o\|^2} \tag{3.8}$$

where g_e and g_o represents the even and odd components of the function g, respectively:

$$g_e(x) = \frac{1}{2}\big(g(x) + g(-x)\big), \qquad g_o(x) = \frac{1}{2}\big(g(x) + g(-x)\big) \tag{3.9}$$

The operator $\|\cdot\|$ represents the function norm in Hilbert space, which is defined as:

$$\|g(x)\| = \sqrt{\int g^2(x)dx} \tag{3.10}$$

The SI calculated in equation 3.8 varies from -1 (for an odd-symmetric function) and 1 (for an even-symmetric function). SI of 0 represents a threshold-linear function.

Determining OS from RF filters

For each single unit, RF filters were transformed into the 2D Fourier spectrum, where the radial and angular coordinates of the Fourier domain represent the spatial frequency and orientation, respectively. Orientation tuning polar plots were obtained by sampling the Fourier amplitude spectrum at the preferred spatial frequency, which is the radial distance of the maximum of the amplitude spectrum (indicated as black dashed line in Figure 3.7C). Preferred orientation was measured as the angle that which the line passing through the maximum amplitude meets the origin of the x-axis (green line in Figure 3.7C). We quantified the OS of every unit with an orientation bias (OB) index as follows:

$$OB = \frac{|\sum_k R_k \exp\ (i2\theta_k)|}{\sum_k R_k} \tag{3.11}$$

where R_k represents the neuronal response at orientation θ_k. We adopted this measure for the amplitude spectrum of filters, and R_k here represents the amplitude spectrum of the filter sampled at orientation θ_k.

An OB index of 0 is indicative of a cell responding equally to all orientations, while an OB index of 1 suggests that the cell is responding to only one particular orientation. Hence, OS is greater as OB indices increase. For single units with more than one filter, the OB index was calculated for all filters, and the minimum OB was used.

3.2.3 Analysis of RF properties from drifting gratings

Determining OS from drifting gratings

For each single unit, an orientation polar plot was obtained from the responses to different orientations θ_k, at the optimum spatial and temporal frequency. Equation 3.11 was used to calculate OB indices for cells stimulated by drifting sinusoidal gratings.

Calculating modulation index

For each single unit, the relative modulation (F1/F0) ratio in response to drifting sinusoidal gratings was calculated. The amplitude of the Fourier coefficient at the fundamental frequency of the stimulus grating (F1) was divided by mean firing rate (F0), after subtracting the mean spontaneous activity from both measures (Crowder et al., 2007). The single unit was defined as a complex cell if its F1/F0 ratio < 1 and as a simple cell if its F1/F0 ratio > 1 (Skottun et al., 1991). Fourier coefficients were calculated by performing Fourier analysis on the spike train using the FFT function in MATLAB.

Nonlinearity characterisation

For each single unit, the F2/F1 ratio was calculated in response to drifting sinusoidal gratings at the optimum orientation. The discrete Fourier transform was used on the spike trains and the F2/F1 ratio was calculated as the ratio of the second harmonic (F2) response over the first harmonic (F1) response. Cells were classified as having nonlinear summation if the F2/F1 > 1 and as having linear summation if the F2/F1 < 1 (Hochstein & Shapley, 1976b).

3.3 Results

We recorded from 234 single units (SUs) that were driven by WGN in the primary visual cortex of six anesthetized wallabies, 195 of which had their spatial RFs uncovered. The spatial RFs were estimated using the nonlinear input model (NIM), which utilises a non-parametric representation for the spatial RF filters and the nonlinear functions applied on the filter outputs. The NIM produced RFs comprising of up to five filters. All the RFs that were characterised using NIM were excitatory and had no significant inhibitory filters. The lack of inhibitory filters is consistent with previous findings in the cat primary visual cortex (Touryan et al., 2005; Almasi et al., 2020). As described in the Methods, a significance test was used to determine the optimum number of filters.

3.3.1 Classification of spatial RFs in V1 cells

The classification of RF types was based on the number of filters that were present in the uncovered RF. Figure 3. shows 20 example units with all the RF filters characterised by the NIM. Example units are presented in rows, labelled from #1–20, and the filter types are laid out in columns, labelled Filter 1–5. The estimated RF filters are all localised. Within the spatial RFs, red regions represent the ON response (i.e. responding to brightness increments of light), blue regions represent the OFF response (i.e. responding to decrements of light). The size of RFs is indicated by the scale bar, which represents 1º in visual space. Units #1–5 are examples of RFs with one spatial filter. Units #1–3 have spatial filters that are tuned to blob-like features of appropriate brightness polarity. Units #4–5 are selective for elongated Gabor-like features with alternate ON and OFF polarities. Units # 6–10 are examples of RFs with two spatial filters. Units #6–7 have two spatial filters with the same orientation, but the spatial phase is shifted by ~90°. Unit #8 has two spatial filters that both have blob-like features tuned to respond to ON-stimuli in their centres (red). Units #9–10 have two spatial filters, with one filter selective for blob-like features of single polarity and another selective for orientation with alternate ON and OFF polarities.

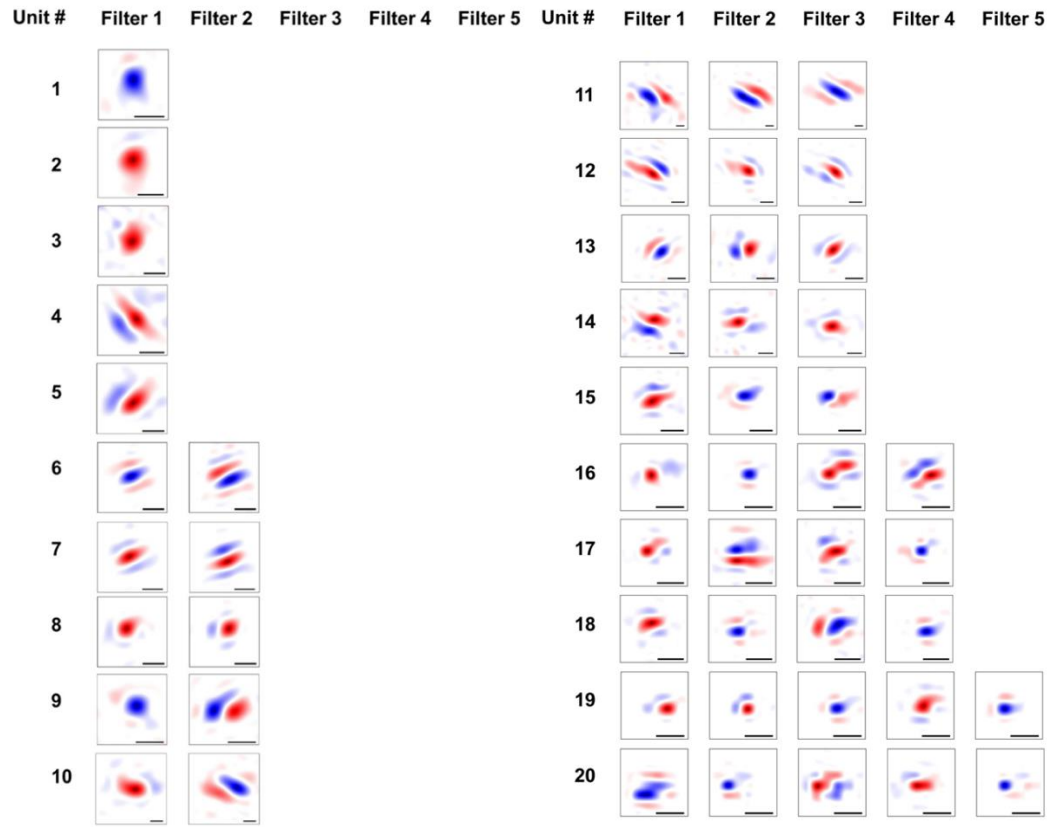

Figure 3.3 Characterization of spatial RFs of V1 cells using the NIM. Twenty example cells that have different numbers of spatial filters are displayed in rows with their corresponding filter types (Filter 1–5).

The second set (Figure 3.: Right) presents examples of units with 3–5 filters. Units #11–15 are examples of RFs with three spatial filters. The three spatial filters of #11–12 have the same preferred orientation, but their phases are shifted by 120° across the different filters. Unit #13 has two filters preferring the same orientation, and one filter with preferred orientation shifted anti-clockwise by approximately 45°. Units #14–15 are examples of RFs showing a mixture of filters responding to blob-like features and Gabor-like features. Units #16–18 are examples of RFs with four spatial filters also responding to both blob-like features and Gabor-like features. Units #19–20 are examples of RFs with five spatial filters. In Unit #19, all its filters respond to blob-like features tuned to various brightness polarities. Unit #20 has a mixture of filters responding to blob-like features and Gabor-like features.

Overall, the number of RF filters varied across the cell population, ranging from 1 to 5. Figure 3. shows a summary of the population data based on the number of filters characterised using the NIM. We found 56% of SUs (n = 110/195) with

one filter (blob or elongated) and 44% of SUs (n = 85/195) with multiple filters. The proportion of single and multiple-filter cells is similar to the proportion of classical simple and complex cells previously found in cat V1 (Almasi et al., 2020). Figure 3.B further categorises the multi-filter units into 2-filter, 3-filter, 4-filter, and 5-filter cells. Out of the multi-filter units, 45% had two filters (n = 38/85); 40% had three filters (n = 34/85); 9% had four filters (n = 8/85); and 6% had five filters (n = 5/85).

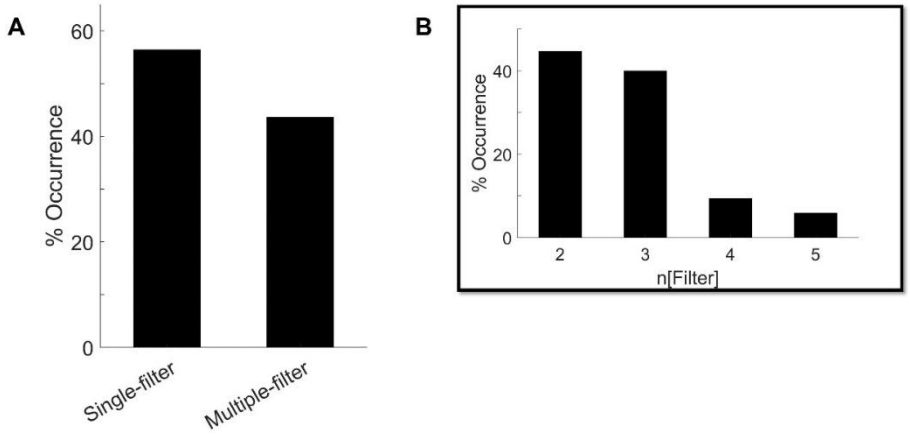

Figure 3.4 Classification of RF filters. **(A)** The bar graph presents the distribution of single- and multi-filter units in the population. **(B)** Distribution of the number of filters for the multi-filter units.

According to the standard linear and energy models, simple cells have one filter, and complex cells have two filters (Schwartz et al., 2006; Sharpee, 2013), although a recent study by Almasi et al. (2020) suggests that both types of cell can have more filters. We classified simple and complex cells from our cell population based on their modulation ratio to drifting sinusoidal gratings (F1/F0 ratio), as shown in Figure 3.A. The F1/F0 ratios for 195 SUs showed a clear bimodal distribution, where the simple and complex cell populations were significantly different from unimodality (Hartigan's dip statistic: $p = 0.03$). Based on the separation line (i.e. F1/F0 = 1), we identified 79 simple cells (in grey bars) and 116 complex cells (in black bars). Figure 3.B shows the distribution of the number of spatial filters identified for simple and complex cells. Many simple cells (grey bar) in our population match the filter number proposed by the linear model, with 84% of simple cells having one filter. However, in the case of complex cells (black bar), a large portion differed from the energy model, with only 28% comprising of two

filters and the remaining 72% varying from one, three, four, or five filters. Importantly, 61% of complex cells had more than two filters, which is a clear sign of their complexity (Figure 3.C).

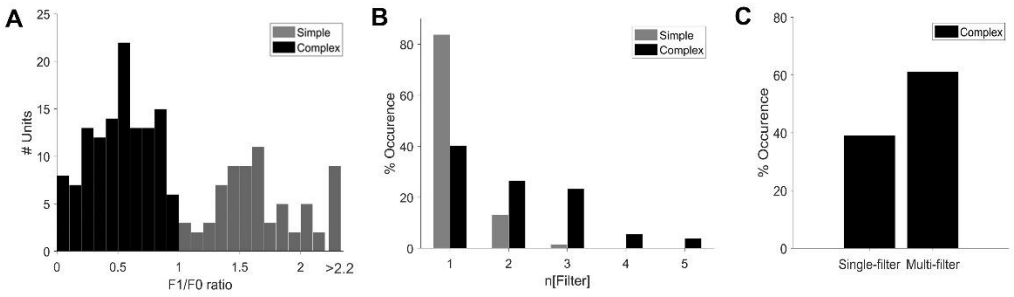

Figure 3.5 Comparison to F1/F0 analysis. **(A)** F1/F0 ratios for the cortical cells. Grey and black columns represent simple and complex cells, respectively. The cells are binned into 0.1 bar widths. Cells with F1/F0 ratios > 2.2 are presented in the far-right bar. The distribution of simple and complex cells was significantly different from unimodality (Hartigan's dip statistic: $p = 0.03$). **(B)** The bar graph shows the distribution of the number of RF filters obtained from NIM for classical simple and complex cells. Note that many simple cells had only a single filter and many complex cells varied from one to five filters when assessed using NIM. **(C)** The bar graph compares the proportion of single and multiple filters in the complex cell population. It is clear that most complex cells have multiple filters, but it cannot be overlooked that nearly 40% of complex cells only revealed a single significant filter.

3.3.2 Feature-contrast nonlinearities in V1 cells.

Neuronal response properties of different cell types are further examined by observing each cell's response profiles as a function of its RF feature-contrast. The feature-contrast for an RF filter is the inner product of the stimulus with the filter and represents the similarity between the stimulus and the filter.

Figure 3. shows the nonlinearities plotted as an input function over the feature-contrast for three SUs. Here, we have only shown the cell nonlinearity prior to the application of the spiking nonlinearity; the latter has a fixed parametric form of a log-exponential function similar to a soft thresholding function. The output of the input function is approximately equivalent to the subthreshold membrane potential. The feature-contrast is presented in arbitrary units (au) as it is normalized to the measured filter. The origin ($x = 0$ and $y = 0$) is indicated by the grey lines on

the plot. The origin, y = 0 corresponds to the spontaneous level of activity. The symmetry index (SI), which describes the similarity between the positive and negative feature-contrasts of the curve, is indicated above the nonlinearity plot. A linear cell, typical of a simple cell, has opposite responses to opposite feature contrasts, resembling a monotonic function (odd symmetric; SI = -1). A linear filter could also respond to one feature-contrast, in which case its input function resembles a threshold-linear function (SI = 0). A nonlinear filter, typical of a classical complex cell, responds equally to opposing feature-contrasts, resembling a squaring function (even symmetric; SI = 1).

Figure 3.A presents an example SU with one spatial filter, which has an odd symmetric-input function (SI = -0.73), showing excitation from one polarity and inhibition from the opposite. Figure 3.B presents an example SU with one spatial filter, which has an even-symmetric input function (SI = 0.93), responding almost equally to both polarities of the RF filter. Figure 3.C shows an example SU with two spatial filters that have two different even-symmetric input functions (SI = 0.36, SI = 0.99).

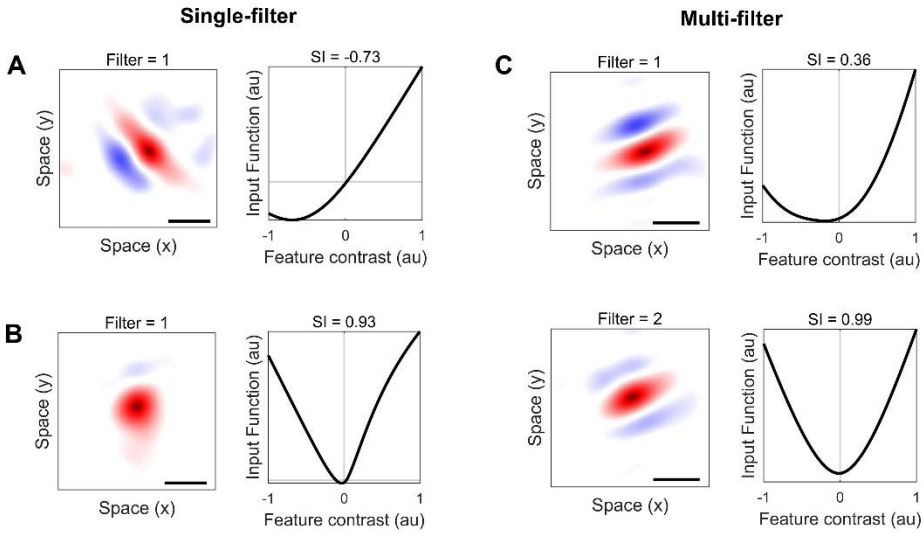

Figure 3.6 Three example SUs with their RFs and corresponding input functions from the NIM. The subregions are represented in red for ON response and blue for OFF response, in x and y space. The black bar indicates 1º in visual space. On the right side of the filters are the respective input nonlinearities plotted as input function over feature contrast (arbitrary units: au), and the grey lines represent the origin (x = 0, y = 0). Above the input function plot is the symmetry index (SI). **(A)** Single-filter unit with an odd symmetric input function (SI = -0.73). **(B)** Single-filter unit with an even symmetric input function (SI = 0.93). (**C)** Multi-filter unit with two spatial filters that have even symmetric input functions (SI = 0.36 and 0.99).

For multi-filter cells, the input functions were heavily biased toward even-symmetric functions (black bars in Figure 3.7A), with 50% of filters showing SIs > 0.75 and less than 10% of filters distributed towards odd-symmetric functions (SIs > 0). For the single-filter cells, the distribution also peaked at even-symmetric input functions (white bars in Figure 3.7A). The even-symmetric input functions for these single-filter cells (example SU in Figure 3.B) show that they respond to opposite polarities of the RF filter, which lead to nonlinearity in their responses. However, the distribution across the SI was more even, with 29% of cells showing SIs > 0.75 and 27% of filters distributed towards odd-symmetric functions (SIs < 0). Moreover, we found that single-filter cells with a modulation index of F1/F0 < 1 (typical of a complex cell) were strongly biased towards even-symmetric functions (86% with SIs > 0; grey bars in Figure 3.7B).

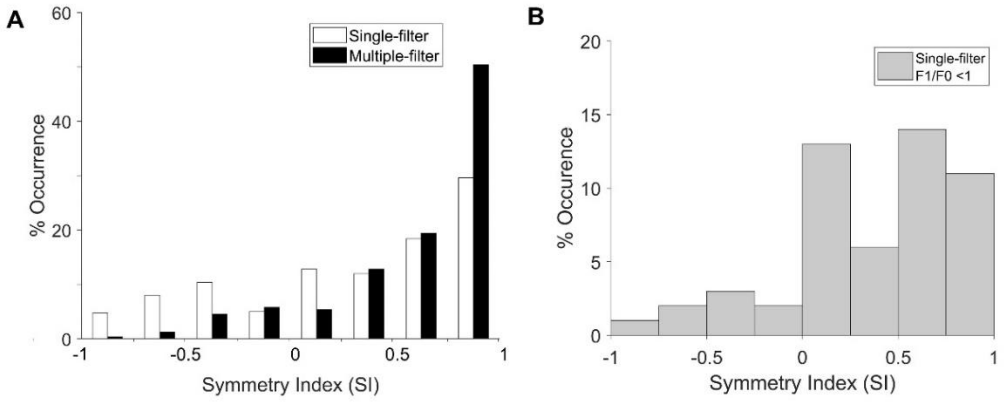

Figure 3.7 Diversity in the input functions of the V1 cells. **(A)** Distributions of the SI of identified input functions for single-filter (white bars) and multi-filter cells (black bars). **(B)** Distribution of the SI of identified input functions for single-filter cells with F1/F0 ratio < 1.

3.3.3 Characterisation of spatial RF filters in V1 cells

The spatial RFs recovered from the subpopulation of single units were characterised into two groups based on their orientation feature: oriented and non-oriented. The filters of the oriented units show significant alignment towards a particular orientation, while the non-oriented units have circular filters with no bias toward any particular orientation. Qualitatively, the two types can be distinguished through their spatial RF structures. Figure 3. shows examples of single units characterised as oriented (Figure 3.A) and non-oriented (Figure 3.B). Red and blue regions of the

RFs represent ON (i.e. selectivity for brightness increments) and OFF (i.e. selectivity for brightness decrements) responses, respectively.

To quantitively determine the type of orientation feature selectivity, the RF filters were transformed into the two-dimensional (2D) spatial Fourier domain (Figure 3.C and Figure **3.**D). The angular and radial coordinates of the Fourier amplitude spectrum represent orientation and spatial frequency coordinates, respectively. As shown in Figure 3.E and Figure **3.**F, we measured the orientation tuning curves by sampling each filter's amplitude spectrum along circular contours (black circle in Figure 3.C and Figure **3.**D), which correspond to all orientations at the filter's maximum spatial frequency (green dotted line in Figure 3.C and Figure **3.**D). For oriented filters, the peak orientation from the amplitude spectrum (the two patches in red) were confined to localised regions at equal but opposite spatial frequencies. On the other hand, for non-oriented RFs, the amplitude spectrum was approximately uniform across the orientation.

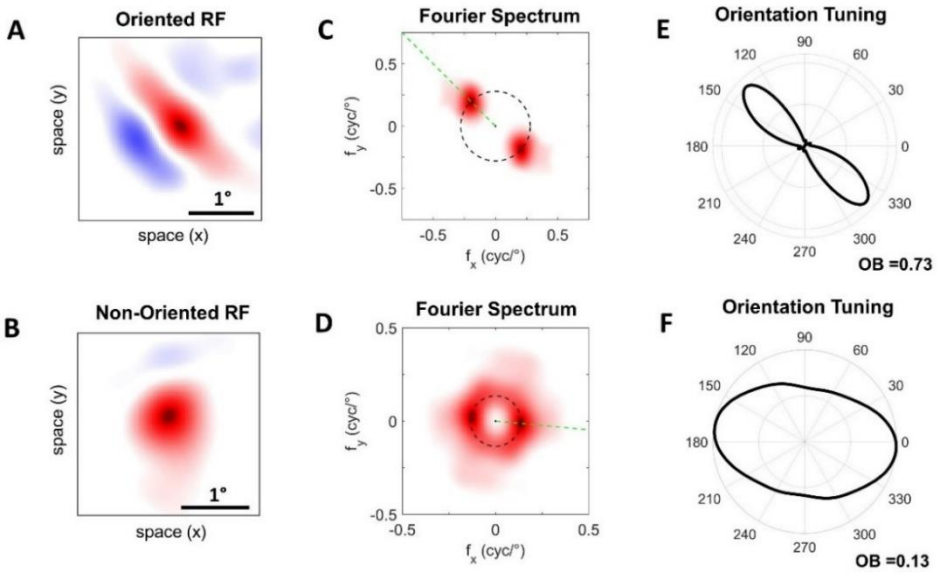

Figure 3.8 Characterisation of V1 cell spatial feature selectivity. **(A–B)** Example single units with **(A)** oriented and **(B)** non-oriented RF filters. Red represents ON responses (i.e. brightness increments) and blue represents OFF responses (i.e. brightness decrements). The black scale bar indicates 1° of visual field. **(C–D)** 2D Fourier amplitude spectrum of the RF filters. The *x* and *y* axes indicate spatial frequency in cycles per degree. The red colour intensity indicates the amplitude of the Fourier spectrum. The black dashed circle indicates the preferred spatial frequency of the filter. The green dashed line indicates the preferred orientation of the filter. **(E–F)** Orientation tuning polar plots obtained by sampling the amplitude spectrum at the preferred spatial frequency (black circles in C and D). OS of cells is quantified with an orientation bias (OB) index, which ranges from 0 (no selectivity) to 1 (narrow selectivity). Cells with OB > 0.2 are classified as non-oriented.

We quantified the OS of every unit with an orientation bias (OB) index, calculated using the circular variance from the amplitude spectrum along the circle passing through the peak amplitude spectrum (see equation 3.11). An OB index of zero is indicative of a cell responding equally to all orientations, while an OB index of one suggests that the cell is responding to only one particular orientation. Hence, OS is greater as the OB index increases. For single units with more than one filter, the OB index was calculated for all filters and the minimum OB was used.

Figure 3.A presents the distribution of OS in OB indices of all the SUs. It is to be noted that the histogram does not show a bimodal distribution that divides the units into oriented and non-oriented types (Hartigan's dip test: $p = 0.12$). Hence, cells around the threshold might show the properties of the two types, because there is no strict boundary. Previous studies have found that non-oriented LGN cells have an OB index of less than 0.2 (Rosenberg et al., 2010; Gharat & Baker, 2017). Hence, after carefully observing the spatial structure of our single unit population, we chose an OB index of 0.2 as the threshold between oriented and non-oriented types, which is the same threshold employed by Gharat and Baker (2017). Examples of the RF filters with different OB indices are shown in Figure 3.B, where RFs with OB values close to 0 show more blob-like features, and filters with OB above 0.2 are more elongated and selective to one particular orientation.

Of all the SUs recorded, 76% were classified as oriented RFs (n = 148/195), and 24% were classified as non-oriented RFs (n = 47/195), as shown in the bar plot in Figure 3.C. We examined the peak orientation of each oriented SU measured from the amplitude spectrum (Figure 3.C). For single units with more than one filter, the peak orientation was calculated for the SU with the minimum OB. Figure 3.8D shows a histogram of orientation preferences measured from 148 SUs with oriented RFs. The preferred orientations of every SU were binned into eight bins of size 22.5°. We found that 58% of SUs were tuned to cardinal angles (i.e. 157.5°–22.5° and 67.5°–112.5°) and 42% to oblique angles (i.e. 22.5°–67.5° and 112.5°–145°). Hence, the percentage of SUs tuned to cardinal angles was greater than that tuned to oblique angles.

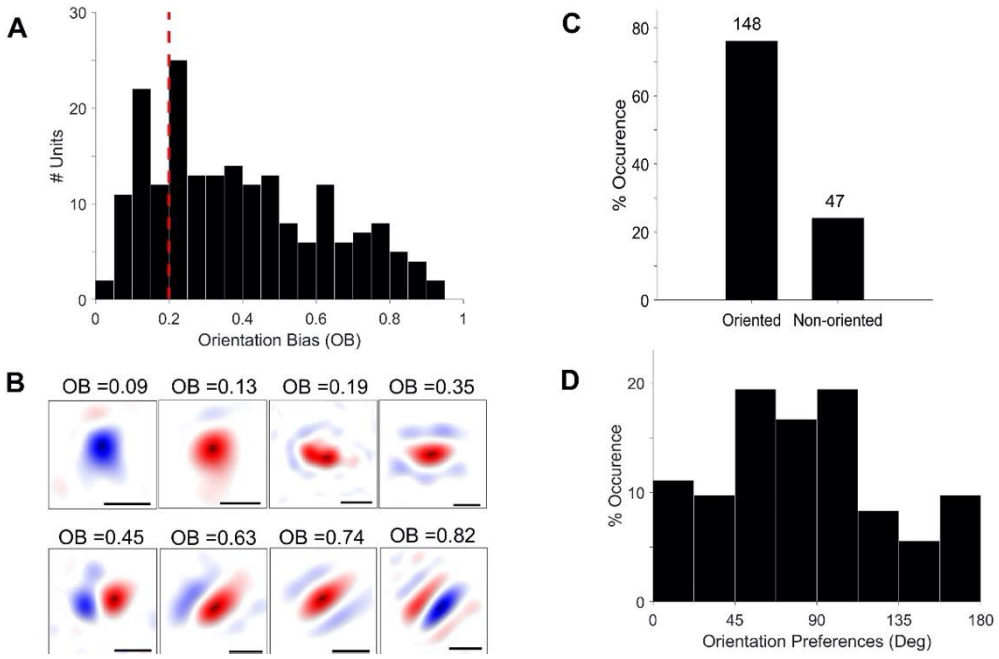

Figure 3.9 OS of cells characterised with OB indices. **(A)** Histogram showing the distribution of OB values of all the 195 SUs recorded. Red dashed line indicates the threshold (OB = 0.2) between non-oriented and oriented types. **(B)** Example RFs with different OB values. RFs with OB < 0.2 are non-oriented and RFs with OB > 0.2 show greater OS as OB increases. **(C)** Bar graph indicating the percentage of SUs classified into two types: oriented and non-oriented. Of all the SUs recorded, 76% (n = 148/195) were oriented and 24% (n = 47/195) were non-oriented. **(D)** Histogram showing the distribution of orientation preference in the 148 oriented SUs, binned into eight bins of size 22.5°.

The OS of cells was also studied using sinusoidal drifting gratings across the RFs, moving in 16 directions equally spaced between 0° and 360°. Figure 3.A shows the histogram of OB values of all the SUs recorded. The same threshold OB = 0.2 was used to define the boundary between oriented and non-oriented types, as the histogram does not show a bimodal distribution to separate the non-oriented classes (Hartigan's dip test: p = 0.15). Figure 3.B shows example tuning curves of cells with different OB values, measured with drifting sinusoidal gratings at the optimal spatial and temporal frequencies of each cell. SUs with OB values close to zero (isotropy) display broad orientation tuning, and, as their OB values reach the transition point, the cells become selective to one particular orientation. The bar graph in Figure 3.C shows that 62% of SUs were classified as oriented RFs (n = 314/506), and 38% were classified as non-oriented RFs (n = 192/506). Figure 3.D shows a bar graph of orientation preferences measured from the 314 SUs with oriented RFs. The orientation preferences for the SU were determined to be the

orientation giving the largest response. We found that many of the SUs were tuned to an orientation of 90° (23%, n = 72/314) and 0° (13%, n = 40/314), This is consistent with our optical imaging recordings (see Section 2.2), where we also find a strong bias towards cardinal angles in the OP maps.

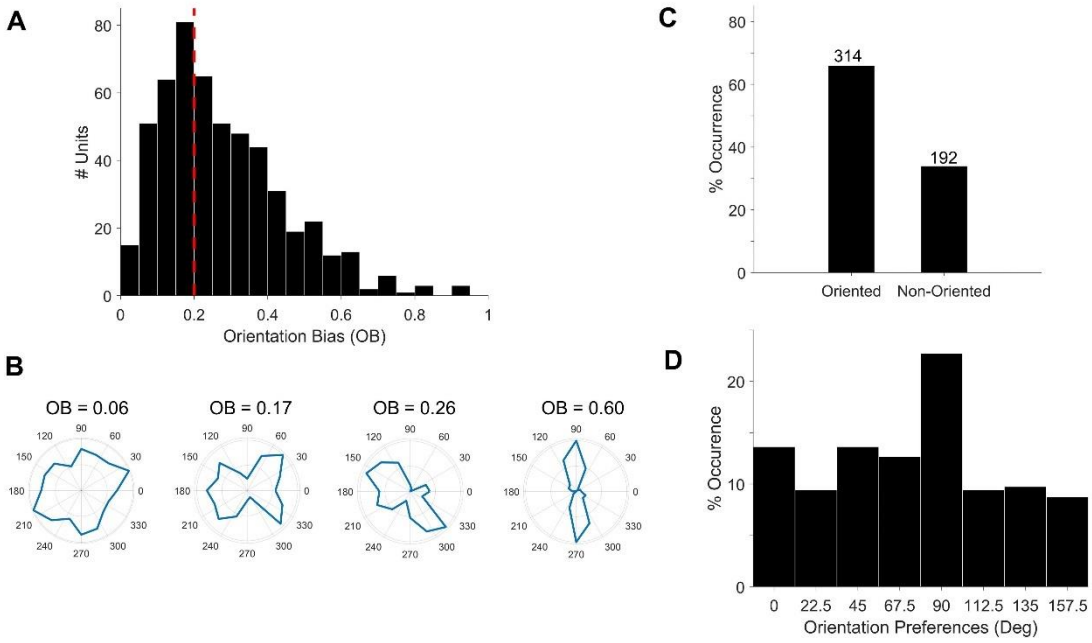

Figure 3.10 OS of cells characterised with an OB index. **(A)** Histogram showing the distribution of OB values of all the 506 SUs recorded in response to oriented gratings. Red dashed line indicates the threshold (OB = 0.2) between non-oriented and oriented types. **(B)** Example tuning curves with different OB values. **(C)** Bar graph indicating the percentage of SUs classified into two types: oriented and non-oriented. Out of all the SUs recorded, 62% (n = 314/506) were oriented and 38% (n = 192/506) were non-oriented. **(D)** Histogram showing the distribution of orientation preferences in 314 oriented SUs, binned into eight bins of size 22.5°.

3.3.4 Classification of spatial RFs in LGN cells

We recorded 12 isolated SUs driven by WGN in the LGN of one anesthetised wallaby from which we were also able to recover their spatial RFs. Unfortunately, the COVID-19 crisis of 2020 prevented us from conducting two further scheduled experiments. Due to imposed restrictions, these experiments had to be delayed until after the PhD candidature, so the reported cell numbers are lower than expected. The spatial RFs were estimated using the NIM. The electrode was driven vertically to a depth of 11–13 mm, going through 10 mm of the cerebral cortex before penetrating the thalamus, using the stereotaxic coordinates described by Wye-Dvorak et al. (1987). Figure 3.2A displays a diagram of the 32-channel single shank

multi-electrode array (MEA) that was used to record the visual responses. The scale bar represents 1 mm, with 0.1 mm spacing between channels. The depth of each SU was estimated by considering how deep the electrode was relative to the surface and the channel of the electrode in which the SU appeared. For example, if the first track was vertically inserted to a depth of 11mm, channels 1 to 11 (marked in red) represent the depths between 10mm–11 mm. The depth information and the RF characteristics found in histologically confirmed LGN cells were used to classify SUs as those originating from the LGN.

Figure 3.2B shows the 12 isolated SUs with RFs filters characterised by the NIM. We found all SUs to be tuned to blob-like features of appropriate brightness polarity presented within their RFs. 10 SUs responded to ON polarity (i.e. brightness increments), and 2 SUs responded to OFF polarity (i.e. brightness decrements). The size of RFs is indicated by the scale bar representing 1^{o} in visual space. The SUs recorded from LGN have very small RFs, with a size of half a degree of the visual field. The average response latency of a SU was determined by observing the time it took to start spiking following a stimulus presentation. Figure 3.C shows the spatiotemporal STAs computed for an example SU from the LGN. The temporal binning used was 10 msec, with the time shown above each filter in msec. It appears that the pattern in the STAs becomes visible between 20 and 30 msec, which indicates that the STAs onset occurs at these times. We also established the post-stimulus time histogram (PSTH), as shown in Figure 3.2D. Time 0 msec represents the start of the stimulus presentation, and 66.69 msec marks its end. The responses are binned into 3 msec bins. The latency was calculated by determining when the spike rate reaches 15% of the peak firing rate. The average response latency of the 12 isolated SUs was calculated to be 27 msec ± 2 msec. The example cell shown in Figure 3.2D has double peaks on the PSTH, with the first peak occurring at 25 msec, followed by the second peak occurring at 50 msec. This is an example of the classic centre surround response previously reported in LGN cells (Durand et al., 2016). Figure 3.2E shows the mean spike rate of LGN units with SEM represented by a red error bar (mean ± SEM: 2.2 ± 0.27 spks/sec).

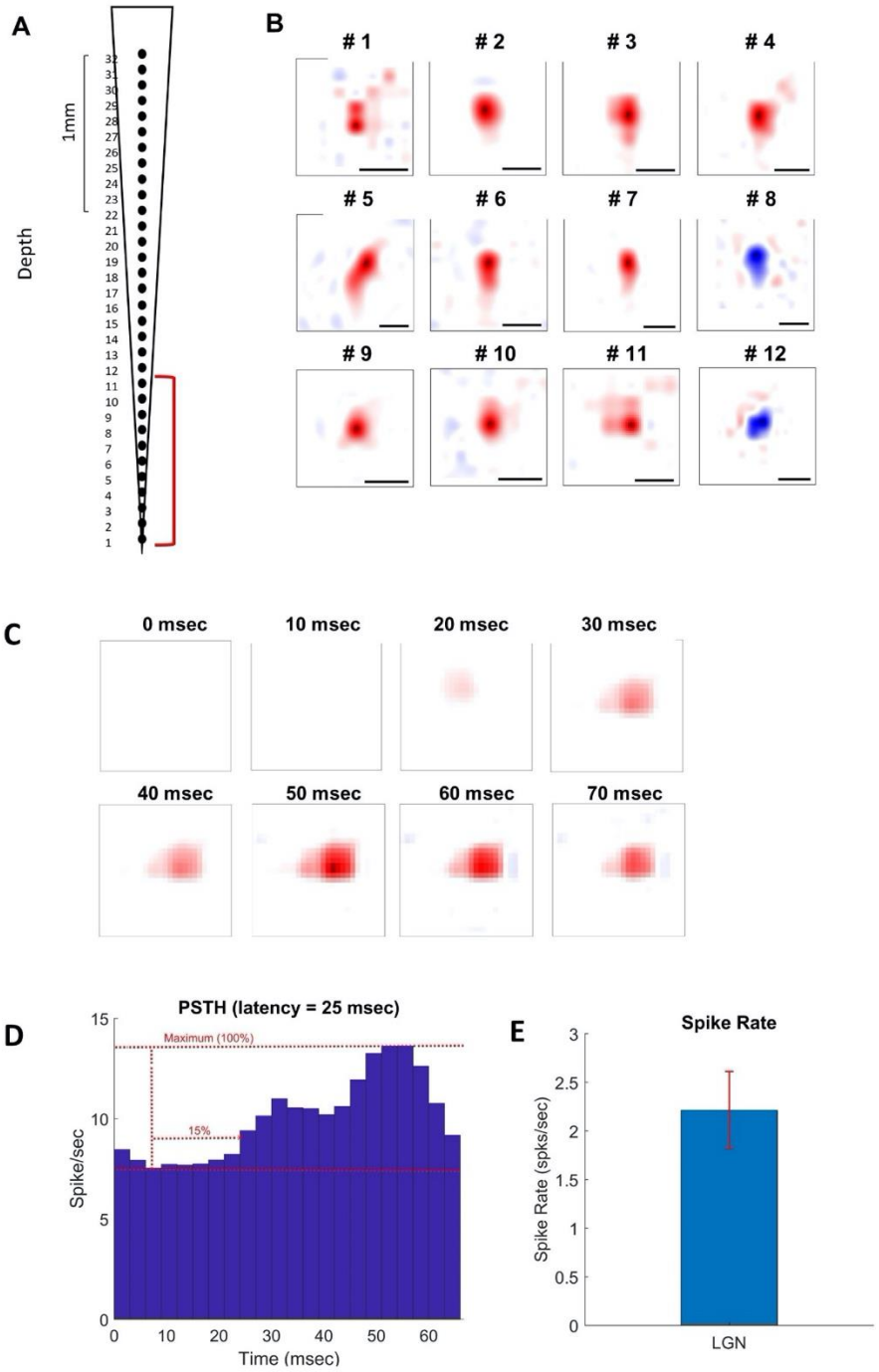

Figure 3.2 Recordings from LGN cells. **(A)** Schematic diagram of 32-channel MEA that was used to record from the LGN. The electrode was vertically inserted to a depth of 11 mm-13 mm. The black vertical scale bar indicates 1 mm (while the space between the channels is 0.1 mm). The red bracket on the right indicates the channels where LGN cells were found. **(B)** Spatial RFs of 12 SUs obtained in LGN using the NIM. The black scale bar indicates 1 degree of visual field. **(C)** The spatio-temporal STAs computed from one of the LGN-units. The temporal binning used was 10 msec. **(D)** PSTH from one LGN-unit. The responses (spikes/sec) are binned into 3 msec bins. The red dashed lines are the minimum (0%) and maximum (100%) spike rates. Latency is determined as the time after the minimum when the first bin reaches 15% threshold. The latency of this unit is 25 msec. **(E)** Bar plot showing the mean spike rate of LGN units. SEM is represented by red error bar (mean ± SEM: 2.2 ± 0.27 spks/sec).

3.3.5 Feature-Contrast Nonlinearities in LGN cells

For the LGN units, we also examined the response profiles as a function of their RF feature-contrasts. Figure 3.3 shows the nonlinearities plotted as an input function over the feature-contrast (arbitrary units: au) from two example SUs. The symmetry index (SI) is indicated above the nonlinearity plot. Both example SUs in Figure 3.3 have linear filters with odd symmetric-input functions (SI = -0.35, SI = -0.99). In fact, for LGN cells, the input functions were significantly biased towards odd-symmetric-input functions, with 92% (n = 11/12) of RF filters showing SIs < 0 and one SU with SI = 0.03. This means that all the RFs obtained were linear and responded mostly to one particular polarity of feature-contrast, resembling simple cells.

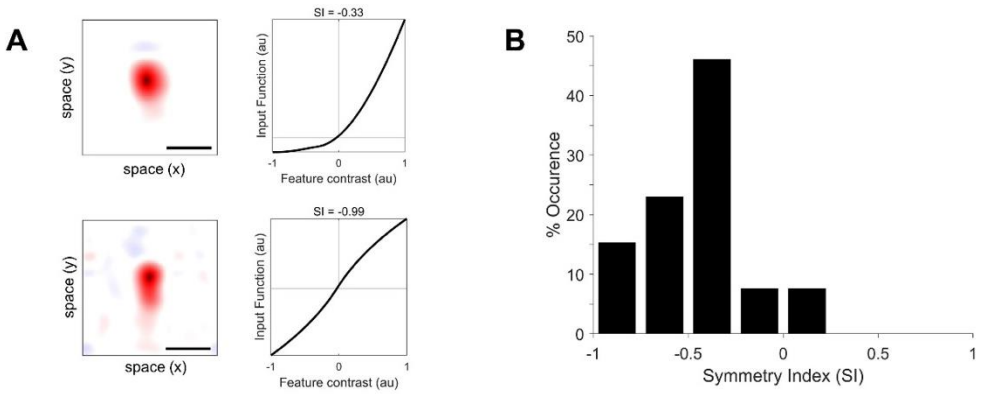

Figure 3.3 Nonlinearities in LGN cells. **(A)** Two example SUs with their RFs and corresponding input functions from the NIM. The subregions are represented in red for ON response and blue for OFF response, in x and y space. The black bar indicates 1º in visual space. On the right side of the filters are the respective input nonlinearities plotted as input functions over feature contrast (arbitrary units: au), and the grey lines represent the origin ($x = 0$, $y = 0$). Above the input function plot is the symmetry index (SI). Top line: Single-filter unit with an odd symmetric input function (SI = -0.33). Bottom line: Single-filter unit with an odd symmetric input function (SI = -0.99). **(B)** Distributions of the SIs of the identified input functions for individual filters in our population of LGN cells. 92% of SUs had SI > 0 (n = 11/12).

The LGN cell population was classified as linear or nonlinear based on its F1/F0 ratio when responding to moving gratings. For all 12 SUs recorded in LGN, the F1/F0 ratio > 1 and skewed toward higher values (Figure 3.4A; median = 2.09). Based on the calculated F1/F0 ratios, all LGN cells recorded were classified as linear, having phase sensitivities that would be normally associated with simple

cells. Moreover, the LGN cell population was further classified into two types: linear or nonlinear based on its nonlinearity index, which is defined as the F2/F1 ratio (Gharat & Baker, 2017). If a cell had a F2/F1 ratio < 1, it was classified as linear, otherwise as nonlinear. For all 12 SUs recorded in LGN, the F2/F1 ratio was < 1 and skewed toward lower values (Figure 3.4B). Based on their F2/F1 ratios, all LGN cells recorded were classified as having linear summation properties.

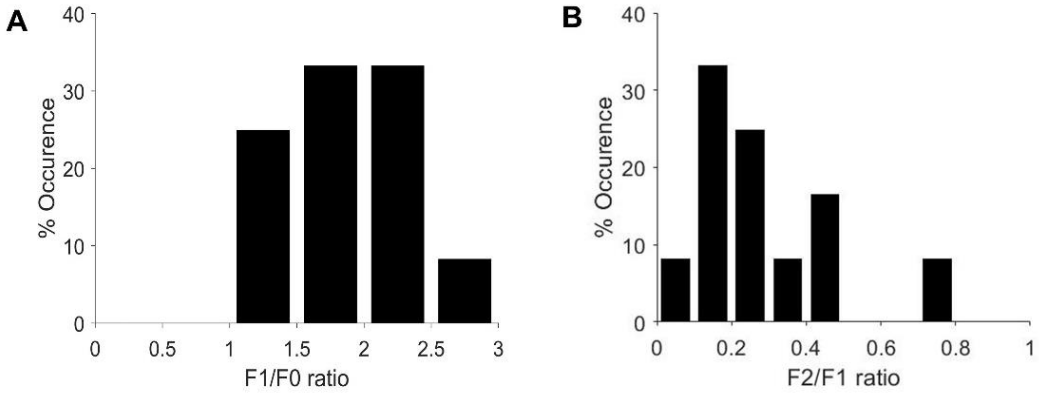

Figure 3.4 Fourier Analysis of LGN cells. **(A)** F1/F0 ratios for the recorded LGN cells. The cells are separated into bins of 0.5 ratios. **(B)** F2/F1 ratios for the recorded LGN cells. The cells are separated into bins of 0.1 ratios. Note that all LGN cells have F2/F1 ratios below 1, which indicates linear summation.

3.3.6 Characterisation of spatial RFs in LGN cells

The OS of cells in the LGN was measured in response to both WGN and drifting gratings. Figure 3.5 shows an example RF filter transformed into the 2D spatial Fourier domain. We measured the orientation tuning curve by sampling the filter's amplitude spectrum along the contour line (black circle in Figure 3.5B), which represents all orientations at the filter's preferred spatial frequency. The example LGN cell has relatively broad tuning for orientation, with an OB index of 0.13 (Figure 3.5C). Figure 3.5D shows a broad orientation tuning measured from the same cell's response to drifting gratings (OB = 0.15). We plotted a histogram of distribution of OB values of all 12 LGN SUs (blue bars) on top of the distribution of OB values of all V1 SUs (black bars) recorded in response to WGN (Figure 3.5E). Where cortical cells had a mean OB of 0.45 ± 0.05, the LGN cells were poorly tuned with a mean OB of 0.17 ± 0.07. Similarly, in Figure 3.5F, OB values

calculated from responses to drifting gratings were plotted for LGN SUs (blue bars) and V1 SUs (black bars).

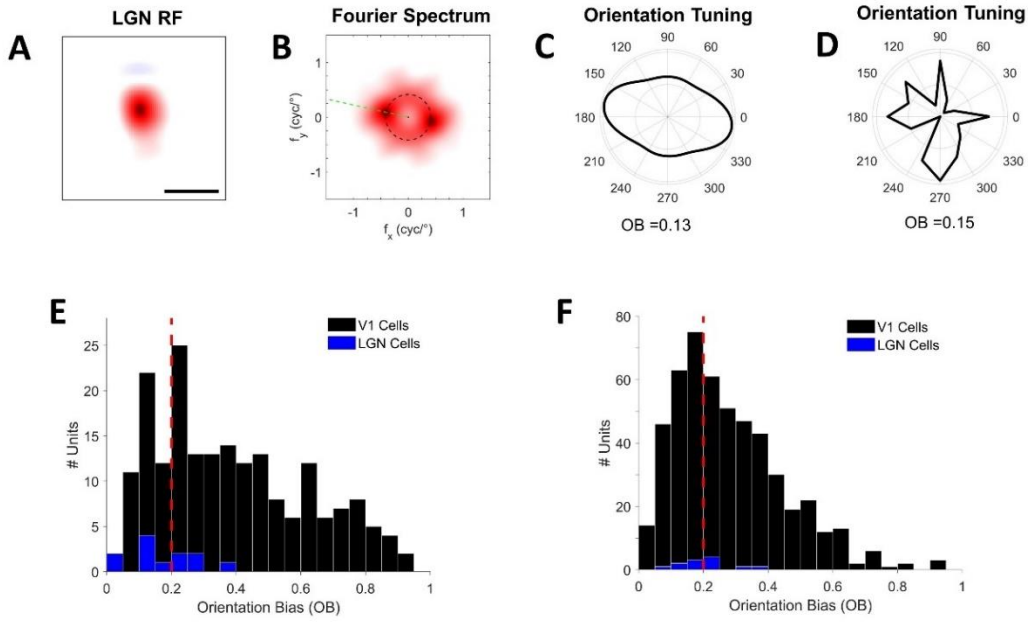

Figure 3.5 Characterisation of spatial feature selectivity of LGN cells. **(A)** An example SU with a non-oriented RF. Red represents the ON response (i.e. brightness increments) and blue represents the OFF response (i.e. brightness decrements). The black scale bar indicates 1° of visual field. **(B)** The 2D Fourier amplitude spectrum of the RF filters. The x and y axes indicate spatial frequency in cycles per degree. The red patches indicate the peak amplitude. The black dashed circle indicates the preferred spatial frequency of the filter. The green dashed line indicates the preferred orientation of the filter. **(C)** Orientation tuning polar plots obtained by sampling the amplitude spectrum at the preferred spatial frequency (black circles in C). **(D)** Corresponding orientation tuning curve obtained using sinusoidal gratings. **(E)** Histogram shows the distribution of OB values of all 12 SUs recorded in LGN (Blue) and 195 SUs recorded in V1 (Black) in response to WGN. **(F)** Histogram shows the distribution of OB values of all 12 SUs recorded in LGN (blue) and 575 SUs recorded in V1 (black) in response to oriented gratings. The red dashed line indicates the threshold (OB = 0.2) between non-oriented and oriented types.

3.4 Discussion

3.4.1 Receptive fields and classification of V1 cells

In this study, we applied the NIM framework to SU recordings in anaesthetised tammar wallaby V1 and LGN. The NIM estimation method allowed us to uncover spatial RFs in V1 and LGN, with minimal constraints on the form of response nonlinearity (McFarland et al., 2013). Previous studies have estimated RFs using the NIM with sequentially fitted parameters, which is likely to cause biased estimates (Rowekamp & Sharpee, 2011). However, in this study, we have estimated all parameters simultaneously in the NIM with a maximum likelihood optimisation technique as described by Almasi et al. (2020). This identifies the best maxima from multiple local peaks and avoids biased estimates.

We have identified one to five RF filters across the V1 cell population (Figure 3.). Each RF filter represents a distinct feature of visual space, and the number of filters represents the complexity observed in a cell's response profiles. According to the standard models for V1 cells, one filter is present in simple cells, and two filters are present in complex cells (Skottun et al., 1991; Touryan et al., 2002; 2005). As reported in earlier studies, the neurons in the primary visual cortex of the tammar wallaby are classified as simple and complex cells based on F1/F0 ratios (Figure 3.A). Using this classification of simple cells and complex cells, we found that 84% of simple cells in our population were found to have one filter while complex cells had a more varied distribution of filters, with 62% being multi-filter (Figure 3.B, Figure **3.**C). This is in line with recent studies that have estimated spatial RFs with extra filters than indicated by the standard models (Rust et al., 2005; Chen et al., 2007; Fournier et al., 2014). Rust et al. (2005) reported in macaque V1 that multiple filters can exist in many simple cells, and likewise, more than two significant RF filters can be present in complex cells. Recent studies have highlighted the diversity of filters and phase insensitivity of complex cells, suggesting that both simple and complex cells integrate properties of nonlinear spatial summation that are not described by the standard models for each cell type (Chen et al., 2007; Fournier et al., 2014; Yunzab et al., 2019; Almasi et al., 2020).

Here, we found filters with purely excitatory and mixed excitatory-suppressive filters, but no SUs with purely suppressive filters. However, this is not to suggest that NIM was unable to identify SUs with suppressive filters because we had identified input functions with suppressive effects during RF estimation. Our findings were consistent with several studies that have conducted extracellular recordings in cat V1 (Touryan et al., 2002; 2005; Almasi et al., 2020). This is in contrast to other studies that have found purely suppressive filters in RFs at the membrane potential level in cat V1 (Fournier et al., 2014) and in monkey V1 (Rust et al., 2005; Chen et al., 2007). The lack of suppressive filters might be linked to the relatively low numbers of recorded spikes in V1 from extracellular recordings or interspecies differences. In addition, some studies have suggested that the discrepancy might be related to the effect of anaesthetics on neural recordings, as certain types of anaesthetics (i.e. halothane, as used here) impacts the inhibitory receptors by potentiating GABA and Glycine receptors (Touryan et al., 2002; 2005; Goldstein, 2015).

The maximum number of RF filters recorded in a wallaby V1 cell was five excitatory filters, which is consistent with what has been previously reported in cat V1 (Touryan et al., 2002; 2005; Almasi et al., 2020). However, when compared to monkey V1, where up to eight excitatory filters were found, it is substantially lower (Rust et al., 2005; Chen et al., 2007). Besides the variability across species, the low number of filters may also be attributed to the type of stimulus used. The number of filters we estimated represents a lower bound on the true number for each cell. In addition, the use of stimuli like natural scenes may uncover more spatial filters because of their richer statistical regularities compared to WGN (Butts, 2019). However, we decided to use WGN stimuli because it is the most general stimulus possible and using WGN reduces any possible methodological bias for estimating RFs.

3.4.2 Nonlinearities

For the first time, we provided a quantitative analysis of the feature-contrast response function at the population level in the tammar wallaby. The input function for each filter was characterised by a symmetry index around zero feature-contrast.

Traditionally, simple cells are modelled as having linear filters with a monotonically increasing input function with opposite responses to opposite feature-contrasts (odd symmetric). On the other hand, complex cells are modelled as having nonlinear filters in the form of a squaring function that responds equally to opposing feature-contrasts (even symmetric) (Touryan et al., 2002; 2005; Rust et al., 2005; Chen et al., 2007).

However, we found that almost 30% of single-filter cells, traditionally considered to be simple cells according to the standard linear model (Simoncelli & Llampaninski, 2004), exhibited even-symmetric input functions (Figure 3.7A). This discrepancy is explained by considering the F1/F0 ratio of the single-filter cells. We found that close to 86% of single-filter cells were classified as complex cells when using grating stimuli and calculating an F1/F0 ratio. They tended to have even-symmetric input functions and behaved more like complex cells than simple cells, despite only having one filter. It has been noted that a hard boundary between simple and complex cells based on F1/F0 ratios cannot be found even in cat cortex (Hietanen et al., 2013). The calculation of the F1/F0 ratio is heavily dependent on the number of spikes available for the analysis and, while complex cells are often said to be phase invariant, many complex cell responses actually oscillate quite strongly when stimulated with drifting gratings. The data from the wallaby concurs with these observations in that many single-filter units have nonlinear characteristics, which are revealed as F1/F0 ratios below unity when using grating stimuli.

For multiple-filter cells, the peak of the distribution was at even symmetric functions (Figure 3.7A). However, we found that the input functions for multi-filter cells were not all quadratic-like, and mostly deviated from a perfectly even-symmetric form. Overall, we found a greater diversity in feature-contrast response functions than advised by the energy model in our multiple filter cells (Adelson & Bergen, 1985). Other studies have also reported a similar deviation from even symmetric forms for complex RF filters (Spitzer & Hochstein, 1985; Touryan et al., 2005; Almasi et al., 2020).

The NIM framework provides for a far more comprehensive and less biased analysis of RF properties. It reveals that there is more variation in RF structure than

thought based on prior analysis using grating stimuli and simplistic F1/F0 analysis. There is a reasonable correlation between the grating-based and NIM-based analysis, but the grey area between the classification of simple and complex cells is partially explained by the more complex RF structures revealed by NIM. Greater variation in RF structures was already noted in cat cortex (Almasi et al., 2020). We have now extended this finding to the marsupial cortex.

3.4.3 Receptive fields and classification of LGN cells

We applied the NIM to the LGN cells of the tammar wallaby in response to WGN stimuli, as we did with V1 cells. We found circular ON/OFF-centre RFs, which responded to light stimuli (ON-centre response) and dark stimuli (OFF-centre response), as described in the initial feed-forward model of the cortical hierarchical pathway (Hubel & Wiesel, 1962) (Figure 3.2). Our findings are also consistent with what has been reported previously about the responses of LGN cells in the tammar wallaby when using hand-held stimuli (Wye-Dvorak et al., 1987; Henry & Mark, 1992). For the first time, we demonstrated the specific types of nonlinearity that underly the LGN of the tammar wallaby. The majority of LGN cells displayed linear summation properties, as indicated by the SI and F1/F0 ratios (Figure 3.3B; Figure **3.4**A). This is consistent with reports on other species, which displayed linear summation characteristics in most LGN cells (mouse: Grubb & Thompson, 2003; Piscopo et al., 2013; cats: Hochstein & Shapley, 1976a; Ferster & Jagadeesh, 1991; monkeys: Usrey et al., 2000; Xu et al., 2002).

It is known that there are distinct types of retinal ganglion cells that provide input to LGN cells, and they correlate with the distinct X and Y classes of LGN units, which can be determined based on the cell's spatial summation (Hochstein & Shapley, 1976a; So & Shapley, 1979; Kaplan & Shapley, 1982). The responses of X cells have a distinct linear component, while the responses of Y cells have a distinct nonlinear component. We found that all LGN cells recorded in the tammar wallaby had linear summation characteristics. As we used drifting gratings, we do not have the ability to directly compare these linear summation properties with those known from using contrast reversing gratings, we can comment about the linearity, or otherwise, of the responses. Given that the response had linear

characteristics, the cells are closer to the expectation for X-like cells in the retina and LGN (Figure 3.4B). The results suggest but do not definitively prove that one type of retinal ganglion cells dominates the input to wallaby's LGN cells, i.e. X-cells. This is consistent with cats and monkeys, where the majority of LGN cells were classified as X-like (Enroth-Cugell & Robson, 1966; Hochstein & Shapley, 1976a; Kaplan & Shapley, 1982). However, this conclusion might be biased by our small sample size. Due to COVID-19 restrictions, we were unable to conduct more LGN experiments, but we plan to do so in the future.

3.4.4 Emergence of OS in the visual pathway

Non-oriented RFs in wallabies

In previous studies of the visual cortex, almost all units were reported to display RFs with oriented ON/OFF subregions (Cardin et al., 2007; Van Hooser, 2007). However, recent studies have reported units with circular RFs showing no or low OS (Kremkow et al., 2016; Talebi & Baker Jr, 2016; Gharat & Baker, 2017; Almasi et al., 2020). The discrepancy has been explained by a selection bias in the sampling of RFs in previous studies, which used single electrodes to search for RFs with oriented bars or edges (Talebi & Baker Jr, 2016). It could be argued that searching for cells with gratings might bias selection towards orientation-selective cells. In our study, MEAs were inserted into the cortex 'blindly' without searching for RFs, which reduced the likelihood of human-derived selection bias (as described in Talebi & Baker Jr, 2016; Gharat & Baker, 2017; Almasi et al., 2020). This objective sampling technique uncovered a high portion of non-oriented RFs (24%; Figure 3.C). It is interesting that, when using similar MEA recording techniques in cat cortex, our research group also identified far more non-oriented RFs than has been typically reported (Almasi et al., 2020).

OS in the tammar wallaby V1cells

Despite the presence of non-oriented RFs, three-quarters of the neurons in the tammar wallaby V1 had oriented RFs (76%; Fig. 3.9C). This is also reasonably consistent with our findings using sinusoidal gratings, which found 62% of neurons in V1 to be orientation-selective (Figure 3.C) (also in line with findings from Ibbotson et al., 2005). Further, this is consistent with studies finding high OS in cat

and monkey visual cortex (65–70%; cat: Hubel & Wiesel, 1963; Ferster et al., 1996; Alonso et al., 2001; monkeys: Hubel & Wiesel, 1968; Bullier & Henry, 1980). However, 76% OS in wallaby is substantially higher than the percentage of OS in the visual cortices of the two previously studied marsupial species; the Australian brush-tailed possum and the American opossum (Crewther et al., 1984; Rocha-Miranda et al., 1976). They have been reported as exhibiting substantially lower percentages of orientation-selective neurons (~30%), and consequently, higher percentages of cells with non-oriented RFs. The differing results amongst marsupials could indicate that OS in V1 is not dependent on phylogenetic classification. Rather, these results might indicate that the primitive mechanisms underlying the development of OS are likely to have been altered by differing environmental factors. In the case of the wallaby, they are active during the day and highly social animals. It is possible that the development of good vision (i.e. high OS) in wallabies is driven by their highly social lifestyle. On the other hand, the low percentage of orientation-selective neurons in the visual cortex of brush tailed possum may be due to their largely nocturnal lifestyle (Crewther et al., 1984).

However, before making such large claims, it is important to note technical differences. The previous marsupial research was conducted many years ago using stimulation and analysis equipment and techniques that were far less sophisticated than that used here. In just one example, the ability to very selectively identify specific spikes potentially offers much better ability to get accurate response characterisation from single cells. It is also the case that the anaesthetics and muscular blockers that were used then and now are very different. In Rocha-Miranda's study (1976), nitrous oxide was used as the sole anaesthetic agent during extracellular recordings with opossums. Nitrous oxide, which has been widely employed in the early electrophysiological experiments, potentiates inhibitory receptors (i.e. $GABA_A$ and Glycine receptors) and conversely inhibits glutamate and nicotinic acetylcholine receptors (nAChRs), which impedes fast excitatory neurotransmission (Emmanouil & Quock, 2007). It has been revealed that under nitrous oxide, responses to visual stimuli are severely reduced and frequently abolished (Mandl et al., 1980; Sebel et al., 1984; Langeron et al., 1999). Hence, the lack of orientation-selective cells in opossums reported by Rocha-Miranda et al.

(1976) may be related to the effects of anaesthetic impeding neural activity in the visual cortex.

OS in tammar wallaby LGN cells

In this study, we were interested to know if the LGN cells of the tammar wallaby were orientation selective, in the same way as V1 cells. Previously, Wye-Dvorak et al. (1987) detected a couple of cells in the LGN with RFs that were oriented horizontally along with the visual streak but, in their study, no quantitative measurement of OS was made from the LGN cells. We are the first to quantitatively interpret OS in LGN cells of the tammar wallaby. We found that LGN cells in the tammar wallaby have mostly non-oriented RFs, with some very weakly orientation biased (Figure 3.5). Of the twelve LGN cells characterised in this study, 33% of them displayed slightly elongated RFs. Tang et al. (2016) suggested that those LGN cells with elongated RFs could result from the summation of two circular retinal RFs with a slight offset in location. Weak orientation biases could occur when LGN cells receive inputs from two direction-selective RGCs with opposite preferred direction (Marshel et al., 2012). It will be interesting to further examine the connectivity of RFs from RGCs to LGN by taking advantage of recent imaging techniques (Marshel et al., 2012; Yang et al., 2016; Adam et al., 2019) to clearly distinguish these mechanisms.

The underlying mechanisms for emergence of OS appear to be different across species. For example, in rodents and rabbits, OS emerges in the retina (mouse: Dräger, 1975; Metin et al., 1988; Ohki et al., 2005; rabbit: Stewart et al., 1971; Venkataramani & Taylor, 2010), which is inherited by LGN cells and, ultimately V1 neurons. In cats and primates, cortical OS emerges from less selective LGN cell inputs (Hubel & Wiesel, 1968; Ts'o et al., 1990; Bosking et al., 1997). Several factors may influence the emergence and organisation of OS including; the lateralisation of the eyes, the existence of a fovea, the degree to which animals are nocturnal or diurnal, and the need for good vision for a given species. We suggest that, despite the ubiquity of cortical OS, a diverse range of mechanisms is present when it comes to the method by which OS is represented in the visual cortex.

The relationship between emergence of OS in the visual pathway and OP maps

It is possible that the formation of OP maps relates directly to the existence of subcortical OS. Our results from the tammar wallaby confirms that species with highly structured OP maps are likely to have the OS pushed further up the hierarchical visual pathway into the cortex. It is plausible that animals with a high CP ratio and thus less cell diversity in their central retina create OS in cortex *de novo* and this, in turn, leads to more structured OP maps. Conversely, species with orientation-selective LGN cells are likely to send signals into V1 in a random spatial order, thus imposing a salt-and-pepper arrangement on the cortex.

3.5 Conclusion

In conclusion, OS observed in the primary visual cortex (V1) of marsupial wallabies emerges from less selective LGN cell inputs, which is similar to that found in the V1s of most mammals. Species in the Clade Glires (i.e. rodents and rabbits) have OS emerging early in the visual pathway, suggesting that they have different mechanisms for visual processing compared to other mammals. As discussed above, the emergence of OS in the visual pathway and the formation of OP maps may be influenced by the density of cells providing input to the cortex. Furthermore, the NIM framework provided a far more comprehensive analysis of RF properties of neurons in the marsupial cortex, with greater variation in RF structures of simple and complex cells than reported based on simplistic F1/F0 analysis.

Abbreviation	Meaning
2D	Two-dimensional
NIM	Nonlinear input Model
WGN	White Gaussian Noise
LED	Light-emitting diode
MEAs	Multi-electrode Arrays
SV	Singular value decomposition
SU	Single unit
SI	Symmetry Index
OB	Orientation Bias
FFT	Fast Fourier Transform
SEM	Standard Error Mean
GABA	Gamma aminobutyric acid
nAChRs	Nicotinic acetylcholine receptors

Chapter 4

4.1 Introduction

Neurons in the visual cortex fire action potentials when visual stimuli appear within their receptive fields (RFs). Over the past decades, recordings of action potentials (or spikes) have been very useful in determining the response properties of individual neurons and how these neurons communicate with each other across the various stages of the visual system, i.e. the lateral geniculate nucleus (LGN) and the primary visual cortex (V1)(Hubel & Wiesel, 1959, 1961, 1962). As discussed in the previous chapter, we know from early electrophysiology studies that most LGN cells have non-orientation selective centre-surround RFs and that V1 cells have elongated, orientation selective RFs with either discrete ON and OFF regions (i.e. simple cells) or without segregation of ON and OFF regions (i.e. complex cells).

Intracellularly, spike waveforms are classically described as having four different phases: (1) resting membrane potential; (2) depolarisation when Na+ channels open and Na+ ions enter the cell; (3) repolarisation when Na+ channels close, K+ channels open and K+ ions exit the cell; and (4) hyperpolarisation when K+ channels close slowly. This is illustrated in Figure 4.1. However, this classical description is based on recordings from large squid axons (Moore & Adelman Jr, 1961). In fact, intracellular spike shapes can vary from this basic plan for a range of reasons, e.g. the type of neuron, the brain area and the location of the electrode relative to the cell body (Dyball et al., 1991; Quirk & Wilson, 1999; Gold et al., 2006; 2009). Importantly, recordings from cell bodies (somas), rather than axons, which is the most common situation in cortical studies, have a range of shapes that depend on the cell class (Mason & Larkman, 1990; Stuart et al., 1993). Previous studies have found that different spike-waveform shapes correspond to different

neuronal classes in V1. For example, in cat V1 broad spike-waveforms (i.e. regular spiking) arise from excitatory neurons (often pyramidal neurons), whereas narrow spike-waveforms (i.e. fast spiking) originate from inhibitory neurons, e.g. basket and chandelier cells (Ahmed et al., 1998; Azouz et al., 1997; Henze et al., 2000).

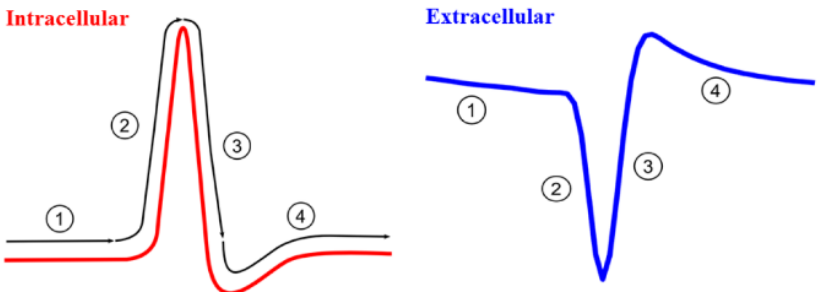

Figure 4.1 Red waveform: a typical intracellular spike recorded from an axon. Blue waveform: a typical extracellular spike recorded in the axonal region. There are four phases shown: (1) resting membrane potential; (2) depolarisation; (3) repolarisation; and (4) overshoot hyperpolarisation. Source: Intracellular spike from open source under Creative Commons license.

Intracellular recording is very challenging in the visual cortex and has only been mastered in a small number of laboratories worldwide (e.g. Ferster, 1986; Douglas & Martin, 1991; Henze et al., 2000; Priebe & Ferster, 2008; Long & Lee, 2012). Most importantly, recordings do not last for long periods, so it is hard to characterise RF properties in detail. As a result, a far more common approach to recording from visual cortex is to use extracellular recordings, which can be stable for many hours. Extracellular spike shapes are directly related to the changes in membrane potential observed during intracellular recording. However, the polarity of the waveform is reversed. That is, the classical four phases of the intracellular action potential are flipped (Figure 4.1) (Henze et al., 2000). There is a steady resting potential, a negative trough (corresponding to the depolarization intracellularly), a recovery to baseline or a positive peak and a final recovery to true baseline. Extracellular recordings suffer from more noise than intracellular signals because the signals are far smaller (e.g. cat V1: 50–200 μV; Gold et al., 2009), the extracellular electrodes are less optimal, and the signals are mixed with potentials from many neighbouring cells (Yunzab et al., 2019). Therefore, the extracellular waveforms are rarely as smooth as those that can be recorded intracellularly. Extracellular electrodes do not generally have the resolution to pick up sub-threshold post-synaptic potentials, while intracellular recordings can (Seong et al., 2014). Extracellular waveforms

often have an initial peak (1st peak; Figure 4.2B) before the large negative deflection. This 1st peak is thought to occur when recording from distal regions of the axon and is most likely the result of a mixed-ion capacitive current caused by slow NA+ channel activation (Gold et al., 2006).

Recent development of dense extracellular multi-electrode arrays (MEAs) has allowed simultaneous recordings of multiple neurons. This is made possible because there are multiple recording channels on every electrode array but also because multiple cells can now be recorded and recovered from single electrode channels (Sun, 2021). It is now common to record from the same neuron via several electrode channels. This improves the capacity to more carefully assess extracellular spike waveforms. As a consequence, the MEAs deliver a more detailed identification of extracellular spike waveform properties (Buzsáki, 2004). Several studies have also reported more non-traditional extracellular waveform shapes, e.g. positive spiking waveforms, which had been reported only rarely prior to the use of MEAs (Gold et al., 2006; 2009; Robbins et al., 2013; Gharat & Baker, 2017). In our laboratory, Sun (2019) identified five distinct classes of extracellular spike waveforms in cat V1 (Figure 4.2A): regular spiking (RS), fast spiking (FS), triphasic spiking (TS), compound spiking (CS), and positive spiking (PS). These spike waveform classes were identified based on five waveform features, as illustrated in Figure 4.2B. These features are: amplitude (red), peak-trough ratio (purple), end-slope (orange), duration (blue), and 1st peak-trough ratio (green). This classification method will be explained in detail in the Methods.

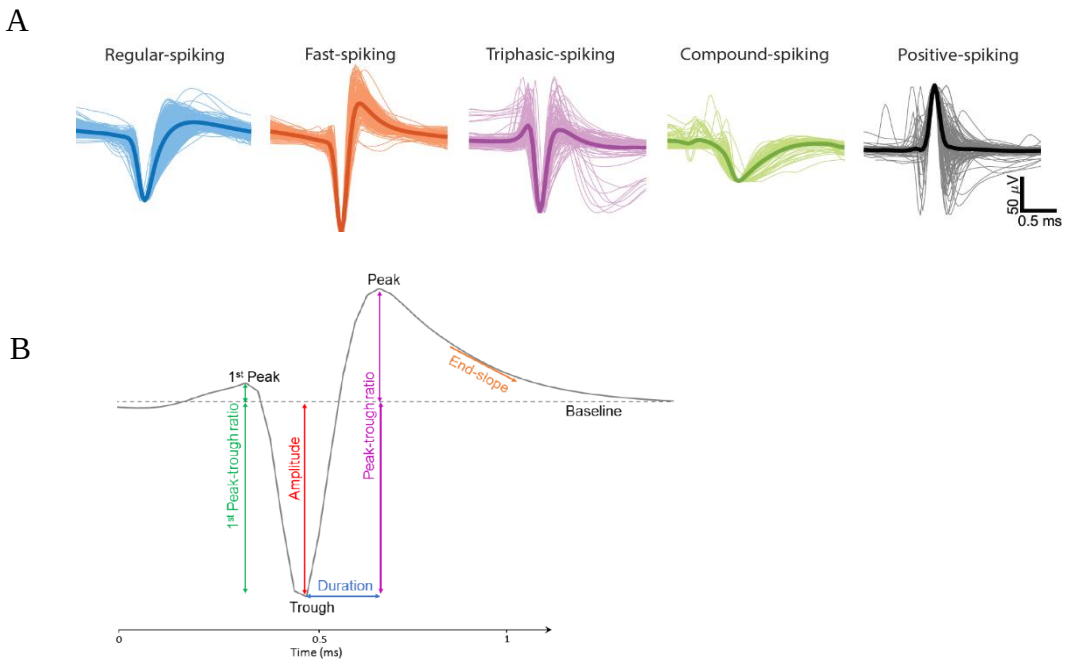

Figure 4.2 Classification of extracellular spike waveforms. **(A)** Five classes: regular spiking (RS), fast spiking (FS), triphasic spiking (TS), compound-spiking (CS) and positive spiking (PS). Further details of spike waveform classification are explained in the Methods. **(B)** An example spike waveform. The three peaks in this waveform include: the 1st peak, trough, and peak. The baseline is marked as a dotted line. Amplitude (in red) is the difference between the maximum peak (in this case trough) and the baseline. Peak-trough ratio (in purple) is the ratio between the amplitudes of the peak and the trough. 1st peak-trough ratio (in green) is the ratio between the amplitudes of the 1st peak and the trough. Duration (in blue) is the time period between the trough and the peak. End-slope (in orange) is the gradient calculated at 0.5 ms after the trough. Source: Sun (2019) Thesis Dissertation, University of Melbourne.

Commonly, the studies listed in the previous paragraph found that the amplitude of the trough, which is associated with intracellular depolarization, decreases with distance from the cell body (Figure 4.3). As the size of this negative deflection decreases, there is an increase in the amplitude of the 1st peak, which is thought to be linked to more distal recordings (Figure 4.3). Gold et al. (2006) argued that the 1st peak found in the distal axon likely results from a mixed-ion capacitive current caused by slow Na+ channel activation. Consistent with previous findings, Sun (2019) reported single units with positive-dominant spikes in cat V1. These positive spiking neurons have exceptionally large 1st peaks and small negative troughs. These recordings have been associated with the potentials that occur in axons or axon-terminals (Gold et al., 2009; Lewandowska et al., 2015). Sun and colleagues argued that positive-dominant waveforms may be recordings from LGN

afferents, as the single units with positive-dominant spikes had mostly non-oriented RFs, which are similar to the centre-surround RFs observed in the LGN.

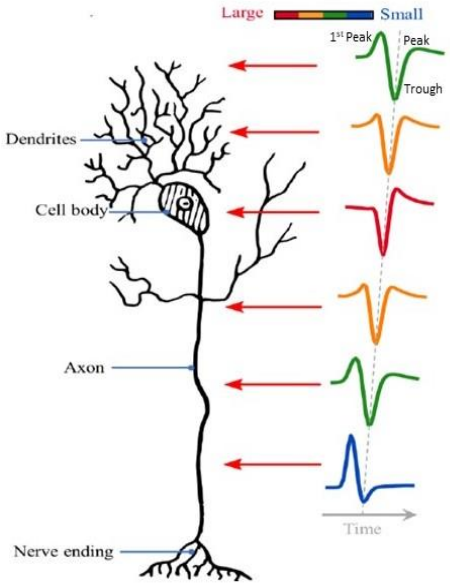

Figure 4.3 Schematic of a neuron illustrating that different spatial locations relative to the cell body can reflect different extracellular spike waveforms. The amplitude of the negative trough, associated with depolarization (represented in amplitude-dependent colour), decreases rapidly with distance from the cell body, and is associated with a relative increase of the 1st peak. Source: Sun (2019) Thesis Dissertation, University of Melbourne.

In this chapter, we will extract spike waveforms from all the single units recorded from the primary visual cortex (V1) of anaesthetised wallabies and subsequently categorise them on the basis of waveform shapes (following the same protocol as described by Sun, 2021). Second, we aim to correlate the extracellular waveform classes with their associated spatial receptive fields (RFs), estimated using the NIM (as described in Chapter 3). Based on extensive data from other species (mouse: Niell & Stryker, 2008; Yunzab et al., 2019; cat: Ferster, 1987; Shevelev et al., 1993; monkey: Tamura et al., 1996; Ringach et al., 2002), we hypothesise that the majority of RS and FS waveforms will have orientation-selective RFs. The data in Chapter 3 shows that LGN units in wallaby tend to be non-orientation selective. If the wallaby cortex proves to have similar characteristics to cat cortex, we might expect that positive-dominant waveforms in wallaby V1 will have non-selective RFs, resembling the RFs of the LGN units recorded from wallaby in Chapter 3. If

this is the case, it would suggest that the recordings from positive-spiking neurons in wallaby V1 are from the distal portions of LGN axons. By being able to correlate the RF properties of cortical neurons with particular spike waveforms with a high degree of certainty, we are potentially able to investigate the connectivity between brain areas with very fine resolution.

4.2 Methods

4.2.1 Waveform analysis

For 195 single units (SUs) described in the previous chapter (3.2), we collected 10,000 random spike waveforms for each SU from the raw data on the channel with the highest amplitude. These waveforms were extracted in the period between 1 ms before and 2 ms after the spike time (in a window of -30 to 60 samples, where 0 is the minimum trough). We used the maximum number of spikes for SUs with less than 10,000 spikes (< 10% of the total population). Collected spike waveforms were averaged, and the baseline was subtracted to make the new baseline equal to 0. The baseline was calculated as the mean of the first and last ten samples of the extracted waveform. Figure 4.2B shows a schematic diagram of example extracellular spike waveforms. The negative deflection in the extracellular spike waveform indicates the depolarization of the cell membrane, while the positive deflection reflects the hyperpolarization of the cell membrane. For each spike waveform, we measured five features: amplitude, peak-trough ratio, end-slope, duration, and 1st peak-trough ratio.

Amplitude

The amplitude was calculated as the signed difference between the maximum peak or the minimum trough and the baseline of the waveform (Figure 4.2B: red). The maximum peak was used when the magnitude was larger than the minimum trough, and if the minimum trough was larger than the maximum peak, the minimum trough was used. The spike waveform in Figure 4.2B has a minimum trough that is larger than the two positive peaks. Hence, the distance between the baseline and the minimum trough was used to calculate the amplitude.

Peak-trough ratio

The peak-trough ratio was calculated as the ratio between the unsigned amplitudes of the minimum trough and the following peak (Figure 4.2B: purple). The amplitude of the peak was divided by the amplitude of the minimum trough.

End-slope

The end-slope was calculated as the gradient of the slope at 0.5 ms after the minimum trough (Figure 4.2B: orange). The data was normalized using standard z-scores and clustered using k-means. Then, we calculated the sum of distances between cluster points to evaluate the separation of cluster groups. All spike waveforms were normalized to the smallest amplitude waveform before calculating the end-slope.

Duration

The duration was calculated as the time period from the minimum trough and the following peak (Figure 4.2B: blue).

1st Peak-trough ratio

The 1st peak-trough ratio was calculated as the ratio between the amplitude of the minimum trough and the previous peak (Figure 4.2B: green). The amplitude of the 1st peak was divided by the amplitude of the minimum trough.

Signal to noise ratio

The signal to noise ratio (SNR) was calculated as the ratio between the mean waveform and the standard deviation (SD) of waveform noise, as described by Kelly et al. (2007). The following equation describes how SNR was calculated for each spike waveform:

$$W = \begin{bmatrix} v^1(t_1) & v^1(t_2) & \cdots & v^1(t_n) \\ \vdots & \vdots & \ddots & \vdots \\ v^k(t_1) & v^k(t_2) & \cdots & v^k(t_n) \end{bmatrix},$$

$$\varepsilon = W - \begin{bmatrix} \bar{W} \\ \vdots \\ \bar{W} \end{bmatrix}, \tag{4.1}$$

$$SNR = \frac{\max(\bar{W}) - \min(\bar{W})}{2 \times SD_{\varepsilon}}$$

where W is the collection of k waveforms with n samples, $\overline{W}$ denotes the mean spike waveform, ε represents the matrix of noise values and SD_ε is the SD of all entries in ε.

4.2.2 Spiking properties

Spike rate

The spike rate of a single unit was determined by subtracting the spike rate during the stimulus offset (spontaneous activity) from the spike rate during the stimulus onset (response).

Response latency

The optimum response latency of a single unit was calculated from the post stimulus time histogram (PSTH). The PSTH was established from the stimulus onset (time = 0 ms) to the stimulus offset (time = 66.67 ms) and spikes were binned at 1/15 ms. The PSTH was smoothed by averaging over a sliding window of length 5 ms. Latency was determined as the point in time when the spike rate reaches 15% above the minimum ongoing spike rate inside 0-66.67 ms.

Burst index

The burst index was calculated as the ratio of burst frequency over the mean frequency for all spikes (i.e. nBurst/nAll). Spikes were defined as bursty when the inter-spike interval before the first spike was > 100 ms and when the subsequent spikes were within an inter-spike interval of < 4 ms. This burst index calculation is adapted from Wang et al. (2006).

4.2.3 Receptive Field

Receptive Field Estimation

The Nonlinear Input Model (NIM) was used to estimate receptive fields (RFs) for each SU as described in Chapter 3.

Receptive Field Categorisation

The spatial RFs uncovered from the previous chapter were categorised into two groups. The first included SUs with one or more RF filters that were oriented and elongated. The second included SUs with a single non-oriented RF filter. Refer to Chapter 3 for further details on how the RFs were categorised.

4.3 Results

4.3.1 Extracellular spike waveform classes

We recorded from 642 single units (SUs) in the primary visual cortex of six anesthetized wallabies. 195 of the SUs were driven by WGN and had their spatial RFs uncovered. The spatial RFs were estimated using the NIM, as described in the previous chapter. From the 642 SUs recorded, we identified five distinct waveform classes: regular spiking (RS), fast spiking (FS), triphasic spiking (TS), compound spiking (CS), and positive spiking (PS). Categorisation was conducted in a serial manner using a decision tree. First, SUs were classified as PS if they had any positive peak greater than their negative trough, while the remaining units were classified into negative spiking (NS) waveform types. Second, SUs were classified as TS if the magnitude of the 1st peak was 10% of the following negative trough. Third, TS units with particularly long waveforms (>1 ms) were further classified as CS units. Fourth, the remaining NS units were classified as RS and FS units using clustering techniques. The details on the classification of waveforms will be further discussed below. Figure 4.4 presents spike waveforms for all units from the five distinct waveform classes. From left to right presents RS (blue), FS (orange), TS (purple), CS (green) and PS (black). The dark line shows the mean spike waveform for each type of spike.

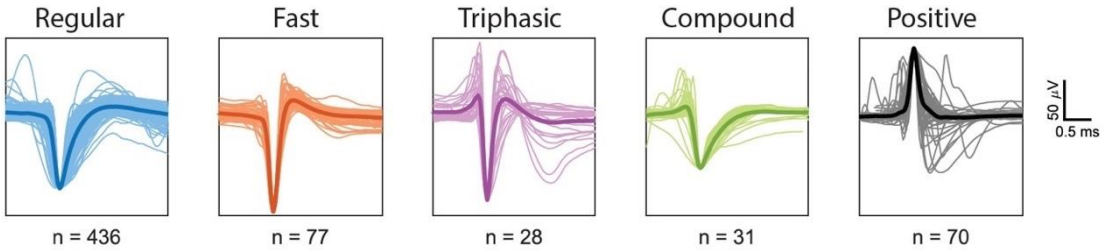

Figure 4.4 Classification of spike waveforms from all SUs. Regular spiking (RS, blue), fast spiking (FS, orange), triphasic spiking (TS, purple), compound spiking (CS, green) waveforms were normalized and aligned to the average minimum trough. Positive spiking (PS, black) waveforms were normalized and aligned to the average maximum peak. Dark lines within each waveform class represent the mean spike waveform. The X and Y axes for all units represent time (ms) and microvolts (μV), respectively. The spikes were collected in the timeframe between -1 ms to 1.5 ms. Scale bars represent 0.5 ms (horizontal) and 50 μV (vertical).

Regular and Fast spiking units

RS units and FS units had waveforms with a biphasic shape, with a strong negative trough followed by a smaller positive peak. First, RS and FS units were separated using end-slope and peak-trough ratio. We measured the end-slope of the waveform at 0.5 ms after the trough and plotted against the peak-trough ratio (i.e. ratio between normalized amplitude of the trough and the peak). RS and FS units were separated at an end-slope of zero (green line). We classified spikes with an ascending slope (end-slope > 0) as RS, and spikes with a descending slope (end-slope < 0) as FS units. There were no units with an end-slope of zero.

RS units had a significantly smaller trough-to-peak ratio when compared to FS units (mean ± SEM; RS: 0.13 ± 0.04, FS: 0.23 ± 0.03, t-test $p < 0.001$), which suggests that RS units have smaller positive phases following the negative trough than FS units. Furthermore, we measured trough-peak duration (Figure 4.5C and D), as described by Thiele et al. (2016), to confirm the separation of RS and FS units. The histogram shows the distribution of trough-peak duration for RS (blue) and FS (orange) units. FS units had trough-peak durations predominately < 0.5 ms (mean ± SEM = 0.28 ± 0.02 ms), while in RS units the ratio was > 0.6 ms (mean ± SEM = 0.74 ± 0.04 ms). We found that FS units had a significantly larger mean peak amplitude than that of the RS units (mean ± SEM: FS = 119 ± 8 μV, RS = 90 ± 4 μV, t-test, $p < 0.05$, Figure 4.6B).

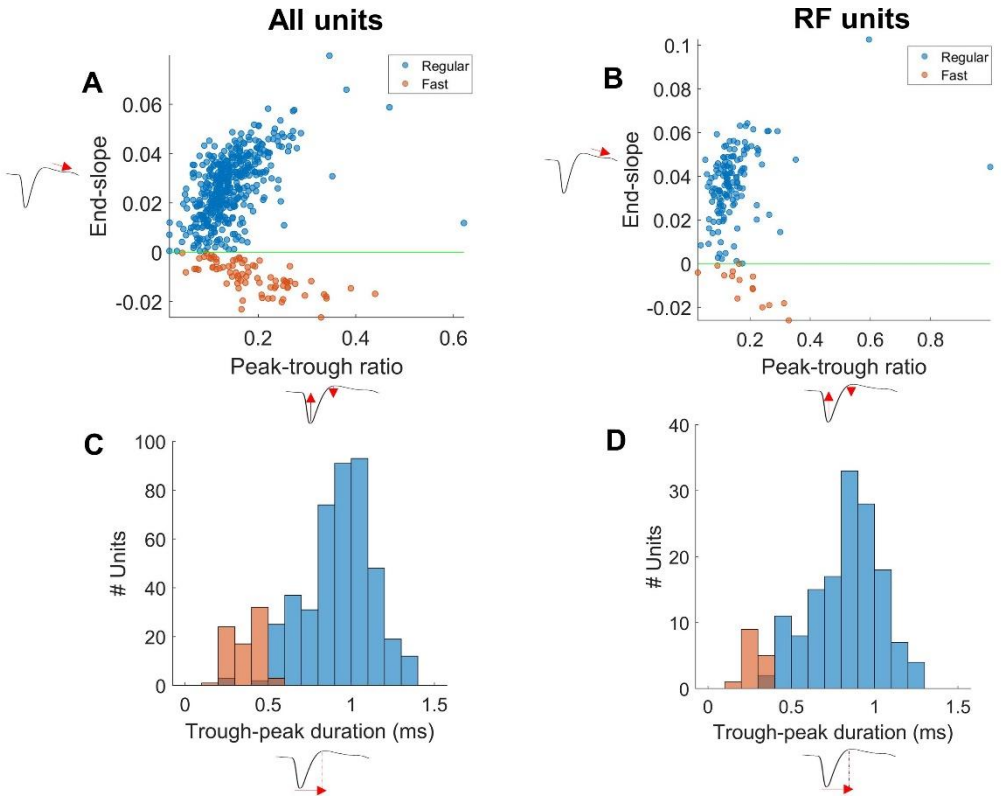

Figure 4.5 Separation of FS and RS units in wallaby V1. **(A–B)** Scatterplots of spike waveform shape parameters: end-slope and peak-trough ratio used to separate RS (blue) and FS (orange) units from **(A)** all units and **(B)** units with RFs. RS (blue) and FS (orange) units were separated using an end-slope = 0 (green-line). The x and y axes denote peak-trough ratio and end-slope, respectively. **(C–D)** Histogram plots of the trough-peak duration (ms): RS (blue) and FS (orange) units from **(C)** all units and (**D)** units with RFs. Bins are in 0.1ms.

Triphasic spiking units

TS units had waveforms with 1st peaks > 10% of the minimum trough, which was followed by a large negative trough and subsequently a small positive peak. The mean initial positive peak from the TS units was 31 μV (30% of minimum trough), which created a distinct triphasic shape, different to those of the RS and FS units. If we exclude the initial peak component of TS units, the waveforms looked very much like FS units in terms of trough-to-peak ratio (mean ± SEM: 0.32 ± 0.05) and trough-peak duration (mean ± SEM: 0.43 ± 0.06 ms). The mean peak amplitude for TS units (mean ± SEM: 104 ± 14 μV, Figure 4.6B) was similar to that of RS and FS units.

Compound spiking units

CS units had waveforms with distinct triphasic shapes, with an initial positive peak, which was followed by a negative trough and a small positive peak. The CS units were separated from TS by their significantly longer waveforms, which we quantified by measuring the peak-to-peak time (mean peak-to-peak time ± SEM: CS = 1.4 ± 0.07 ms, TS = 0.45 ± 0.06 ms, t-test, $p < 0.01$). Of all the waveform classes, CS units had the smallest mean peak amplitude (mean ± SEM: 36 ± 6 μV, Figure 4.6B), smallest trough-to-peak ratio (mean ± SEM: 0.12 ± 0.04), and longest trough-peak duration (mean ± SEM: 1.0 ± 0.04 ms).

Positive spiking units

PS units had waveforms with a maximum peak larger than the minimum trough. Figure 4.6A presents a histogram of the distribution of peak amplitudes for all SUs. The red line (amplitude = 0) is the boundary that separates negative spikes (amplitude < 0) from positive spikes (amplitude > 0). The mean peak amplitude of PS units is 84 ± 5 μV (mean ± SEM, Figure 4.6B), while the mean peak amplitude of all the negative spikes is 95 ± 10 μV (mean ± SEM, Figure 4.6B).

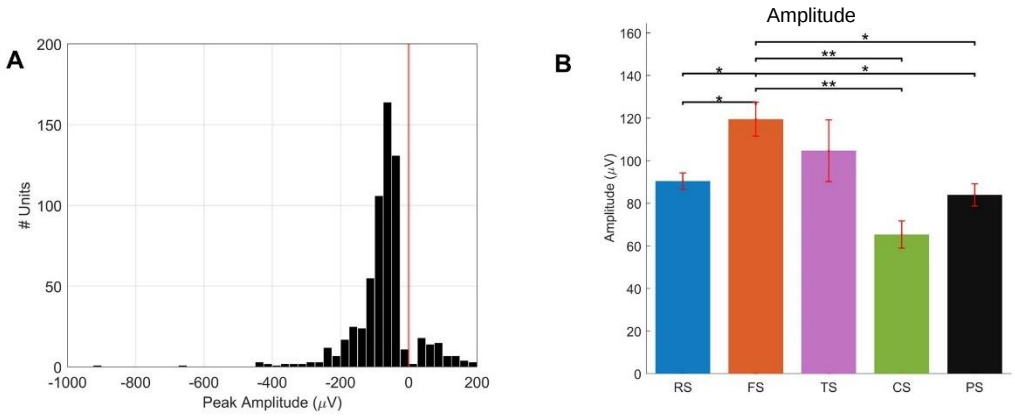

Figure 4.6 Peak spike amplitudes. **(A)** Histogram of the distribution of recorded peak amplitudes in 24 μV bins. Red lines represent amplitude = 0, where the negative spikes (amplitude < 0) were separated from positive spikes (amplitude > 0). The mean amplitude from all negative spikes is -95 ± 10 μV (mean ± SEM) and, for positive spikes, the mean amplitude is 84 ± 5 μV (mean ± SEM). **(B)** Bar plot showing absolute mean amplitudes of all units for each waveform class: RS (blue, 90 ± 4 μV), FS (orange, 119 ± 8 μV), TS (purple, 104 ± 14 μV), CS (green, 36 ± 6 μV), and PS (black, 84 ± 5 μV) units. SEM is represented by red error bars. * and ** represent $p < 0.05$ and $p < 0.01$ (t-test), respectively.

Signal to noise

For each spike waveform, we measured the signal to noise ratio (SNR) by calculating the ratio between the mean waveform and the SD of the waveform noise, as described previously by Kelly et al. (2007). Figure 4.7 presents the SNR of all the spike waveform classes to compare the level of spike signal to the level of background noise. Of all the waveform classes, FS units had the highest SNR (mean ± SEM, 1.70 ± 0.12 μV; t-test, $p < 0.01$). The remaining waveform classes: RS, TS, and PS units had similar SNRs (mean ± SEM, RS = 1.23 ± 0.03 μV, TS =1.57 ± 0.20 μV, CS =1.18 ± 0.14 μV, PS = 1.26 ± 0.07 μV).

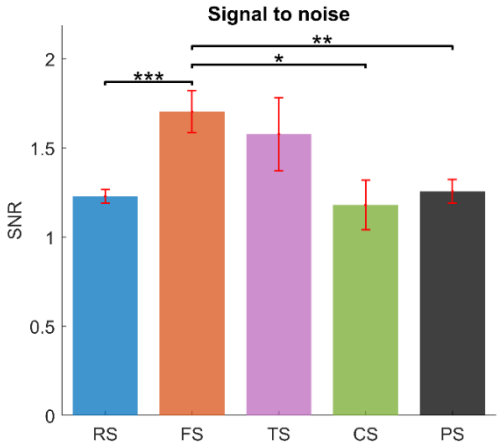

Figure 4.7 Signal to noise ratios from each waveform class: RS (blue, 1.23 ± 0.03 μV), FS (orange, 1.70 ± 0.12 μV), TS (purple, 1.57 ± 0.20 μV), CS (green, 1.18 ± 0.14 μV), and PS (black, 1.26 ± 0.07 μV) units. SEM is represented by red error bars. *, **, and *** represent $p < 0.05$, $p < 0.01$, $p < 0.001$ (t-test), respectively.

4.3.2 Population

Figure 4.8A presents a summary of the distribution of spike waveform types identified from all SUs recorded. The population was dominated by RS (n = 436, 68%) and FS units (n = 77, 12%). The ratio of RS units and FS units (68/12 = 5.7) identified in our SU population is higher than findings in previous extracellular studies in other species (2.2 for cat: Chen et al., 2007; 4.1 for mouse: Niell & Stryker, 2008). The PS units (n = 70, 11%) were found to be the next largest group, though they formed a slightly lower proportion than those recorded in cat visual cortex (14%: Sun, 2021). Lastly, TS and CS units (n = 28, 4%; n = 31, 5%) were found in the lowest proportions in the population of SUs.

We also classified spike waveforms from the population of SUs with RFs (Figure 4.8B). The distribution of spike waveforms in the population of SUs with RFs was very similar to that in the population for all units. Of the 194 SUs, RS (n = 132, 68%) units were identified as the largest group, followed by the FS units (n = 27, 14%). The ratio of RS units to FS units (132/27 = 4.9) was similar to that of the population for all units. The remaining waveform classes were all identified below 10% of the total population: TS units (n= 11, 6%), CS units (n = 7, 4%) and PS units (n = 17, 9%).

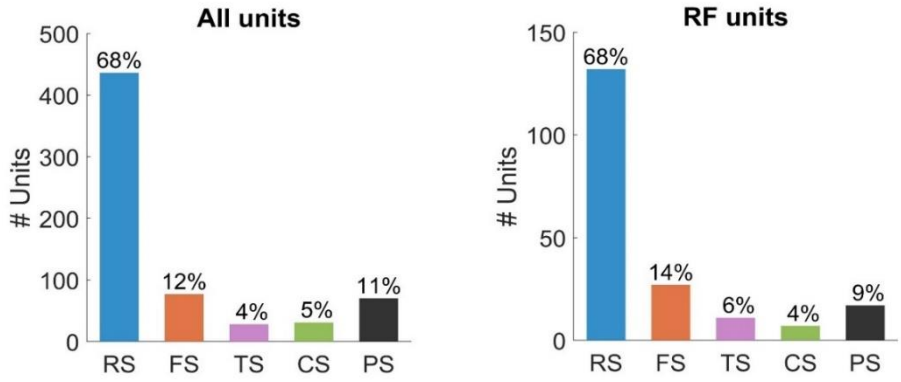

Figure 4.8 Population statistics for **(A)** all units and **(B)** units with RFs. Bars represent the number of units within each waveform class: RS (all units n = 436, RF units n = 132), FS (all units n = 77, RF units n = 27), TS (all units n = 28, RF units n = 11), CS (all units n = 31, RF units n = 7), PS (all units n = 70, RF units n = 17). The percentages of each subpopulation are presented above the bars.

4.3.3 Correlating spike waveforms with receptive field structure

Spike waveforms and RF types

In the previous chapter, we classified RFs into three types: single RFs, multiple RFs, and non-oriented RFs. In this chapter, we classified spike waveforms into five classes: RS, FS, CS, and PS waveforms. We wanted to find out if there was any correlation between spike waveform classes and receptive field types. Figure 4.9 plots the proportion of the three RF types (single RF = blue; multiple RF = light blue; non-oriented RF = yellow) for each spike waveform type. The numbers above each bar represent the actual unit counts. Most waveform types including RS, FS, TS, and CS have predominately orientation-selective RFs (RS: 42% single RFs, 37%

multiple RFs, and 21% non-oriented RFs; FS: 43% single RFs, 29% multiple RFs, and 28% non-oriented RFs; TS: 46% single RFs, 27% multiple RFs, and 27% non-oriented RFs; CS: 43% single RFs, 43% multiple RFs, and 14% non-oriented RFs). Overall, single RFs are found more than multiple RFs in all waveform types, with the exception of CS spikes where single and multiple RFs are evenly distributed. In contrast, PS units contain a relatively even distribution of oriented and non-oriented single RFs, showing the highest portion of non-oriented RFs of all the waveform classes (PS: 53% oriented RFs and 47% non-oriented RFs).

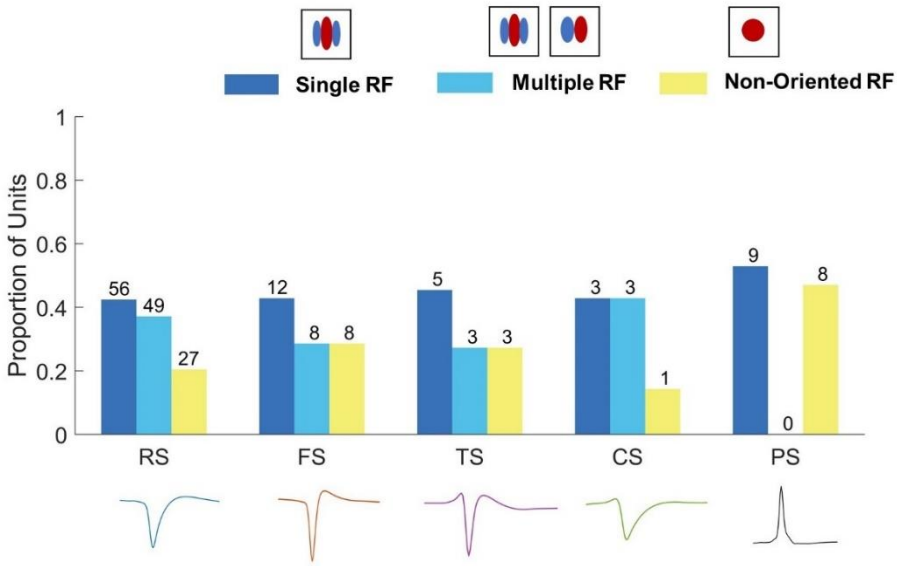

Figure 4.9 Correlating spike waveform classes to their receptive field types. The legend above shows the RF types: single RF (blue; # Filter = 1; OB > 2.0), multiple RF (light blue; # Filter >1; OB > 2.0), and non-oriented RF (yellow; OB < 2.0). RS units include 42% single RF (n = 56); 37% multiple RF (n = 59); 21% non-oriented RF (n = 27). FS units include 42% single RF (n = 12); 29% multiple RF (n = 8); 29% non-oriented RF (n = 8). TS units include 46% single RF (n = 5); 27% multiple RF (n = 3); 27% non-oriented RF (n = 3). CS units include 43% single RF (n = 3); 43% multiple RF (n = 3); 14% non-oriented RF (n = 1). PS units include 53% single RF (n = 9); 0% multiple RF (n = 0); 47% non-oriented RF (n = 8).

Spike waveforms and oriented/non-oriented RF types

We classified SUs into oriented and non-oriented RF types using the OB index calculated from neuronal responses to WGN. Figure 4.10 presents the proportion of oriented (blue) and non-oriented (yellow) RF units for each spike waveform type. The results from RFs derived from drifting gratings were similar to the results we found from RFs uncovered from NIM (Figure 4.9). RS and FS units are mainly

orientation-selective RFs (RS: 67% oriented RF and 33% non-oriented RF; FS: 71% oriented RF and 29% non-oriented RF). TS and CS units contain well-balanced portions of oriented and non-oriented units (TS: 55% oriented RFs and 45% non-oriented RFs; CS: 57% oriented RFs and 43% non-oriented RFs). Conversely, PS units have more non-oriented RFs than oriented RFs (PS: 41% oriented RFs and 59% non-oriented RFs).

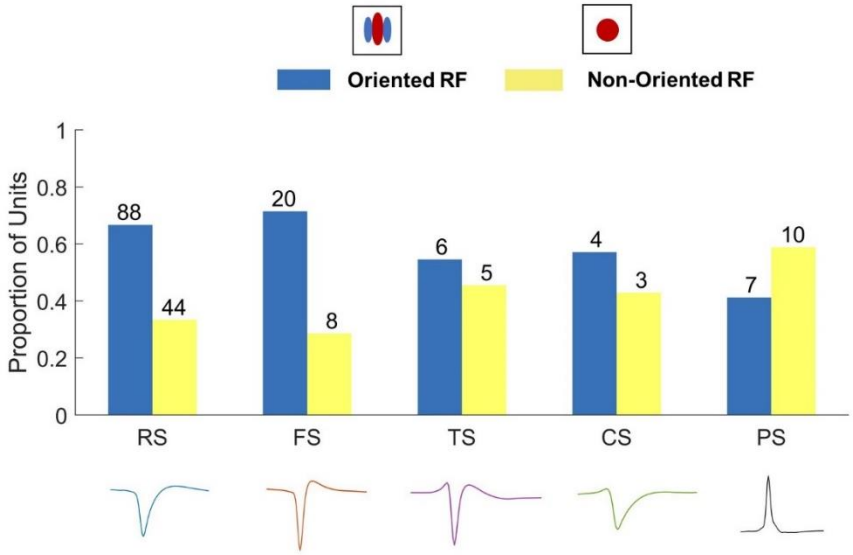

Figure 4.10 Correlating spike waveform classes to oriented and non-oriented RFs. The legend above shows the RF types: oriented RF (blue) and non-oriented RF (yellow). RS and FS units are predominately oriented (RS: 67% oriented RF, n = 88; 33% non-oriented RF, n = 44; FS: 71% oriented RF, n = 20; 29% non-oriented RF, n = 8). TS, CS and PS units have similar proportions of oriented RFs and non-oriented RFs (TS: 55% oriented RF, n = 6; 45% non-oriented RF, n = 5; CS: 57% oriented RF, n = 4; 42% non-oriented RF, n = 3; PS: 41% oriented RF, n = 7; 59% non-oriented RF, n =10).

Spike waveforms and nonlinearities

In the previous chapter, we characterised nonlinearities in RF units based on three measures: F1/F0 ratio, symmetry index (SI), and number of spatial filters (nFilter). Figure 4.11A–C presents all three measures of nonlinearities from each waveform type. RF units are characterised as either linear (blue: F1/F0 > 1; SI < 0; nFilter = 1) or nonlinear (light blue: F1/F0 < 1; SI > 0; nFilter > 1). Figure 4.11A indicates that RS and FS units are predominately complex RF units (RS: 67% simple RFs and 33% complex RFs; FS: 79% simple RFs and 21% complex RFs). The nonlinear characteristic of RS and FS units are supported in Figure 4.11B, which shows that the majority of RS and FS units have positive SIs (RS: 12% linear RFs and 88%

nonlinear RFs; FS:11% linear RFs and 89% nonlinear RFs). Figure 4.11C suggests that the distribution of RF units with single and multiple filters occurs in similar proportions for both RS and FS waveform classes (RS: 51% single filter and 49% multiple filter; FS: 54% single filter and 46% multiple filter).

TS and CS units contain similar portions of simple and complex RFs (TS: 55% simple RFs and 45% complex RFs; CS: 43% simple RFs and 57% complex RFs, Figure 4.11A). These units are also largely nonlinear (TS: 36% linear RFs and 64% nonlinear RFs; CS:14% linear and 86% nonlinear, Figure 4.11B) and have greater proportions of RF units with single filters (TS: 73% single filter and 27% multiple filter; CS: 57% single filter and 43% multiple filter, Figure 4.11C). On the other hand, PS units are largely simple RF units (PS: 65% simple RFs and 35% complex RFs). Despite the high proportion of simple RFs amongst the PS units, 64% of these units have positive symmetry indices (nonlinear). 94% of PS units have a single spatial filter. (Figure 4.11C).

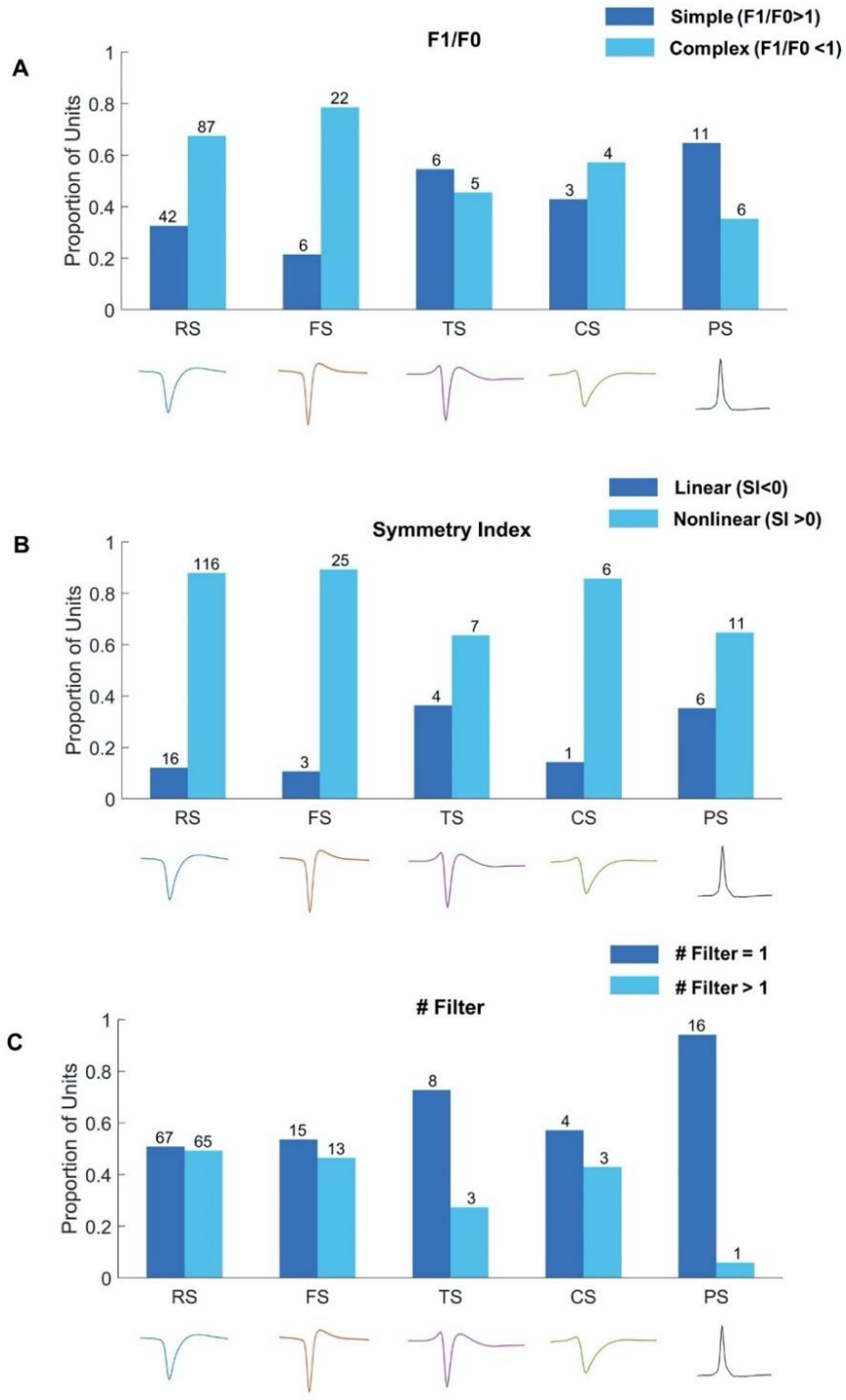

Figure 4.11 Correlating spike waveform classes to three measures of nonlinearities in RF units. **(A)** Bar plots showing the proportion of simple (blue; F1/F0 > 0) and complex (light blue; F1/F0 < 0) units for each waveform type. RS and FS units are predominately complex units (RS: 33% simple RF, n = 44; 67% complex RF, n = 86; FS: 21% simple RF, n = 6; 79% complex RF, n = 22). TS and CS units have a similar proportion of simple and complex RFs (TS: 55% simple RF, n = 6, 45% complex RF, n = 5; CS: 43% simple RF, n = 3, 57% complex RF, n = 4). PS units are dominated by simple RF (PS: 65% simple RF, n = 11; 35% complex RF, n = 6). **(B)** Bar plots showing the proportion of linear (blue; SI < 0) and nonlinear (light blue; SI > 0) units for each waveform type. All waveforms: RS, FS, TS, CS and PS units have larger portions of linear RF filters (RS:

12% linear RF, n =16 , 88% FS:11% linear RF, n = 3; 89% nonlinear RF, n = 25; TS: 36% linear RF, n = 4, 64% nonlinear RF, n = 7; CS:14% linear, n = 1, 86% nonlinear, n = 6; PS: 35% linear, n = 6, 65% nonlinear RF, n = 11). **(C)** Bar plots showing the proportion of single filter (blue; # filter = 1) and multiple filter (light blue; # filter > 1) units for each waveform type. RS, FS, and CS units have similar proportions of single and multiple filter units (RS: 51% single filter, n =67, 49% multiple filter, n = 65; FS: 54% single filter, n = 15; 46% multiple filter, n = 13; CS: 57% single filter, n = 4, 43% multiple filter, n = 3). TS and PS units are dominated by single filters (TS: 73% single filter, n =8, 27% multiple filter, n= 3; PS: 94% single filter, n = 16, 6% multiple filter, n = 1).

4.3.4 Spiking characteristics

For each waveform class, several spiking characteristics were examined, i.e. spike rate, burst index, and response latency (Figure 4.12A–C). These spiking characteristics were chosen to distinguish spike waveforms that are from cortical and thalamic cells. In this section, we only analyse the population of SUs with characterised RFs.

Spike rate

Figure 4.12A presents the average spike rate in response to WGN from each waveform class. PS units had the lowest average spike rate of all waveform classes (mean ± SEM: 1.36 ± 0.35 spks/sec). Their spike rates were significantly lower than RS (mean ± SEM: 2.84 ± 0.27 spks/sec, t-test: $p < 0.01$) and CS units (mean ± SEM: 3.20 ± 2.03 spks/sec, t-test: $p < 0.01$), but not significantly lower than TS (mean ± SEM: 2.18 ± 1.17 spks/sec, t-test: $p = 0.1$) and CS units (mean ± SEM: 3.20 ± 2.03 spks/sec, t-test: $p = 0.1$).

Response latency

Figure 4.12B presents the latency (i.e. the average time required to respond to the stimulus onset) for each waveform class. Latency for each SU was calculated from the PSTH (as described in the Methods). PS units had the shortest latency (mean ± SEM; 25 ± 2.7 msec), which was significantly shorter than RS (mean ± SEM; 39 ± 1.1 msec, t-test: $p < 0.001$) and FS units (mean ± SEM; 36 ± 2.1 msec, t-test: $p < 0.05$). Short latencies are usually associated with the thalamic input in the cat cortex, as they respond to visual input earlier than the cortical cells (Reid & Alonso, 1995; Usrey et al., 2000; Alonso et al., 2001).

Burst index

The burst index is indicative of how short the time interval is between the spikes. Thalamic cells are known to spike in bursts more often as compared to cortical cells (Guido & Weyand, 1995; Ramcharan et al., 2000). The burst index ranges from 0 to 1, representing low to high burst, respectively. Figure 4.12C presents the average burst index (i.e. the ratio of burst spikes over all spikes) for each waveform class. PS units had the highest proportion of bursting spikes (mean ± SEM: 0.13 ± 0.01), which were significantly higher than RS (mean ± SEM: 0.07 ± 0.01, t-test: $p < 0.01$) and FS units (mean ± SEM: 0.06 ± 0.01, t-test: $p < 0.01$) and not significantly higher than TS (mean ± SEM: 0.09 ± 0.03, t-test: $p = 0.08$) and CS units (mean ± SEM: 0.12 ± 0.03, t-test: $p = 0.1$).

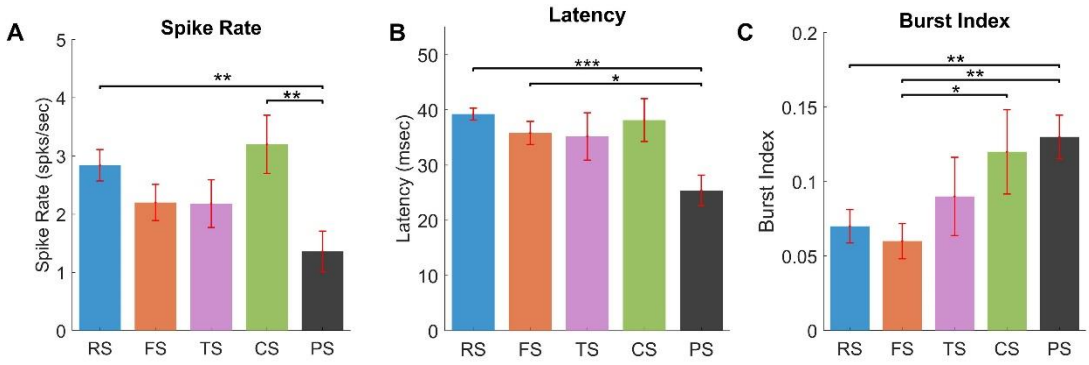

Figure 4.12 Bar plots showing spiking characteristics of all units for each waveform class. **(A)** Mean spike rate of units with measured RFs: RS (blue, mean ± SEM: 2.84 ± 0.27 spks/sec), FS (orange, mean ± SEM: 2.20 ± 0.32 spks/sec), TS (purple, mean ± SEM: 2.18 ± 1.17 spks/sec), CS (green, mean ± SEM: 3.20 ± 2.03 spks/sec), and PS (black, mean ± SEM: 1.36 ± 0.35 spks/sec) units. **(B)** Mean latency, calculated by setting a 15% threshold from baseline to peak of the unit's corresponding PSTH: RS (blue, mean ± SEM: 39 ± 1.1 msec), FS (orange, mean ± SEM: 36 ± 2.1 msec), TS (purple, mean ± SEM: 35 ± 4.3 msec), CS (green, mean ± SEM: 38 ± 3.9 msec), and PS (black, mean ± SEM: 25 ± 2.7 msec) units. (C) Mean burst index, i.e. ratio between burst spikes and all spikes: RS (blue, mean ± SEM: 0.07 ± 0.01), FS (orange, mean ± SEM: 0.06 ± 0.01), TS (purple, mean ± SEM: 0.09 ± 0.03), CS (green, mean ± SEM: 0.12 ± 0.03), and PS (black, mean ± SEM: 0.13 ± 0.01) units. SEM is represented by red error bars. *, **, and *** represent $p < 0.05$, $p < 0.01$, $p < 0.001$ (t-test), respectively.

4.4 Discussion

We categorised spikes into five extracellular waveform classes: regular-spiking (RS), fast-spiking (FS), triphasic-spiking (TS), compound-spiking (CS), and positive-spiking (PS). As described in the previous chapter, RFs were estimated using white Gaussian noise (WGN) with the nonlinear input model (NIM) and categorised into oriented RFs (single-filter, multi-filter) and non-oriented RFs. In the following, I will discuss the biophysical properties and origin of each spike waveform class identified in this study and compare these to the results of previous studies.

4.4.1 Biophysics of extracellular spike waveform classes

In RS and FS waveforms, the negative trough followed by a positive peak is established by the opening and closing of Na+ and K+ channels, respectively (Henze et al., 2000). The dominant negative troughs observed in wallaby RS and FS waveforms provide compelling evidence that the recordings were made close to somas (Gold et al., 2006). In our study we separated RS and FS units based on the difference in spike durations. In rodents this difference has been understood to be the result of the difference in the level of expressions of Na+ and K+ channels (Martina & Jonas, 1997; Martina et al., 1998) ; the spike duration in FS waveforms is shorter due to the faster repolarisations of Kv1 and Kv3 channels. Additionally, broad spike waveforms have been observed in pyramidal and spiny stellate neurons (i.e. excitatory neurons), whereas narrow spike waveforms have been observed in basket and chandelier interneurons (i.e. GABAergic inhibitory neurons) in rodent and cat V1 (Barthó et al., 2004; Trainito et al., 2019). However, it should be noted that the classification of RS and FS spike waveforms based on spike duration may not be flawless: recent studies in monkey cortex observed pyramidal cells with narrow-waveform spikes (Ichinohe et al., 2004; Constantinople et al., 2009; Vigneswaran et al., 2011; Onorato et al., 2020). However, this is the only such report, so its general significance relative to the huge bodies of work showing the alternate case should be noted.

In contrast to RS and FS waveforms, TS, CS and PS waveforms were found with a dominant 1st peak (Figure 4.4), which is most likely due to a mixed-ion capacitive current that increases in amplitude as the recording site increases in distance from the soma (Gold et al., 2006), either in the dendritic spikes (Gur et al., 1999; Henze et al., 2000; Jia et al., 2019; Gold et al., 2009) or in the axonal spikes (Raastad & Shepherd, 2003; Blanche et al., 2005; Lewandowska et al., 2015). This phenomenon is consistent with models of current sources and sinks from extracellular spikes that propagate through an isolated axon, most likely due to differences in morphology and ion channels (Barry, 2015).

The slow and small spikes associated with CS waveforms are most likely due to the large distance between the recording site and the soma and the consequent contribution of distal sources to the generation of the action potentials (Gold et al., 2006). In our cell population, we did not find any PS waveforms that exceeded 100 μV, which is consistent with Sun's (2019) findings in cat V1. However, this is in contrast to Gold et al's (2009) study in cat cortex that recorded larger extracellular positive spikes (> 500 μV) with orientation selective RFs, which they named high-amplitude positive spikes (HAPS). Gold et al. (2009) believe that the HAPS may be recordings from the somas of large L5 pyramidal neurons undergoing distal dendritic initiation. The amplitude of any spike increases with the size of the soma and apical trunk, which might explain the large positive spikes of the HAPS (Gold et al., 2009). A possible explanation for the absence of HAPS in our data is that our recording sites did not reach L5 pyramidal neurons in wallaby V1, as most of our recordings were made in the supragranular or granular layers (i.e. layers 1–4).

4.4.2 Predictions on the origin of each spike class

Due to the low numbers of single units that had TS and CS waveforms (6% and 4%), it is difficult to draw strong conclusions on where their somas originate, but it is likely that TS and CS units are recordings from a mixture of cells with local cortical- or thalamic origin. This is because they have relatively even proportions of oriented and non-oriented RFs, which is consistent with what has been reported in cat cortex (Sun, 2021) and have a higher proportion of burst responses to RS/FS waveforms. It is possible that TS and CS waveforms are of the same spike class, as

they have similar proportions of RF type and spiking characteristics. We have left them as separate classes due to the unusual shape, low amplitude, and slow waveforms of CS units. This CS waveform has only recently been observed in cat cortex (Sun, 2021). As mentioned above, the modern sampling methods, i.e. MEAs and spike-sorting algorithms may have led to the extraction of these low amplitude spikes.

It is possible that PS waveforms are recordings of axons originating from the thalamus, as was proposed in cat cortex (Sun, 2021). It is noteworthy that some 60% of PS unit RFs in wallabies were not orientation selective. As LGN cells are non-oriented in wallaby and cat (Hubel & Wiesel, 1961; Vidyasagar & Heide, 1984) and positive spikes have been associated with recordings from distal axons (Bakkum et al., 2013; Pan et al., 2013; Lewandowska et al., 2015; Sun, 2021). There is a possibility that a high proportion the wallaby PS units are recordings from axons or axon afferents from the LGN. A recent study looked at this possibility in cat cortex and found that 80% of PS units in that species have non-oriented RFs, which is a notably higher percentage than in the wallaby data (Sun, 2021). However, it is also possible that the non-oriented PS unit RFs could be from V1 afferents targeting the geniculate.

If the PS units in wallaby are LGN axons or axon afferents, why is it that only slightly more than half have non-oriented RFs? One explanation might be that orientation selectivity is more developed in wallaby LGN than in cat LGN (as discussed in the previous chapter). Previous studies in cats defined non-oriented LGN cells as those that have an Orientation Bias Index < 0.2 (Rosenberg et al., 2010; Gharat & Baker, 2017). In the analysis of LGN units in Chapter 3, I showed that 70% had OBs < 0.2 but this means that 30% of the LGN cell population had OBs > 0.2, suggesting that some LGN cells in wallabies exhibit some degree of orientation selectivity. Consistent with our findings, Gur et al. (1999) recorded small-amplitude positive spikes that were slightly less tuned to orientation than the negative spikes, but more selective to orientation than LGN cells in macaque V1. In their analysis of monkey cortex, they hypothesized that the small-amplitude positive spikes represented an intermediate processing stage in the evolution of orientation selectivity within the visual hierarchy. Unfortunately, I had to terminate

my LGN recordings from the wallaby due to COVID-19. Nonetheless, from the twelve recordings, most cells showed either non-oriented or only mildly oriented RFs. The mild orientation biases of some LGN units might represent the early stages of orientation selectivity in wallaby LGN, and this might explain why many PS units had orientation selectivity, even if they were LGN axons. Alternative to the classic convergence model of Hubel and Wiesel (1962), several studies have proposed that orientation selectivity in V1 emerges from the sharpening of orientation-biased LGN inputs (Vidyasagar & Sigüenza, 1985; Xu et al., 2002; Kuhlmann & Vidyasagar, 2011). Kuhlmann and Vidyasagar (2011) proposed that simple cells might receive excitatory input from orientation-biased LGN cells and inhibitory input from non-oriented LGN cells. They suggest orientation selectivity may be driven by the interaction between excitatory and inhibitory inputs from the LGN cells, combined with recurrent cortical excitation and inhibition. Such a scheme is a possibility in the wallaby but far more LGN data is required before conclusions can be drawn.

While the existence of orientation selectivity in many wallaby PS units could be used to argue against them being LGN axons, two factors point strongly towards them being LGN axons. The spiking characteristics of PS waveforms were similar to thalamic cells for two reasons. First, they had shorter response latencies than other cortical recordings (PS units: 25 ms; RS and FS units: respectively, 39 ms and 36 ms), which is expected for cells earlier in the visual pathway (Bair et al., 2002; Kara et al., 2002; Jin et al., 2011; Takemura et al., 2020). This is also consistent with the short latency observed in our twelve LGN cells (27 msec ± 2 msec; see Chapter 3). Second, the PS units had a higher proportion of burst responses than other cell types. In many species, LGN units have been found to have far greater burstiness than V1 units (Weyand et al., 2001; Bezdudnaya et al., 2006; Ruiz et al., 2006). This is consistent with what has been reported in cats, where the PS units had the highest burst responses of all spikes recorded in V1 (Sun, 2021). However, an unusual feature of the PS units in wallabies was their low spike rates. In cats, the PS units were reported to have the highest spike rates of all spike types in V1 (Sun, 2021). In other species that have been studied, LGN units tend to have high spikes rates (monkey: Martinez-Conde et al., 2002; cat: Yeh et al., 2003; mouse: Alitto & Usrey, 2005; mouse: Durand et al., 2016; marmosets: Pietersen et

al., 2017). From the data in Chapter 3, I showed that wallaby LGN spike rates were on average 2.2 spks/sec, which is relatively low compared to what has been reported in cats (~5 spks/sec; Yeh et al., 2003) or in monkeys (~10 spks/sec; Martinez-Conde et al., 2002). Hence, this correlates with the low spike rates observed in the PS units in wallaby V1. It appears based on the recordings from LGN and from PS units in wallabies that they have somewhat lower spike rates than LGN units in other species. This is very interesting and deserves further comprehensive analysis.

In addition to similarities in spiking characteristics between PS units and LGN units in cat, Sun (2019) found strong evidence through muscimol experiments that PS waveforms are axons originating outside V1. Muscimol silences the cortex by specifically binding to GABA receptors in the dendrites of cortical cells for which any unit that is unaffected by muscimol is likely to originate outside the cortex. Sun (2019) recorded from cat V1 before and after the application of muscimol in V1 area and found that PS units remained active while RS and FS cells did not. This method confirmed that the PS waveforms are not from V1, but rather originate from outside V1. However, it is also possible that PS waveforms are from long-range cortico-cortical connectivity from higher visual cortical areas. Nonetheless, muscimol increases acetylcholine (ACh) and there is also evidence that suggests Ach increases inhibitory strength in cat, which might potentially modulate geniculosriate waveforms (Erisir et al., 2001; Disney et al., 2012). It would be interesting to conduct the same muscimol experiment for the wallaby and see if the PS units remain after the cortical silencing, however, such an extensive experimental protocol was beyond the scope of this thesis.

In our study, we also show that a high proportion of PS units with recovered RFs were characterised as having linear summation properties, using the F1/F0 ratio (PS = 65% simple units) and by consideration of the number of spatial filters (PS = 94% single-filter). This finding matches the data from Chapter 3, where all twelve LGN cells showed linear summation characteristics, as expected if their inputs from retina and LGN were from X-like cells (Enroth-Cugell & Robson, 1966; Kaplan & Shapley, 1982). The linear properties of PS units were also observed in high proportion in cat V1, which was explained by the X cells in the LGN projecting almost exclusively to Area 17 (primary visual cortex) (Sun, 2021).

One measure contradicts the linear properties seen in our PS units, and that is the symmetry index of the NIM input nonlinearities, which showed that 63% of PS units were nonlinear. It is possible that some of our PS units may have been recordings from local cortical interneurons. One possibility is that these cells received inputs from opposing X-cells (i.e. one excitatory and one inhibitory), which would influence the linearity of the PS units. At this point, it is not possible to arrive at a strong conclusion about one type of RGCs dominating the input to the wallaby's LGN based on the small sample size. However, with the easing of COVID-19 restrictions, we plan to conduct more LGN experiments to increase the size of the wallaby LGN cell population.

In this study, we show high proportions of RS and FS units (RS = 68% and FS = 12%), which, based on extensive prior work, likely correspond to excitatory (i.e. pyramidal) and inhibitory (i.e. basket and chandelier) cortical cells, respectively (Barthó et al., 2004; Mitchell et al., 2007; Niell & Stryker, 2008; Mruczek & Sheinberg, 2012). This is also consistent with recent reports in cat V1, where RS and FS units comprised 72% of the overall cortical cell population (Sun, 2021). However, it is interesting that the ratio of RS to FS waveforms in wallabies (RS/FS = 5.7) is much higher than what has been reported in other extracellular studies (cat: RS/FS = 2.2; Chen et al., 2007; mouse: RS/FS = 4.1; Niell & Stryker, 2008). There is a possibility that we have an over-representation of recordings from layer 5 (L5), where medium and large pyramidal cells are abundant. However, this contradicts the earlier assertion in Section 4.4.1 above that the lack of recordings from HAPS is because we recorded mainly in layer 1–4. This contradiction is impossible to resolve based on existing data.

The large over-representation of RS units in our wallaby recordings raises a more significant limitation associated with using extracellular spike waveforms to separate inhibitory and excitatory cells. It has been previously reported that some inhibitory cells display regular spiking waveforms that are indistinguishable from excitatory cells; namely basket cells that express cholescystokinin and vasoactive intestinal peptide (Wang et al., 2002; Zaitsev et al., 2009). Moreover, some studies have reported that some PV-expressing neurons can show regular spiking patterns, although the majority are fast spiking in most species (50–74%: rat: Kawaguchi &

Kubota, 1997; cat: Schwark & Li, 2000; mouse: Blatow et al., 2003; monkey: Krimer et al., 2005; human: Markram et al., 2004). It is possible that the outlier groups of RS inhibitory cells are larger in wallabies and some RS units identified in this study might be actually inhibitory in nature.

4.5 Conclusion

In conclusion, our findings show that it is possible to correlate the RF properties of cortical neurons with particular spike waveforms. Consistent with findings from cat V1 (Sun, 2021), we found that positive-spiking waveforms in wallaby V1 have similar RF types and spiking characteristics to wallaby LGN cells. More importantly, the RF properties of PS units strongly resembled the LGN cells we recorded in Chapter 3, supporting the concept that PS units in V1 are from axons of LGN cells. If this proves to be true, this correlation technique means that we can now simultaneously record from V1 cortical neurons and LGN afferents. This technique might prove very valuable for extracting far more data from cortical recordings in a range of species, to explain not just cortical connectivity but its subcortical input, thus making comparative analysis a more detailed and accurate pursuit than in earlier times.

Abbreviation	Meaning
Na+	Sodium
K+	Potassium
RS	Regular Spiking
FS	Fast Spiking
TS	Triphasic Spiking
CS	Compound Spiking
PS	Positive Spiking
SNR	Signal to noise ratio
SD	Standard Deviation
PSTH	Peristimulus Time Histogram
NS	Negative Spiking
HAPS	High-amplitude positive spikes
Ach	Acetylcholine

Chapter 5

Chapter 1 reviewed the current literature on the origin of functional maps in the mammalian visual cortex and highlighted the importance of studying a Marsupial, in my case the tammar wallaby *(Macropus eugenii)*. In Chapter 2, I used the intrinsic optical imaging method to examine the functional maps in the primary visual cortex (V1) of wallabies. In Chapter 3, I used the nonlinear input model (NIM), which is the most robust receptive field (RF) characterisation technique method, to analyse the spatial RFs of V1 and LGN cells in wallabies. Chapter 4 examined the relationship between RF types and extracellular spike waveforms. This section summarises the key findings of the results, discusses the limitations of the study and potential directions for future research.

5.1 Summary of Findings

5.1.1 Functional maps in the wallaby visual cortex

Most mammals have orientation-selective cells organised into structured orientation columns, which are arranged in pinwheel-like patterns across the cortex (Hubel et al., 1977; Blasdel & Salama, 1986; Bonhoeffer & Grinvald, 1991; Bartfeld & Grinvald, 1992; Obermayer & Blasdel, 1993; Hübener et al., 1997; Nauhaus et al., 2012). However, it has been found that species in the Clade Glires (e.g. rodents and rabbits) are an exception: despite having robust orientation selectivity in individual cells, these orientation-selective cells are randomly distributed across the cortex in salt-and-pepper orientation preference (OP) maps (Ohki et al., 2005; Van Hooser et al., 2005; Bonin et al., 2011; Espinosa & Stryker, 2012; Alonso et al., 2001). This is the starting point of my study: why do some mammals have structured pinwheel maps while others do not? What determines the structure of the cortical maps in mammals?

Marsupials are believed to have split away from the Eutherian mammals around 130-180 mya (Dawson, 1983). Thus, even if just one species of marsupial has a cortical organisation with a pinwheel structure, it argues strongly that pinwheel maps are the standard mammalian plan. The fact that I showed that the wallaby has a pinwheel OP map structure strongly supports pinwheels as the core plan in mammals. Moreover, my finding suggests that species in the Eutherian Clade Glires have a cortical structure that appears to be the exception in mammals. Had it been the case that wallabies had a salt-and-pepper map, then the pinwheel structure found in Eutherian mammals could be considered a recent evolutionary development. Of course, we must also consider the possibility that visually sophisticated marsupials, such as members of the kangaroo family (including wallabies), may have evolved pinwheel structures completely separately from the Eutherian mammals.

We used intrinsic optical imaging and multi-channel electrophysiological recordings to determine the type of OP map present in the wallaby V1. For the first time, we found strong evidence of orientation columns in a marsupial cortex. In the wallaby's central visual field, the orientation columns were organised radially around orientation centres in pinwheel-like patterns across the cortex. The pinwheel density in wallabies (1.60 pinwheels/mm^2) was low compared to that of cats (~3 pinwheels/mm^2) and monkeys (6–8 pinwheels/mm^2). In the peripheral visual field of the wallaby, the orientation columns were organised in linear bands, and pinwheel density was even lower (average pinwheel density = 1.06 mm^2). Moreover, in both central and peripheral visual fields, we demonstrated for the first time that neurons cluster according to their direction-selectivity preferences (DPs) in wallaby V1. We found that DPs shift continuously with orientation around a pinwheel across the cortex, except at the fracture line, where contiguous cortical regions show opposite DPs. This is similar to DP maps observed previously in cat and ferret V1 (Weliky et al., 1996; Shmuel & Grinvald, 2000; Ohki et al., 2005). In this study, we also investigated whether the ocular dominance map is present in V1 of tammar wallaby. We found that monocular stimulation of contralateral and ipsilateral eyes produced similar activity patterns. This is consistent with an early study by Vidysagar et al. (1992), where they found that contralateral and ipsilateral inputs did not segregate into different columns in the wallaby V1.

The finding of pinwheel maps in a marsupial and their similarity to those found in cats and monkeys confirms the unusual status of the salt-and-pepper maps present in rodents and rabbits. This suggests that columnar organisation of orientation preferences may well be a core feature of the mammalian visual cortex, but that the species in the Clade Glires may have lost the capacity to form structured cortical maps through evolution. What is so distinctive about rodents and rabbits that causes them to have salt-and-pepper maps? One option is that rodents have lost the genes that allow structured map formation. While completely plausible, we do not have genetic evidence to support this theory at the present time. Another possibility is that all mammals have the capacity to generate structured cortical maps, but they only form when other factors influence cortical structure during development. Previous studies have suggested that there is a correlation between the size of cortex and presence of pinwheels (Van Hooser et al., 2005; Mazade & Alonso, 2017). It is also possible that for non-eutherian mammals with a small V1, such as the Dunnart, you might find a salt-and-pepper architecture.

We proposed that the type of cortical map can be predicted by the central-to-peripheral ratio (CP ratio) of retinal ganglion cell (RGC) densities. In our review paper (Ibbotson and Jung, 2020), we extensively investigated the density of cells in the retina and the LGN across several species. We found that species like cats and monkeys with a high CP ratio (> 7), and a high number of LGN cells going into the cortex, tend to have orientation pinwheel maps. In contrast, species like rabbits and rodents with a low CP ratio (< 4), and a low number of LGN cells going into the cortex, have random salt-and-pepper maps. Moreover, we found in cats and primates that the pinwheel density increases as the CP ratio increases. Here, we found that wallabies have a highly centralised retinal input with a CP ratio of 20, which fits into the theory that the occurrence of OP maps in a particular species is related to its retinal structure, i.e. the CP ratio. Further, the fact that the wallabies' CP ratio is much lower than that of cats and primates (> 30) also matches the expectation from the CP theory.

The relationship between the CP ratio and emergence of pinwheel maps in the visual cortex could be explained in a logical way as follows, although it is important that the reader understands that this is purely a theory at this time. A high

CP ratio leads to a high number of LGN cells innervating the cortex, which causes the size of V1 to overexpand in a nonlinear fashion. This results in a relatively lower LGN axon density. In contrast, a low CP ratio does not cause V1 to expand to the same extent. Despite the initially lower number of LGN cells going into the cortex, the resulting LGN axon density is higher. For example, in the case of rodents, which have a CP ratio of 2, ~2000 thalamic axons are distributed within 4 mm^2 of the V1 area. In the case of monkeys, with a CP ratio of 40, ~1.5 million thalamic axons are distributed within 1000 mm^2 of V1. In other words, rodents have an LGN-axon density that is five times that of monkeys. Perhaps the LGN cells are so tightly packed in a small area in rodent V1 that it is almost impossible for them to cluster in a meaningful way, thus resulting in a salt-and-pepper arrangement on the cortex.

5.1.2 Receptive fields in V1 and LGN cells

Most mammals present orientation selectivity in their cortical cells, but they seem to show differences in terms of orientation selectivity of cells in their subcortical regions. In mice, LGN afferents have been found to be already orientation selective (Scholl et al., 2013; Sun et al., 2016). In cats and monkeys, orientation selectivity in LGN neurons is weak or absent, and OS appears to be created *de novo* in the cortex (Kremkow et al., 2016; Lee et al., 2016; Wilson et al., 2016). In our study, we wanted to investigate at which point in the visual pathways does orientation selectivity first occur in wallabies. Does orientation selectivity emerge early in the visual pathway like rodents, or later in V1, like cats and primates? How is this related to the pinwheel OP maps formed in wallaby V1?

Earlier studies have found that cortical neurons in the wallaby are highly tuned to orientation, in line with the majority of studied mammals (Sheng et al., 1990; Vidyasagar et al., 1992; Fleming et al., 1993; Ibbotson & Mark, 2003; Ibbotson et al., 2005). Further, using Fourier analysis of responses to moving gratings, Ibbotson et al. (2005) distinguished simple and complex cells in wallaby V1, similar to those found in the rat, cat, and monkey. However, these previous studies have neither measured the spatial structures of the RFs nor quantitatively measured the orientation selectivity of the LGN cells in the tammar wallaby.

In our study, we used multi-array electrodes (MEAs) to record from V1 and LGN cells of the tammar wallaby, and we used the NIM (as applied to cats in Almasi et al., 2020) to characterise the spatial and nonlinear aspects of the cells in response to white Gaussian noise (WGN). We examined the spatial RFs of 195 single units (SUs) in the V1s of six wallabies. We found that most of the neurons in wallaby V1 had oriented RFs (76%), roughly consistent with our findings using sinusoidal gratings (62%), and of the previous findings using grating stimuli by Ibbotson and Mark (2003) (70%). Using the F1/F0 classification of simple and complex cells, we found that 84% of simple cells in our population had single-filters (which resemble simple cells: Simoncelli & Llampaninski, 2004), while complex cells had a more varied distribution of filters, with 62% having multi-filter cells (which resemble the expectations for complex cells: Adelson & Bergen, 1985). As in the case of cats, the NIM framework has offered a far more comprehensive analysis of RF properties of neurons in the wallaby cortex, with greater variation in RF structures of simple and complex cells than previously reported. Our study thus confirms the advantages of the NIM and demonstrates its applicability to the study of how different cells in the cortex respond to visual stimuli in a wider range of species.

Furthermore, for the first time, we recorded 12 LGN cells from a wallaby from which we were able to recover their spatial RFs. We found that all LGN units had blob-like features that responded to either ON or OFF polarity. Using the F2/F1 ratio, we found that all our LGN cells had linear spatial summation, more in line with the expectations from X-like cells in the retina. Further, most of the LGN cells were non-orientation-selective, but 33% of cells had mildly elongated RFs and some mild orientation biases. While these numbers are too small to draw major conclusions, our findings suggest that the orientation selectivity observed in wallaby V1 either emerges completely or is substantially enhanced by processing in V1, as is the case in cats and monkeys.

In relation to OP maps, we proposed that the existence of orientation selectivity in LGN may disrupt the development of an ordered pinwheel OP map. Partially orientation-selective LGN cells could send signals into V1 in a random spatial order, thus imposing a salt-and-pepper arrangement on the cortex. In species

with high CP ratios, where there is reduced cell diversity in the central retina (e.g. Dacey & Packer, 2003), the creation of more sophisticated response characteristics such as orientation selectivity appears to be pushed further up the visual pathway. These species are more likely to create orientation selectivity *de novo* in the cortex and this, in turn, may lead to more structured OP maps.

5.1.3 Correlating extracellular spike waveforms with spatial RFs

Recent development of dense extracellular multi-electrode arrays (MEAs) has allowed simultaneous recordings from multiple neurons and more detailed identification of extracellular spike waveform properties. Several studies have reported more non-traditional extracellular waveform shapes, like positive spiking waveforms (Gold et al., 2006; 2009; Robbins et al., 2013; Gharat & Baker, 2017). Sun (2019) identified five distinct classes of extracellular spike waveforms in cat V1: regular spiking (RS), fast spiking (FS), triphasic spiking (TS), compound spiking (CS), and positive spiking (PS) and suggested that PS waveforms have similar RF types and spiking characteristics to the thalamic afferents that originate outside the cortex. We wanted to know if the wallaby cortex had similar characteristics to the cat cortex and whether we can correlate the spatial RFs and spiking characteristics of positive-dominant waveforms in wallaby V1 to wallaby LGN cells.

In Chapter 4, I classified 642 single units (SUs) in the wallaby V1 into the same five waveform classes as we had found in the cat (RS, 68%; FS, 12%; TS, 4%; CS, 5% and PS, 11%). Our findings show that it is possible to correlate the RF properties of cortical neurons with particular spike waveforms. For example, the proportion of PS units with non-orientation-selective RFs in wallaby V1 (59%), though lower compared to that in cat V1 (74–83%: Sun, 2021), roughly corresponded to the proportion of non-oriented RFs in wallaby LGN cells (66%), recorded in Chapter 3. Further, we found that PS units in wallaby V1 have similar spiking characteristics (e.g. low spike rates and low latency) to the LGN cells in the wallaby. This could indicate that PS units in V1 are actually recordings from axons of LGN cells. If this were true, we can now simultaneously record from V1 cortical

neurons and LGN afferents, which would allow us to extract data from cortical recordings to explain not just cortical connectivity but also its subcortical input.

5.2 Limitations and future work

5.2.1 LGN experiments

Due to the onset of COVID-19 restrictions, the LGN experiments had to be suspended. Units from one animal, while promising, are not enough for an appropriate population distribution. With the easing of restrictions, we plan to resume our experiments to add more units to the data set and to be able to draw more definitive conclusions regarding orientation selectivity of LGN cells in the tammar wallaby. Further, with added units, we expect to conduct a more robust investigation into the correlations between LGN cells and particular spiking waveforms in V1.

5.2.2 Understanding cortical maps through comparative physiology

We propose three experiments that would greatly assist in creating a better understanding of the cortical map structures in mammals. The proposed experiments include the following species: brown antechinus *(Antechinus stuartii),* opossum *(Didelphidae),* fruit bat *(Pteropus Alecto).* In the following, I will explain why these species are chosen for study.

Figure 5.1 Three proposed species: brown antechinus, opossum, and fruit bat. Source:

brown antechinus, virginia opossum, megabats from open source under Creative Commons license.

We previously established that convergent evolution might play a role in determining the formation of OP maps. As mentioned above, a study of rodent-like marsupials would provide insight into the extent to which environmental factors could influence cortical structure development. A rodent-like marsupial that could be studied is the brown antechinus *(Antechinus stuartii),* which is a small carnivorous marsupial (order: Dasyuromorphia). They are also called broad-footed marsupial mice due to their obvious resemblance to Eutherian mice (Figure 5.1). They are crepuscular or nocturnal, specialised for climbing and dwell in forests (Tyndale-Biscoe, 2005; Naylor et al., 2008). If the antechinus has a pinwheel OP, this would suggest rodents and rabbits have salt-and-pepper OP maps because of their phylogenetic grouping under the Clade Glires. However, if the antechinus has a salt-and-pepper OP map, despite being a marsupial, this would disprove the hypothesis that salt-and-pepper maps are exclusive to species within the Clade Glires. Further, this would suggest that salt-and-pepper OP maps are driven by the ecological niches in which rodent-like species are found.

A second proposed experiment involves the opossum *(Didelphidae),* which is an American marsupial. Why do we want to study another marsupial? The reason is that the wallaby belongs to the relatively recent Australian order, Diprotodontia while the opossum belongs to an archaic marsupial order, Didelphimorphia (Samollow, 2008). They may, therefore, have a V1 that is representative of early marsupial cortex. The small percentage of orientation selective cells in opossum V1 compared to wallabies makes the project particularly interesting and, as outlined in the section below, their retinal design is also advantageous for the project. The opossum has a highly centralised retinal input (Rapaport et al., 1981), and it has small eye divergence and large binocular overlap, like cats and monkeys (Figure 5.1). From these parameters we would predict a pinwheel structure based on our theory. However, opossums have a very low percentage of orientation selective cells in cortex (< 50%), which differs from all the other species that have been shown to have pinwheel structures. All the other mammals with pinwheel structures

have very high percentages of OS in V1 (> 70%). Therefore, the opossum is a very interesting species to investigate.

A third proposed experiment is one that tests the CP ratio threshold, i.e. precisely what CP forms the border between pinwheel and salt-and-pepper OP maps. Of the species studied so far showing a pinwheel structure, the tree shrew has the lowest CP ratio (7.6). In contrast, of the species studied so far with salt-and-pepper structures, the squirrel has the highest CP ratio (3.2). Based on this, we established that if the CP ratio is < 4, the cortex is salt-and-pepper; if the CP ratio is > 7, the cortex has a pinwheel structure. What about animals with a CP ratio in this grey area (i.e. CP between 4 and 7)? It would be impossible for a single experiment to arrive at a definitive answer. It would only be possible to approximate the threshold by conducting several experiments with species with CP ratios within this grey area.

A good starting point could be the fruit bat. The fruit bat *(Rousettus aegyptiacus)* is in the Eutherian order of Chiroptera, which is in the Clade Laurasiastheria, which also includes ferrets and cats. The fruit bat uses echolocation for navigation but also has excellent frontal vision (Figure 5.1). While the retinotopy of fruit bat visual cortex has been studied (Rosa et al., 1994) and strong orientation selectivity has been recorded at the single-cell level, there has been no measurement of OP maps in bat V1. Fruit bats are known to have a centralised retinal input to the cortex (Pettigrew et al., 1968). They have more than 9,000 RGCs/mm^2 at the centre of retinal specialisation, which is similar to cats (10,000 cells/mm^2). However, their CP ratio was found to be relatively low (4.5). This is not too much higher than that of the squirrel (3.2). It is worth noting that the relatively low CP ratio of the fruit bat is because the peripheral cell density is unusually high compared to the central cell density. If the fruit bat has a pinwheel map, this would indicate that the threshold between pinwheel and salt-and-pepper maps is somewhere between a CP ratio of 4 and 4.5. If the fruit bat has a salt-and-pepper map, this would open the door for a lot of interesting questions. Using the robust techniques used in this study (e.g. intrinsic optical imaging, RF characterisation, and correlation of spike waveforms), we would be able to gain a broader understanding of the functional organisation of the visual cortex beyond that of the outlined species.

Bibliography

Aboitiz, F., & Montiel, J. (2003). One hundred million years of interhemispheric communication: the history of the corpus callosum. *Brazilian journal of medical and biological research, 36*(4), 409-420.

Adam, Y., Kim, J. J., Lou, S., Zhao, Y., Xie, M. E., Brinks, D., Wu, H., Mostajo-Radji, M. A., Kheifets, S., & Parot, V. (2019). Voltage imaging and optogenetics reveal behaviour-dependent changes in hippocampal dynamics. *Nature, 569*(7756), 413-417.

Adams, D. L., & Horton, J. C. (2003). Capricious expression of cortical columns in the primate brain. *Nature neuroscience, 6*(2), 113-114.

Adelson, E. H., & Bergen, J. R. (1985). Spatiotemporal energy models for the perception of motion. *Josa a, 2*(2), 284-299.

Almasi, A., Meffin, H., Cloherty, S. L., Wong, Y., Yunzab, M., & Ibbotson, M. R. (2020). Mechanisms of Feature Selectivity and Invariance in Primary Visual Cortex. *Cerebral Cortex, 30*(9), 5067-5087. https://doi.org/10.1093/cercor/bhaa102

Almasi, A. (2017). An investigation of spatial receptive fields of complex cells in the primary visual cortex. [Doctoral dissertation, The University of Melbourne]. Melbourne.

Alonso, J.-M. (2002). Book Review: Neural Connections and Receptive Field Properties in the Primary Visual Cortex. *The neuroscientist, 8*(5), 443-456.

Alonso, J.-M., Usrey, W. M., & Reid, R. C. (2001). Rules of connectivity between geniculate cells and simple cells in cat primary visual cortex. *Journal of Neuroscience, 21*(11), 4002-4015.

Bartfeld, E., & Grinvald, A. (1992). Relationships between orientation-preference pinwheels, cytochrome oxidase blobs, and ocular-dominance columns in primate striate cortex. *Proceedings of the National Academy of Sciences, 89*(24), 11905-11909.

Blasdel, G. G. (1992). Orientation selectivity, preference, and continuity in monkey striate cortex. *Journal of Neuroscience, 12*(8), 3139-3161.

Blasdel, G. G., & Salama, G. (1986). Voltage-sensitive dyes reveal a modular organization in monkey striate cortex. *Nature, 321*(6070), 579-585.

Bonhoeffer, T., & Grinvald, A. (1991). Iso-orientation domains in cat visual cortex are arranged in pinwheel-like patterns. *Nature, 353*(6343), 429-431.

Bonin, V., Histed, M. H., Yurgenson, S., & Reid, R. C. (2011). Local diversity and fine-scale organization of receptive fields in mouse visual cortex. *Journal of Neuroscience, 31*(50), 18506-18521.

Bosking, W. H., Zhang, Y., Schofield, B., & Fitzpatrick, D. (1997). Orientation selectivity and the arrangement of horizontal connections in tree shrew striate cortex. *Journal of Neuroscience, 17*(6), 2112-2127.

Bullier, J., & Henry, G. H. (1980). Ordinal position and afferent input of neurons in monkey striate cortex. *Journal of Comparative Neurology, 193*(4), 913-935.

Butts, D. A. (2019). Data-driven approaches to understanding visual neuron activity. *Annual review of vision science, 5*, 451-477.

Carreira-Perpinán, M. A., Lister, R. J., & Goodhill, G. J. (2005). A computational model for the development of multiple maps in primary visual cortex. *Cerebral Cortex, 15*(8), 1222-1233.

Chapman, B., & Bonhoeffer, T. (1998). Overrepresentation of horizontal and vertical orientation preferences in developing ferret area 17. *Proceedings of the National Academy of Sciences, 95*(5), 2609-2614.

Chapman, B., Stryker, M. P., & Bonhoeffer, T. (1996). Development of orientation preference maps in ferret primary visual cortex. *Journal of Neuroscience, 16*(20), 6443-6453.

Chen, X., Han, F., Poo, M.-m., & Dan, Y. (2007). Excitatory and suppressive receptive field subunits in awake monkey primary visual cortex (V1). *Proceedings of the National Academy of Sciences, 104*(48), 19120-19125.

Chichilnisky, E. (2001). A simple white noise analysis of neuronal light responses. *Network: Computation in Neural Systems*, 12 (2), 199-213.

Cloherty, S. L., Hughes, N. J., Hietanen, M. A., Bhagavatula, P. S., Goodhill, G. J., & Ibbotson, M. R. (2016). Sensory experience modifies feature map relationships in visual cortex. *Elife, 5*, e13911.

Collin, S. (1999). Behavioural ecology and retinal cell topography. In *Adaptive mechanisms in the ecology of vision* (pp. 509-535). Springer.

Collin, S. P. (2008). A web-based archive for topographic maps of retinal cell distribution in vertebrates. *Clinical and Experimental Optometry, 91*(1), 85-95.

Coppola, D. M., & White, L. E. (2004). Visual experience promotes the isotropic representation of orientation preference. *Visual neuroscience, 21*(1), 39.

Crewther, D. P., Crewther, S. G., & Sanderson, K. J. (1984). Primary visual cortex in the brushtailed possum: receptive field properties and corticocortical connections. *Brain, Behavior and Evolution, 24*(4), 184-197.

Crowder, N. A., Van Kleef, J., Dreher, B., & Ibbotson, M. R. (2007). Complex cells increase their phase sensitivity at low contrasts and following adaptation. *Journal of neurophysiology, 98*(3), 1155-1166.

Dacey, D. M., & Packer, O. S. (2003). Colour coding in the primate retina: diverse cell types and cone-specific circuitry. *Current opinion in neurobiology, 13*(4), 421-427.

Dawson, T. J. (1983). *Monotremes and marsupials*. E. Arnold.

De Valois, R. L., Yund, E. W., & Hepler, N. (1982). The orientation and direction selectivity of cells in macaque visual cortex. *Vision research, 22*(5), 531-544.

Disney, A. A., Aoki, C., & Hawken, M. J. (2012). Cholinergic suppression of visual responses in primate V1 is mediated by GABAergic inhibition. Journal of neurophysiology, *108*(7), 1907-1923.

Dräger, U. C. (1975). Receptive fields of single cells and topography in mouse visual cortex. *Journal of Comparative Neurology, 160*(3), 269-289.

Dubner, R., & Zeki, S. (1971). Response properites and receptive fields of cells in an anatomically defined region of the superior temporal sulcus in the monkey. *Brain research*.

Emmanouil, D. E., & Quock, R. M. (2007). Advances in understanding the actions of nitrous oxide. *Anesthesia progress, 54*(1), 9-18.

Enroth-Cugell, C., & Robson, J. G. (1966). The contrast sensitivity of retinal ganglion cells of the cat. *The Journal of physiology, 187*(3), 517-552.

Erwin, E., Obermayer, K., & Schulten, K. (1995). Models of orientation and ocular dominance columns in the visual cortex: A critical comparison. *Neural Computation, 7*(3), 425-468.

Erisir, A., Levey, A. I., & Aoki, C. (2001). Muscarinic receptor m2R distribution in the cat visual cortex: laminar distribution, relationship to GABAergic neurons, and the efect of cingulate lesions. *J Comp Neurol, 441*, 168-185.

Espinosa, J. S., & Stryker, M. P. (2012). Development and plasticity of the primary visual cortex. *Neuron, 75*(2), 230-249.

Feldmeyer, D., Egger, V., Lübke, J., & Sakmann, B. (1999). Reliable synaptic connections between pairs of excitatory layer 4 neurones within a single 'barrel' of developing rat somatosensory cortex. *The Journal of physiology, 521*(1), 169-190.

Feldmeyer, D., Lübke, J., Silver, R. A., & Sakmann, B. (2002). Synaptic connections between layer 4 spiny neurone-layer 2/3 pyramidal cell pairs in juvenile rat barrel cortex: physiology and anatomy of interlaminar signalling within a cortical column. *The Journal of physiology, 538*(3), 803-822.

Ferster, D., Chung, S., & Wheat, H. (1996). Orientation selectivity of thalamic input to simple cells of cat visual cortex. *Nature, 380*(6571), 249-252.

Ferster, D., & Jagadeesh, B. (1991). Nonlinearity of spatial summation in simple cells of areas 17 and 18 of cat visual cortex. *Journal of neurophysiology, 66*(5), 1667-1679.

Ferster, D., & Miller, K. D. (2000). Neural mechanisms of orientation selectivity in the visual cortex. *Annual review of neuroscience, 23*(1), 441-471.

Fitzgerald, J. D., Rowekamp, R. J., Sincich, L. C., & Sharpee, T. O. (2011). Second order dimensionality reduction using minimum and maximum mutual information models. *PLoS Comput Biol, 7*(10), e1002249.

Fitzpatrick, D. (1996). The functional organization of local circuits in visual cortex: insights from the study of tree shrew striate cortex. *Cerebral Cortex, 6*(3), 329-341.

Florence, S., & Kaas, J. (1992). Ocular dominance columns in area 17 of Old World macaque and talapoin monkeys: complete reconstructions and quantitative analyses. *Visual neuroscience, 8*(5), 449-462.

Fournier, J., Monier, C., Levy, M., Marre, O., Sári, K., Kisvárday, Z. F., & Frégnac, Y. (2014). Hidden complexity of synaptic receptive fields in cat V1. *Journal of Neuroscience, 34*(16), 5515-5528.

Frenkel, M. Y., & Bear, M. F. (2004). How monocular deprivation shifts ocular dominance in visual cortex of young mice. *Neuron, 44*(6), 917-923.

Gabbott, P., & Somogyi, P. (1986). Quantitative distribution of GABA-immunoreactive neurons in the visual cortex (area 17) of the cat. *Experimental Brain Research, 61*(2), 323-331.

Gharat, A., & Baker, C. L. (2017). Nonlinear Y-like receptive fields in the early visual cortex: An intermediate stage for building cue-invariant receptive fields from subcortical Y cells. *Journal of Neuroscience, 37*(4), 998-1013.

Giacomantonio, C. E., Ibbotson, M. R., & Goodhill, G. J. (2010). The influence of restricted orientation rearing on map structure in primary visual cortex. *Neuroimage, 52*(3), 875-883.

[Record #348 is using a reference type undefined in this output style.]

Goodhill, G. J. (2007). Contributions of theoretical modeling to the understanding of neural map development. *Neuron, 56*(2), 301-311.

Goodhill, G. J., & Sejnowski, T. J. (1997). A unifying objective function for topographic mappings. *Neural Computation, 9*(6), 1291-1303.

Grabska-Barwińska, A., Distler, C., Hoffmann, K. P., & Jancke, D. (2009). Contrast independence of cardinal preference: stable oblique effect in orientation maps of ferret visual cortex. *European Journal of Neuroscience, 29*(6), 1258-1270.

Grinvald, A., Frostig, R. D., Siegel, R. M., & Bartfeld, E. (1991). High-resolution optical imaging of functional brain architecture in the awake monkey. *Proceedings of the National Academy of Sciences, 88*(24), 11559-11563.

Grinvald, A., Lieke, E., Frostig, R. D., Gilbert, C. D., & Wiesel, T. N. (1986). Functional architecture of cortex revealed by optical imaging of intrinsic signals. *Nature, 324*(6095), 361-364.

Grubb, M. S., & Thompson, I. D. (2003). Quantitative characterization of visual response properties in the mouse dorsal lateral geniculate nucleus. *Journal of neurophysiology, 90*(6), 3594-3607.

Gummer, A. W., & Mark, R. F. (1994). Patterned neural activity in brain stem auditory areas of a prehearing mammal, the tammar wallaby (Macropus eugenii). *Neuroreport: An International Journal for the Rapid Communication of Research in Neuroscience*.

Heath, C., & Jones, E. (1971). An experimental study of ascending connections from the posterior group of thalamic nuclei in the cat. *Journal of Comparative Neurology, 141*(4), 397-425.

Hebb, D. O. (1949). The organization of behavior: a neuropsychological theory. J. Wiley; Chapman & Hall.

Hemmi, J., & Mark, R. (1998). Visual acuity, contrast sensitivity and retinal magnification in a marsupial, the tammar wallaby (Macropus eugenii). *Journal of Comparative Physiology A, 183*(3), 379-387.

Hess, D. T., & Edwards, M. A. (1987). Anatomical demonstration of ocular segregation in the retinogeniculocortical pathway of the New World capuchin monkey (Cebus apella). *Journal of Comparative Neurology, 264*(3), 409-420.

Hickford, D., Frankenberg, S., & Renfree, M. B. (2009). The tammar wallaby, Macropus eugenii: a model kangaroo for the study of developmental and reproductive biology. *Cold Spring Harbor Protocols, 2009*(12), pdb. emo137.

Hinds, L., Poole, W., Tyndale-Biscoe, C., Vanoorschot, R., & Cooper, D. (1989). Reproductive-Biology and the Potential for Genetic-Studies in the Tammar Wallaby, Macropus-Eugenii. *Australian journal of zoology, 37*(3), 223-234.

Hochstein, S., & Shapley, R. (1976a). Linear and nonlinear spatial subunits in Y cat retinal ganglion cells. *The Journal of physiology, 262*(2), 265-284.

Hochstein, S., & Shapley, R. (1976b). Quantitative analysis of retinal ganglion cell classifications. *The Journal of physiology, 262*(2), 237-264.

Horton, J. C., & Hubel, D. H. (1981). Regular patchy distribution of cytochrome oxidase staining in primary visual cortex of macaque monkey. *Nature, 292*(5825), 762-764.

Hubel, D. H., & Wiesel, T. (1963). Shape and arrangement of columns in cat's striate cortex. *The Journal of physiology, 165*(3), 559.

Hubel, D. H., & Wiesel, T. N. (1962). Receptive fields, binocular interaction and functional architecture in the cat's visual cortex. *The Journal of physiology, 160*(1), 106.

Hubel, D. H., & Wiesel, T. N. (1968). Receptive fields and functional architecture of monkey striate cortex. *The Journal of physiology, 195*(1), 215-243.

Hubel, D. H., & Wiesel, T. N. (1969). Anatomical demonstration of columns in the monkey striate cortex. *Nature, 221*(5182), 747-750.

Hubel, D. H., & Wiesel, T. N. (1974). Sequence regularity and geometry of orientation columns in the monkey striate cortex. *Journal of Comparative Neurology, 158*(3), 267-293.

Hubel, D. H., Wiesel, T. N., LeVay, S., Barlow, H. B., & Gaze, R. M. (1977). Plasticity of ocular dominance columns in monkey striate cortex. *Philosophical Transactions of the Royal Society of London. B, Biological Sciences, 278*(961), 377-409.

Hubel, D. H., Wiesel, T. N., & Stryker, M. P. (1978). Anatomical demonstration of orientation columns in macaque monkey. *Journal of Comparative Neurology, 177*(3), 361-379.

Hübener, M., Shoham, D., Grinvald, A., & Bonhoeffer, T. (1997). Spatial relationships among three columnar systems in cat area 17. *Journal of Neuroscience, 17*(23), 9270-9284.

Hughes, A. (1977). The topography of vision in mammals of contrasting life style: comparative optics and retinal organisation. In *The visual system in vertebrates* (pp. 613-756). Springer.

Ibbotson, M., & Jung, Y. J. (2020). Origins of Functional Organization in the Visual Cortex. *Frontiers in Systems Neuroscience, 14*, 10.

Ibbotson, M., & Mark, R. (2003). Orientation and spatiotemporal tuning of cells in the primary visual cortex of an Australian marsupial, the wallaby Macropus eugenii. *Journal of Comparative Physiology A, 189*(2), 115-123.

Ibbotson, M. R., Price, N., & Crowder, N. A. (2005). On the division of cortical cells into simple and complex types: a comparative viewpoint. *Journal of neurophysiology, 93*(6), 3699-3702.

Jang, J., Song, M., & Paik, S.-B. (2020). Retino-Cortical Mapping Ratio Predicts Columnar and Salt-and-Pepper Organization in Mammalian Visual Cortex. *Cell Reports, 30*(10), 3270-3279. e3273.

Kaplan, E., & Shapley, R. (1982). X and Y cells in the lateral geniculate nucleus of macaque monkeys. *The Journal of physiology, 330*(1), 125-143.

Karim, A. R., & Kojima, H. (2010). The what and why of perceptual asymmetries in the visual domain. *Advances in Cognitive Psychology, 6*, 103.

Karlen, S. J., & Krubitzer, L. (2007). The functional and anatomical organization of marsupial neocortex: evidence for parallel evolution across mammals. *Progress in neurobiology, 82*(3), 122-141.

Kaschube, M., Schnabel, M., Löwel, S., Coppola, D. M., White, L. E., & Wolf, F. (2010). Universality in the evolution of orientation columns in the visual cortex. *Science, 330*(6007), 1113-1116.

Kaschube, M., Wolf, F., Puhlmann, M., Rathjen, S., Schmidt, K. F., Geisel, T., & Löwel, S. (2003). The pattern of ocular dominance columns in cat primary visual cortex: intra-and interindividual variability of column spacing and its dependence on genetic background. *European Journal of Neuroscience, 18*(12), 3251-3266.

Kolb, H., & Famigilietti, E. (1974). Rod and cone pathways in the inner plexiform layer of cat retina. *Science, 186*(4158), 47-49.

Kolb, H., Nelson, R., & Mariani, A. (1981). Amacrine cells, bipolar cells and ganglion cells of the cat retina: a Golgi study. *Vision research, 21*(7), 1081-1114.

Kossut, M., Thompson, I., & Blakemore, C. (1983). Ocular dominance columns in cat striate cortex and effects of monocular deprivation: a 2-deoxyglucose study. *Acta Neurobiol. Exp, 43*, 273-282.

Kremkow, J., & Alonso, J.-M. (2018). Thalamocortical circuits and functional architecture. *Annual review of vision science, 4*, 263-285.

Kremkow, J., Jin, J., Wang, Y., & Alonso, J. M. (2016). Principles underlying sensory map topography in primary visual cortex. *Nature, 533*(7601), 52-57.

Kuffler, S. W. (1953). Discharge patterns and functional organization of mammalian retina. *Journal of neurophysiology, 16*(1), 37-68.

Langeron, O., Vivien, B., Paqueron, X., Saillant, G., Riou, B., Coriat, P., & Lille, F. (1999). Effects of propofol, propofol-nitrous oxide and midazolam on cortical somatosensory evoked potentials during sufentanil anaesthesia for major spinal surgery. *British Journal of Anaesthesia, 82*(3), 340-345.

Lee, K.-S., Huang, X., & Fitzpatrick, D. (2016). Topology of ON and OFF inputs in visual cortex enables an invariant columnar architecture. *Nature, 533*(7601), 90-94.

LeVay, S., & Gilbert, C. D. (1976). Laminar patterns of geniculocortical projection in the cat. *Brain research, 113*(1), 1-19.

Lillegraven, J. A., Thompson, S. D., McNab, B. K., & Patton, J. L. (1987). The origin of eutherian mammals. *Biological Journal of the Linnean Society, 32*(3), 281-336.

Liu, L., She, L., Chen, M., Liu, T., Lu, H. D., Dan, Y., & Poo, M.-m. (2016). Spatial structure of neuronal receptive field in awake monkey secondary visual cortex (V2). *Proceedings of the National Academy of Sciences, 113*(7), 1913-1918.

Livingstone, M. S., & Hubel, D. H. (1984). Anatomy and physiology of a color system in the primate visual cortex. *Journal of Neuroscience, 4*(1), 309-356.

Ludwig, K. A., Miriani, R. M., Langhals, N. B., Joseph, M. D., Anderson, D. J., & Kipke, D. R. (2009). Using a common average reference to improve cortical neuron recordings from microelectrode arrays. *Journal of neurophysiology, 101*(3), 1679-1689.

Luo, Z.-X., Yuan, C.-X., Meng, Q.-J., & Ji, Q. (2011). A Jurassic eutherian mammal and divergence of marsupials and placentals. *Nature, 476*(7361), 442-445.

Mandl, G., Desai, N., & Capaday, C. (1980). Nitrous oxide modifies visual responses in the cat retina, striate cortex and superior colliculus. *Brain research, 193*(2), 401-414.

Marshel, J. H., Kaye, A. P., Nauhaus, I., & Callaway, E. M. (2012). Anterior-posterior direction opponency in the superficial mouse lateral geniculate nucleus. *Neuron, 76*(4), 713-720.

Maunsell, J., & van Essen, D. C. (1983). The connections of the middle temporal visual area (MT) and their relationship to a cortical hierarchy in the macaque monkey. *Journal of Neuroscience, 3*(12), 2563-2586.

Mazade, R., & Alonso, J. M. (2017). Thalamocortical processing in vision. *Visual neuroscience, 34*, E007.

McCluskey, S., Marotte, L., & Ashwell, K. W. (2008). Development of the vestibular apparatus and central vestibular connections in a wallaby (Macropus eugenii). *Brain, Behavior and Evolution, 71*(4), 271-286.

McFarland, J. M., Cui, Y., & Butts, D. A. (2013). Inferring nonlinear neuronal computation based on physiologically plausible inputs. *PLoS Comput Biol, 9*(7), e1003143.

Metin, C., Godement, P., & Imbert, M. (1988). The primary visual cortex in the mouse: receptive field properties and functional organization. *Experimental Brain Research, 69*(3), 594-612.

Meyer, J. (1981). A quantitative comparison of the parts of the brains of two Australian marsupials and some eutherian mammals. *Brain, Behavior and Evolution, 18*(1-2), 60-71.

Miller, K. D., Erwin, E., & Kayser, A. (1999). Is the development of orientation selectivity instructed by activity? *Journal of neurobiology, 41*(1), 44-57.

Mohan, Y. S., Jayakumar, J., Lloyd, E. K., Levichkina, E., & Vidyasagar, T. R. (2019). Diversity of Feature Selectivity in Macaque Visual Cortex Arising from a Limited Number of Broadly Tuned Input Channels. *Cerebral Cortex, 29*(12), 5255-5268.

Murphy, E. H., & Berman, N. (1979). The rabbit and the cat: a comparison of some features of response properties of single cells in the primary visual cortex. *Journal of Comparative Neurology, 188*(3), 401-427.

Nauhaus, I., Nielsen, K. J., Disney, A. A., & Callaway, E. M. (2012). Orthogonal micro-organization of orientation and spatial frequency in primate primary visual cortex. *Nature neuroscience, 15*(12), 1683.

Nishimoto, S., Ishida, T., & Ohzawa, I. (2006). Receptive field properties of neurons in the early visual cortex revealed by local spectral reverse correlation. *Journal of Neuroscience*, 26(12), 3269–3280.

Obermayer, K., & Blasdel, G. G. (1993). Geometry of orientation and ocular dominance columns in monkey striate cortex. *Journal of Neuroscience, 13*(10), 4114-4129.

Ohki, K., Chung, S., Ch'ng, Y. H., Kara, P., & Reid, R. C. (2005). Functional imaging with cellular resolution reveals precise micro-architecture in visual cortex. *Nature, 433*(7026), 597-603.

Olshausen, B. A., & Field, D. J. (1996). Natural image statistics and efficient coding. *Network: computation in neural systems, 7*(2), 333-339.

Oyster, C. W., Takahashi, E. S., & Hurst, D. C. (1981). Density, soma size, and regional distribution of rabbit retinal ganglion cells. *Journal of Neuroscience, 1*(12), 1331-1346.

Pachitariu, M., Steinmetz, N. A., Kadir, S. N., Carandini, M., & Harris, K. D. (2016). Fast and accurate spike sorting of high-channel count probes with KiloSort. *Advances in neural information processing systems, 29*, 4448-4456.

Paik, S.-B., & Ringach, D. L. (2011). Retinal origin of orientation maps in visual cortex. *Nature neuroscience, 14*(7), 919.

Paninski, L. (2003). Convergence properties of some spike-triggered analysis techniques. *In Advances in neural information processing systems*, 189-196.

Park, M., & Pillow, W. (2011). Bayesian spike-triggered covariance analysis. *In Advances in neural information processing systems* (pp. 1692-1700).

Payne, B., & Berman, N. (1983). Functional organization of neurons in cat striate cortex: variations in preferred orientation and orientation selectivity with receptive-field type, ocular dominance, and location in visual-field map. *Journal of neurophysiology, 49*(4), 1051-1072.

Payne, B. R., & Peters, A. (2002). The concept of cat primary visual cortex. In *The cat primary visual cortex* (pp. 1-129). Elsevier.

Peters, A., & Sethares, C. (1991). Organization of pyramidal neurons in area 17 of monkey visual cortex. *Journal of Comparative Neurology, 306*(1), 1-23.

Pettigrew, J., Nikara, T., & Bishop, P. (1968). Responses to moving slits by single units in cat striate cortex. *Experimental Brain Research, 6*(4), 373-390.

Piscopo, D. M., El-Danaf, R. N., Huberman, A. D., & Niell, C. M. (2013). Diverse visual features encoded in mouse lateral geniculate nucleus. *Journal of Neuroscience, 33*(11), 4642-4656.

Ratzlaff, E. H., & Grinvald, A. (1991). A tandem-lens epifluorescence macroscope: hundred-fold brightness advantage for wide-field imaging. *Journal of neuroscience methods, 36*(2-3), 127-137.

Reese, B. E., & Keeley, P. W. (2015). Design principles and developmental mechanisms underlying retinal mosaics. *Biological Reviews, 90*(3), 854-876.

Reid, R. C. (2012). From functional architecture to functional connectomics. *Neuron, 75*(2), 209-217.

Renfree, M. B. (2010). Marsupials: placental mammals with a difference. *Placenta, 31*, S21-S26.

Renfree, M. B., Short, R., & Shaw, G. (1996). Sexual differentiation of the urogenital system of the fetal and neonatal tammar wallaby, Macropus eugenii. *Anatomy and Embryology, 194*(2), 111-134.

Renfree, M. B., Wilson, J. D., Short, R. V., Shaw, G., & George, F. W. (1992). Steroid hormone content of the gonads of the tammar wallaby during sexual differentiation. *Biology of reproduction, 47*(4), 644-647.

Ringach, D. L., Hawken, M. J., & Shapley, R. (2002). Receptive field structure of neurons in monkey primary visual cortex revealed by stimulation with natural image sequences. Journal of Vision, 2(1), 2–2.

Ringach, D. L. (2004). Mapping receptive fields in primary visual cortex. *The Journal of physiology, 558*(3), 717-728.

Rocha-Miranda, C., Linden, R., Volchan, E., Lent, R., & Bombardieri Jr, R. (1976). Receptive field properties of single units in the opossum striate cortex. *Brain research, 104*(2), 197-219.

Rocha-Miranda, C. E., Bombardieri, J. R., & Linden, R. (1973). Receptive fields in the visual cortex of the opossum. *Brain research, 63*, 362-367.

Rosa, M. G., Krubitzer, L. A., Molnár, Z., & Nelson, J. E. (1999). Organization of visual cortex in the northern quoll, Dasyurus hallucatus: evidence for a homologue of the second visual area in marsupials. *European Journal of Neuroscience, 11*(3), 907-915.

Rosenberg, A., Husson, T. R., & Issa, N. P. (2010). Subcortical representation of non-Fourier image features. *Journal of Neuroscience, 30*(6), 1985-1993.

Rossant, C., Kadir, S. N., Goodman, D. F., Schulman, J., Hunter, M. L., Saleem, A. B., Grosmark, A., Belluscio, M., Denfield, G. H., & Ecker, A. S. (2016). Spike sorting for large, dense electrode arrays. *Nature neuroscience, 19*(4), 634-641.

Rovamo, J., Virsu, V., Laurinen, P., & Hyvärinen, L. (1982). Resolution of gratings oriented along and across meridians in peripheral vision. *Investigative ophthalmology & visual science, 23*(5), 666-670.

Rowe, M. H., Benevento, L., & Rezak, M. (1978). Some observations on the patterns of segregated geniculate inputs to the visual cortex in New World primates: an autoradiographic study. *Brain research, 159*(2), 371-378.

Rust, N. C., Schwartz, O., Movshon, J. A., & Simoncelli, E. (2004). Spike-triggered characterization of excitatory and suppressive stimulus dimensions in monkey v1. *Neurocomputing*, 58 , 793-799.

Rust, N. C., Schwartz, O., Movshon, J. A., & Simoncelli, E. P. (2005). Spatiotemporal elements of macaque v1 receptive fields. *Neuron, 46*(6), 945-956.

Samollow, P. B. (2008). The opossum genome: insights and opportunities from an alternative mammal. *Genome research, 18*(8), 1199-1215.

Schiebinger, L. (1993). Why mammals are called mammals: gender politics in eighteenth-century natural history. *The American Historical Review, 98*(2), 382-411.

Schießl, I., Stetter, M., Mayhew, J. E., McLoughlin, N., Lund, J. S., & Obermayer, K. (2000). Blind signal separation from optical imaging recordings with extended spatial decorrelation. *IEEE Transactions on Biomedical Engineering, 47*(5), 573-577.

Schmolesky. (2007, June, 14). The primary visual cortex. *Webvision.* https://webvision.med.utah.edu/book/part-ix-brain-visual-areas/the-primary-visual-cortex/

Scholl, B., Tan, A. Y., Corey, J., & Priebe, N. J. (2013). Emergence of orientation selectivity in the mammalian visual pathway. *Journal of Neuroscience, 33*(26), 10616-10624.

Schoppmann, A., & Stryker, M. P. (1981). Physiological evidence that the 2-deoxyglucose method reveals orientation columns in cat visual cortex. *Nature, 293*(5833), 574-576.

Schottdorf, M., Eglen, S. J., Wolf, F., & Keil, W. (2014). Can retinal ganglion cell dipoles seed iso-orientation domains in the visual cortex? *PloS one, 9*(1), e86139.

Schwartz, O., Pillow, J. W., Rust, N. C., & Simoncelli, E. P. (2006). Spike-triggered neural characterization. *Journal of vision, 6*(4), 13-13.

Sebel, P., Flynn, P., & Ingram, D. (1984). Effect of nitrous oxide on visual, auditory and somatosensory evoked potentials. *British Journal of Anaesthesia, 56*(12), 1403-1407.

Sengpiel, F., Stawinski, P., & Bonhoeffer, T. (1999). Influence of experience on orientation maps in cat visual cortex. *Nature neuroscience, 2*(8), 727-732.

Sharpee, T. O. (2013). Computational identification of receptive fields. *Annual review of neuroscience, 36*, 103-120.

Shaw, G., Renfree, M., & Short, R. (1988). Experimental manipulation of sexual differentiation in wallaby pouch young treated with exogenous steroids. *Development, 104*(4), 689-701.

Sheng, X. M., Marotte, L., & Mark, R. (1990). Development of connections to and from the visual cortex in the wallaby (Macropus eugenii). *Journal of Comparative Neurology, 300*(2), 196-210.

Shmuel, A., & Grinvald, A. (2000). Coexistence of linear zones and pinwheels within orientation maps in cat visual cortex. *Proceedings of the National Academy of Sciences, 97*(10), 5568-5573.

Shouval, H. Z., Goldberg, D. H., Jones, J. P., Beckerman, M., & Cooper, L. N. (2000). Structured long-range connections can provide a scaffold for orientation maps. *Journal of Neuroscience, 20*(3), 1119-1128.

Simoncelli, E. P., & Llampaninski, J. P. (2004). Responses with stochastic stimuli. *The cognitive neurosciences*, 327.

Sirotin, Y. B., & Das, A. (2009). Anticipatory haemodynamic signals in sensory cortex not predicted by local neuronal activity. *Nature, 457*(7228), 475-479.

Sirotin, Y. B., Hillman, E. M., Bordier, C., & Das, A. (2009). Spatiotemporal precision and hemodynamic mechanism of optical point spreads in alert primates. *Proceedings of the National Academy of Sciences, 106*(43), 18390-18395.

Skottun, B. C., De Valois, R. L., Grosof, D. H., Movshon, J. A., Albrecht, D. G., & Bonds, A. (1991). Classifying simple and complex cells on the basis of response modulation. *Vision research, 31*(7-8), 1078-1086.

Smith, E. L., Chino, Y. M., Ridder, W. H., Kitagawa, K., & Langston, A. (1990). Orientation bias of neurons in the lateral geniculate nucleus of macaque monkeys. *Visual neuroscience, 5*(6), 525-545.

So, Y. T., & Shapley, R. (1979). Spatial properties of X and Y cells in the lateral geniculate nucleus of the cat and conduction velocities of their inputs. *Experimental Brain Research, 36*(3), 533-550.

Spitzer, H., & Hochstein, S. (1985). A complex-cell receptive-field model. *Journal of neurophysiology, 53*(5), 1266-1286.

Springer, M. S., Murphy, W. J., Eizirik, E., & O'Brien, S. J. (2003). Placental mammal diversification and the Cretaceous–Tertiary boundary. *Proceedings of the National Academy of Sciences, 100*(3), 1056-1061.

Stevens, C. F. (2001). An evolutionary scaling law for the primate visual system and its basis in cortical function. *Nature, 411*(6834), 193-195.

Stewart, D. L., Chow, K. L., & Masland, R. H. (1971). Receptive-field characteristics of lateral geniculate neurons in the rabbit. *Journal of neurophysiology, 34*(1), 139-147.

Sun, W., Tan, Z., Mensh, B. D., & Ji, N. (2016). Thalamus provides layer 4 of primary visual cortex with orientation-and direction-tuned inputs. *Nature neuroscience, 19*(2), 308.

Sun, S. H., Almasi, A., Yunzab, M., Zehra, S., Hicks, D. G., Kameneva, T., Ibbotson, M. R., & Meffin, H. (2021). Analysis of extracellular spike waveforms and associated receptive fields of neurons in cat primary visual cortex. *The Journal of Physiology*.

Swindale, N. V. (2004). How different feature spaces may be represented in cortical maps. *Network: computation in neural systems, 15*(4), 217-242.

Talebi, V., & Baker Jr, C. L. (2016). Categorically distinct types of receptive fields in early visual cortex. *Journal of neurophysiology, 115*(5), 2556-2576.

Tanaka, S., Ribot, J., Imamura, K., & Tani, T. (2006). Orientation-restricted continuous visual exposure induces marked reorganization of orientation maps in early life. *Neuroimage, 30*(2), 462-477.

Tibben, E. A., Holland, R. A., & Tyndale-Biscoe, C. (1991). Blood oxygen carriage in the marsupial, tammar wallaby (Macropus eugenii), at prenatal and neonatal stages. *Respiration physiology, 84*(1), 93-104.

Touryan, J., Felsen, G., & Dan, Y. (2005). Spatial structure of complex cell receptive fields measured with natural images. *Neuron, 45*(5), 781-791.

Touryan, J., Lau, B., & Dan, Y. (2002). Isolation of relevant visual features from random stimuli for cortical complex cells. *Journal of Neuroscience, 22*(24), 10811-10818.

Ts'o, D. Y., Frostig, R. D., Lieke, E. E., & Grinvald, A. (1990). Functional organization of primate visual cortex revealed by high resolution optical imaging. *Science, 249*(4967), 417-420.

Tyler, C., Dunlop, S., Lund, R., Harman, A., Dann, J., Beazley, L., & Lund, J. (1998). Anatomical comparison of the macaque and marsupial visual cortex: common features that may reflect retention of essential cortical elements. *Journal of Comparative Neurology, 400*(4), 449-468.

Usrey, W. M., Alonso, J.-M., & Reid, R. C. (2000). Synaptic interactions between thalamic inputs to simple cells in cat visual cortex. *Journal of Neuroscience, 20*(14), 5461-5467.

Van Hooser, S. D. (2007). Similarity and diversity in visual cortex: is there a unifying theory of cortical computation? *The neuroscientist, 13*(6), 639-656.

Van Hooser, S. D., Heimel, J. A. F., Chung, S., Nelson, S. B., & Toth, L. J. (2005). Orientation selectivity without orientation maps in visual cortex of a highly visual mammal. *Journal of Neuroscience, 25*(1), 19-28.

Van Hooser, S. D., & Nelson, S. B. (2006). The squirrel as a rodent model of the human visual system. *Visual neuroscience, 23*(5), 765.

Venkataramani, S., & Taylor, W. R. (2010). Orientation selectivity in rabbit retinal ganglion cells is mediated by presynaptic inhibition. *Journal of Neuroscience, 30*(46), 15664-15676.

Vidyasagar, T., Wye-Dvorak, J., Henry, G., & Mark, R. (1992). Cytoarchitecture and visual field representation in area 17 of the tammar wallaby (Macropus eugenii). *Journal of Comparative Neurology, 325*(2), 291-300.

Vidyasagar, T. R., & Eysel, U. T. (2015). Origins of feature selectivities and maps in the mammalian primary visual cortex. *Trends in neurosciences, 38*(8), 475-485.

Waite, P., Marotte, L., & Leamey, C. (1994). Timecourse of development of the wallaby trigeminal pathway. I. Periphery to brainstem. *Journal of Comparative Neurology, 350*(1), 75-95.

Wang, Y., Jin, J., Kremkow, J., Lashgari, R., Komban, S. J., & Alonso, J. M. (2015). Columnar organization of spatial phase in visual cortex. *Nature neuroscience, 18*(1), 97-103.

Weigand, M., Sartori, F., & Cuntz, H. (2017). Universal transition from unstructured to structured neural maps. *Proceedings of the National Academy of Sciences, 114*(20), E4057-E4064.

Weisbecker, V., & Goswami, A. (2010). Brain size, life history, and metabolism at the marsupial/placental dichotomy. *Proceedings of the National Academy of Sciences, 107*(37), 16216-16221.

Weliky, M., Bosking, W. H., & Fitzpatrick, D. (1996). A systematic map of direction preference in primary visual cortex. *Nature, 379*(6567), 725-728.

Wilson, D. E., Whitney, D. E., Scholl, B., & Fitzpatrick, D. (2016). Orientation selectivity and the functional clustering of synaptic inputs in primary visual cortex. *Nature neuroscience, 19*(8), 1003-1009.

Wimborne, B., Mark, R., & Ibbotson, M. (1999). Distribution of retinogeniculate cells in the tammar wallaby in relation to decussation at the optic chiasm. *Journal of Comparative Neurology, 405*(1), 128-140.

Wong, R. C., Cloherty, S. L., Ibbotson, M. R., & O'Brien, B. J. (2012). Intrinsic physiological properties of rat retinal ganglion cells with a comparative analysis. *Journal of neurophysiology, 108*(7), 2008-2023.

Wye-Dvorak, J., Levick, W., & Mark, R. (1987). Retinotopic organization in the dorsal lateral geniculate nucleus of the tammar wallaby (Macropus eugenii). *Journal of Comparative Neurology, 263*(2), 198-213.

Wynne, C., & McLean, I. G. (1999). The comparative psychology of marsupials. *Australian Journal of Psychology, 51*(2), 111-116.

Xu, X., Bosking, W., Sáry, G., Stefansic, J., Shima, D., & Casagrande, V. (2004). Functional organization of visual cortex in the owl monkey. *Journal of Neuroscience, 24*(28), 6237-6247.

Xu, X., Ichida, J., Shostak, Y., Bonds, A., & Casagrande, V. A. (2002). Are primate lateral geniculate nucleus (LGN) cells really sensitive to orientation or direction? *Visual neuroscience, 19*(1), 97.

Yang, H., Rutte, R., Jones, L., Simson, M., Sagawa, R., Ryll, H., Huth, M., Pennycook, T., Green, M., & Soltau, H. (2016). Simultaneous atomic-resolution electron ptychography and Z-contrast imaging of light and heavy elements in complex nanostructures. *Nature Communications, 7*(1), 1-8.

Yunzab, M., Cloherty, S. L., & Ibbotson, M. R. (2019). Comparison of contrast-dependent phase sensitivity in primary visual cortex of mouse, cat and macaque. *Neuroreport, 30*(14), 960.

Zeki, S., Watson, J., Lueck, C., Friston, K. J., Kennard, C., & Frackowiak, R. (1991). A direct demonstration of functional specialization in human visual cortex. *Journal of Neuroscience, 11*(3), 641-649.

Zeki, S. M. (1974). Functional organization of a visual area in the posterior bank of the superior temporal sulcus of the rhesus monkey. *The Journal of physiology, 236*(3), 549-573.